Assimilation of New-generation Geostationary Meteorological Satellite Data in Mesoscale Numerical Weather Prediction

Michiko OTSUKA

Department of Geography

Graduate School of Urban Environmental Sciences

Tokyo Metropolitan University

September 2021

Contents

List of Figures

Figure 3.5. JMA produced weather analysis at (a) 0000 UTC, (c) 1200 UTC on 20, and (e) 0000 UTC on 21 June 2016 for the surface. Geopotential heights in meters (color shades) and contours of temperatures in degrees Celsius using a contour interval of 3.0 degrees at 500 hPa height obtained from JMA's meso analyses at (b) 0000 UTC, (d) 1200 UTC on 20, and (f) 0000 UTC on 21 June 2016.

Figure 3.6. The spatial distribution of assimilated RS-AMVs during the period 0600–0900 UTC on 20 June 2016 around Japan. Purple, blue, and green arrows represent high-, mid-, and low-level winds, respectively. (a) CNTL with RTN-AMVs, (b) ALL with RS-AMVs, (c) CNTL0.5 with RTN-AMVs thinned to 0.5 deg., (d) ALL1.0 with RS-AMVs thinned to 1.0 deg., and ALL minus first guess for (e) low-level winds and (f) mid- and high-level winds.

Figure 3.7. Differences in the analysis results between ALL and CNTL (ALL minus CNTL) at 0900 UTC on 20 June 2016 after the four assimilation cycles. (a) Wind vectors and wind speeds at 500 hPa, (b) wind vectors and wind speeds at 300 hPa, (c) geopotential heights at 500 hPa, and (d) temperatures at 500 hPa. Arrows represent wind direction in (a) and (b). Color shades represent wind speed (m s^{-1}) in (a) and (b), geopotential heights in (c), and temperatures in (d). A cross in each figure indicates the position of the center of the cold vortex.

Figure 3.8. Forecast results in ALL and CNTL. (a) Geopotential heights (color shades) and temperatures (contour lines) at 500 hPa in ALL, differences between ALL and CNTL (ALL minus CNTL) in (b) geopotential heights and (c) temperatures at 500 hPa, and (d) surface pressure (hPa) at 1200 UTC on 20 June 2016 (FT03). (e) Geopotential heights (color shades) and temperatures (contour lines) at 500 hPa in ALL and (f) differences between ALL and CNTL in geopotential heights at 500 hPa at 0000 UTC on 21 June 2016 (FT15). Color shades represent differences of geopotential heights in (b) and (f), temperatures in (c), and surface pressures in (d).

Figure 3.9. Forecast winds and temperatures in northern Japan validated against sonde observations. The two upper panels (a, b) at FT03, the bottom panels (c, d) at FT15. RMSVD profiles (a, c) and RMSE profiles for temperature (b, d). The black solid line represents ALL, and the dashed line represents CNTL. The gray line indicates ALL1.0 with 1.0° data thinning, while the gray dashed line indicates CNTL0.5 with 0.5° thinning scale.

Figure 3.10. Differences in the analysis and forecast results of geopotential heights at 500 hPa from CNTL. Analysis differences in (a) ALL and (b) B03, (c) B07, (d) B08, (e) B09, (f) B10, (g) B13, and (h) B16. Forecast differences at 1200 UTC 20 June 2016 (FT03) in (i) ALL and (j) B03, (k) B07, (l) B08, (m) B09, (n) B10, (o) B13, and (p) B16. Forecast differences at 0000 UTC 21 June 2016 (FT15) in (q) ALL and (r) B03, (s) B07, (t) B08, (u) B09, (v) B10, (w) B13, and (x) B16.

Figure 3.11. Forecast winds in northern Japan validated against sonde observations. Profiles of RMSVD differences from CNTL for the (a) VIS, (b) IR, (c) WV, and (d) CO2 channels at FT03 and (e) VIS, (f) IR, (g) WV, and (h) CO_2 channels at FT15. The dotted lines indicate ALL. The solid line represents B03 in (a) and (e), B07 in (b) and (f), B08 in (c) and (g), and B16 in (d) and (h). The dashed line represents B13 in (b) and (f), and B09 in (c) and (g). The dash-dot line represents B10 in (c) and (g).

Figure 3.12. Forecast winds in northern Japan validated against WPR observations. (a) RMSVDs at each forecast hour and (b) profiles of RMSVD averaged over the whole forecast period. The solid lines and dashed lines represent ALL and CNTL, respectively.

Figure 3.13. Forecast winds in northern Japan validated against WPR observations. Profiles of RMSVD differences from CNTL averaged over the entire forecast period for the (a) VIS, (b) IR, (c) WV, and (d) CO_2 channels. The dotted lines indicate ALL. The solid line represents B03 in (a), B07 in (b), B08 in (c), and B16 in (d). The dashed line represents B13 in (b) and B09 in (c). The dash-dot line represents B10 in (c).

Figure 4.1. Appearance frequencies of cloud properties: (a) COT, (b) CTP (hPa), (c) CRE (μm), (d) CWP (g m^{-2}) according to present weather categories in July 2017. White, light gray, and black bars represent fair, cloudy, and rainy weather conditions.

Figure 4.2. Examples of relative humidity over water (solid blue lines) and ice (dashed blue lines) and temperature (solid turquoise blue lines) profiles, and cloud layers (light blue rectangles) obtained by sonde observations together with OCA CTPs (red squares) within a radius of 5 km from a sonde station (Fukuoka). (a) 1 July, (b) 2 July, (c) 9 July, and (d) 10 July 2017. CF values in tenth were (a) 10^{-1} (overcast with openings), (b) 7, (c) 10^{-1}, and (d) 10^{-1}. There was rain in (c).

Figure 4.3. Frequencies of differences of (a) CTP (hPa) and (b) CTH (m) between OCA and sonde observation (OCA minus sonde) in July 2017. The white, light gray, and dark gray bars are histogram when OCA CTP levels were higher than 440 hPa, equal to 440−680 hPa, and lower than 680 hPa.

Figure 4.4. Frequencies of differences between OCA and NHM (OCA minus NHM) during the period 0000−0900 UTC 7−10 September 2015: (a) CWP (LWP and IWP are shown by dark and light gray bars, respectively) (g m^{-2}), (b) all OCA CTP levels (hPa), and (c) OCA CTP values at three heights. The white, light gray, and dark gray bars show frequencies when OCA CTP levels were above 440 hPa, equal to 440−680 hPa, and below 680 hPa. In (a), the left and the right sides of the histograms are cutoff. The minimum and maximum differences (g m^{-2}) for LWP and IWP are -68,719 and 1,997, -72,983 and 4,815, respectively.

Figure 4.5. Himawari-8 OCA data: (a) CTP (hPa), (b) COT, and (c) CWP (g m^{-2}), and (d) CWP differences between OCA and NHM (OCA minus NHM) at 0200 UTC 8 September 2015. In (c), the gray pattern in the vicinity of the typhoon represents COT values above 100 and corresponds to the gray pattern in the same area in (d).

Figure 4.6. (a) The JNoVA domain and (b) locations of the Kanto and Kyushu areas (circles with dashed lines), where the heavy rainfalls examined in the experiments of this study occurred, and surrounding areas. Topography (meters above sea level) is indicated by shading.

Figure 4.7. Synoptic situation for the assimilation experiment on 9 September 2015. (a) Surface weather map and (b) Himawari-8 IR and VIS composite image at 0000 UTC produced by JMA. In (b), yellow color represents low clouds, white represents thick and high clouds such as Cb and Ns, and blue represents cirrus clouds.

Figure 4.8. Frequency histograms of departures of assimilated OCA pseudo-RH from (a) first-guess and (b) analysis results during the 0000−0900 UTC 9 September 2015 assimilation period. (c) Distribution map of pseudo-RH data points at 0900 UTC. In (c), the circles indicate points where pseudo-RH profiles for assimilation were obtained. The color of each circle indicates the pseudo-RH value at the top of the profile.

Figure 4.9. Differences in analysis results between TEST and CNTL at 0900 UTC 9 September 2015. Water vapor mixing ratio (kg kg^{-1}) at (a) 850 hPa, (b) 700 hPa, and (c) 500 hPa, (d) sea surface pressure and wind speed at (e) the surface and (f) 850 hPa. Color shading in (e) and (f) indicates differences of wind speed (m s^{-1}) between TEST and CNTL, and arrows indicate wind vectors in TEST.

Figure 4.10. Differences of forecast RH and wind speed at 850 hPa between TEST and CNTL. (a), (b) and (c) for RH (%), (d), (e) and (f) for v-component wind (m s^{-1}), and (g), (h) and (i) for wind speed (m s^{-1}). (a), (d) and (g) at the 9 h, (b), (e), and (h) at 12 h, and (c), (f), and (i) at 15 h forecast time. Color shading indicates differences of RH in (a)−(c) and wind speed in (d)−(i) between TEST and CNTL, and arrows in (g)−(i) indicate wind vectors in TEST.

Figure 4.11. 3-h precipitation (mm) in observations and forecasts on 9 September 2015. (a), (b), and (c) Radar/rain gauge-analyzed precipitation (RAP); (d), (e), and (f) forecasts by TEST; (g), (h), and (i) forecasts by CNTL. (a), (d), and (g) FT = 09 (1800 UTC 9 September 2015); (b), (e), and (f) FT = 12 (2100 UTC 9 September 2015); (c), (f), and (i) FT = 15 (0000 UTC 10 September 2015).

Figure 4.12. Precipitation forecast (a) threat and (b) bias scores for the 3-h precipitation thresholds at every 3 h of forecast time in CNTL (green lines) and TEST (red lines). Thin, thick, and dashed lines indicate threshold values of 1 mm, 10 mm, and 20 mm, respectively. Threat score = hits / (hits + misses + false alarms). Bias score = (hits + false alarms) / (hits +misses).

Figure 4.13. Forecast RH, temperature, and wind validated against sonde observations. (a, b, c, d) FT = 03 (1200 UTC 9 September 2015); (e, f, g, h) FT = 15 (0000 UTC 10 September 2015); (i, j, k, l) FT = 27 (1200 UTC 10 September 2015). (a, e, i) RH (%); (b, f, j) temperature (K); (c, g, k); u-component wind (m s^{-1}); and (d, h, i) v-component wind (m s^{-1}) in CNTL (solid green lines) and TEST (solid red lines). The green dashed lines represent RMSEs in CNTL, and the red dashed lines represent RMSEs in TEST.

Figure 4.14. Synoptic situation and differences in water vapor analyses for the assimilation experiments on 4 and 5 July 2017. (a, d) Surface weather maps, (b, e) Himawari-8 IR and VIS composite images with the same color patterns as in Fig.4.7b, and (c, f) differences in analysis results for RH (%) between TEST and CNTL at 700 hPa at (a, b, c) 0000 UTC 4 July and (d, e, f) 0000 UTC 5 July.

Figure 4.15. Precipitation forecast (a, c) threat and (b, d) bias scores for the 3-h precipitation thresholds at every 3 h of forecast time in the assimilation experiments on (a, b) 4 July and (c, d) 5 July 2017. Green lines represent CNTL, and red lines represent TEST. The thin, thick, and dashed lines indicate threshold values of 1 mm, 10 mm, and 20 mm, respectively.

Figure 4.16. 3-h precipitation (mm) in observations and forecasts on 5 July 2017. (a, b, c, d) Radar/rain gauge-analyzed precipitation (RAP); (e, f, g, h) forecasts by TEST; (i, j, k, l) forecasts by CNTL. (a, e, f) at FT03 (1200 UTC); (b, f, j) at FT06 (1500 UTC); (c, g, k) at FT09 (1800 UTC); (d, h, l) at FT12 (2100 UTC)

List of Tables

Acronyms

AHI Advanced Himawari Imager

AMV atmospheric motion vector

CALIPSO Cloud-Aerosol Lidar and Infrared Pathfinder Satellite Observations

CBH cloud base height

CF cloud fraction

CGMS Coordination Group for Meteorological Satellites

CGT cloud geometric thickness

CMA China Meteorological Agency

COT cloud optical thickness

CPR cloud profiling radar

CRE cloud effective radius

CSR clear sky radiance

CTH cloud top height

CTP cloud top pressure

CWC cloud water content

CWP cloud water path

DA data assimilation

ECMWF European Centre for Medium-Range Weather Forecasts

EUMETSAT European Organisation for the Exploitation of Meteorological Satellites

4D-Var four-dimensional variational DA

FT forecast time

GEO geostationary earth orbit satellite

GOES Geostationary Operational Environmental Satellite

GSM Global Spectral Model of JMA

IR infrared (channel)

ISCCP International Satellite Cloud Climatology Project

IWP ice water path

JMA Japan Meteorological Agency

JNoVA JMA's NHM with 4-dimensional variational data assimilation

LEO low earth orbit satellite

LWC liquid water content

LWP liquid water path

MA JMA's Mesoscale Analysis

MD mean difference

ME mean error

MODIS Moderate Resolution Imaging Spectroradiometer

MSC Meteorological Satellite Center of JMA

MSM Meso-scale Model of JMA

MTSAT Multi-functional Transport Satellite (or Himawari-6 and -7)

NASA National Aeronautics and Space Administration

NHM Non-Hydrostatic Model of JMA

NOAA National Oceanic and Atmospheric Administration

NWP numerical weather prediction

OCA optimal cloud analysis

QC quality control

QI quality indicator flag (for AMV data)

RH relative humidity

RMSD root mean square difference

RMSE root mean square error

RMSVD root mean square vector difference

RS rapid scan

RS-AMV AMV obtained from rapid scan imagery

RTM radiative transfer model

RTN-AMV routinely obtained AMV with a low temporal resolution such as an hour

RTTOV Radiative Transfer for TOVS

TIROS Television Infrared Observation Satellites

TOVS TIROS Operational Vertical Sounder

VIS visible (channel)

WMO World Meteorological Organization

WPR wind profiler

WV water vapor (channel)

Acknowledgement

First of all, I would like to express my deepest gratitude to Professor Jun Matsumoto for guiding me through the doctoral thesis. He was also my supervisor when I got a master's degree at the Tokyo Metropolitan University (TMU) in 2009. I respect him for his passion and insights in his expertise, particularly the efforts to utilize observational data as much as possible that have been neglected and forgotten for years in climate research. I always feel that the values of observations should be more appreciated both in the operational and research community because the enormous efforts of so many known and unknown people were involved in making them available for use. I think I was fortunate to get a chance to learn under Professor Matsumoto who fully understands the importance of observations.

I am grateful to Professor Hideo Takahashi and Professor Hiroshi Matsuyama for their valuable comments while carefully reviewing the thesis. Their suggestions have greatly helped me improve the manuscript.

I'd like to thank all the staff and students in the climate laboratory of TMU for accepting me as a member of the team. Even when I first joined the master's course, I was ten years elderly compared to other students, and now, I belong to their parent's generation. I appreciate the patience and kindness of every one of TMU.

I owe much of my research achievements to the wonderful collaborators at the Japan Meteorological Agency (JMA). Dr. Hiromu Seko, who was my supervisor at the Meteorological Research Institute of JMA in 2014–2019, has guided me throughout the research in mesoscale meteorology and data assimilation. Mr. Masaru Kunii, Mr. Kazuki Shimoji, Mr. Masahiro Hayashi, Mr. Koji Yamashita, and Mr. Ko Koizumi are excellent experts in their field and always helpful to me.

Finally, I thank my family, my husband, and two sons for their continuous supports.

Chapter 1 General introduction

1.1. Mesoscale numerical weather prediction and satellite data

Weather forecasts issued by national meteorological services worldwide are based on numerical weather prediction (NWP), whose history of over half a century has been summarized in several books and papers (e.g., Kalnay 2003; Harper et al. 2007; Yoden 2007). NWP is essentially a time integration of computer models of the atmosphere starting from appropriate initial states, that is, an initial value problem on a supercomputer (Kalnay 2003). In order to obtain skillful forecasts, the initial conditions should be accurately known, and the model should realistically represent the atmosphere. Data assimilation (DA) plays a crucial role in NWP to provide the initial states of the atmosphere by statistically constraining model variables with observations.

Mesoscale NWP systems produce short-range forecasts (typically 1–2 days) over a limited area with a fine resolution of one to several kilometers. It aims to forecast various mesoscale events, including torrential rainfalls and other types of severe weather that can seriously affect our daily social and economic activities. The challenges posed for mesoscale NWP systems include quickly evolving processes that require a rapid update of the assimilation cycles, complex, non-linear, and flow-dependent relationships between model variables and observations that come from dealing with convective disturbances (Fabry and Sun 2008), and the influence of lateral boundary conditions usually obtained by global models with larger domains (Vukicevic and Paegle 1989). Besides these general issues, one solution to realize practical improvements for more accurate mesoscale forecasts in the current NWP systems is to better exploit the information obtained from observations and better estimate the forecasts' initial states. The increased availability of new data obtained by various remote sensing instruments, including those onboard satellites, enables

exploring the potential impacts of such data in mesoscale forecasts. The nature and characteristics of these new data, which need to be accounted for in mesoscale DA systems, are not fully understood.

Satellite observations in the visible, infrared, and microwave spectrum currently occupy a significant part of the impacts of all the observations routinely assimilated for global NWP (Geer et al. 2018), thanks to the development of DA techniques, including the direct assimilation of radiances. They provide useful information on the initialization of temperature, water vapor, and wind fields, including over the oceans where in-situ observations are scarce. However, assimilating satellite data into mesoscale NWP systems has yet to be fully explored. Because mesoscale NWP needs to be run closer to real-time to predict rapidly developing weather on a small scale, it may have relied more on surface-based local observations such as radars with high spatial and temporal resolution rather than satellites. Geostationary earth orbit satellites (hereafter GEOs) are usually boarded with visible and infrared imagers and constitute an essential part of the World Weather Watch's Global Observing System (WMO 2019) together with near-polar orbiting and other lower earth orbit satellites (LEOs). A primary disadvantage of GEOs before the Japan Meteorological Agency (JMA) 's Himawari-8 (Bessho et al. 2016) was their lower resolution of observations with 2–4 km spatial and 30-min temporal resolution compared to ground-based radars and other high-resolution remote-sensing observations.

1.2. DA and variational methods

DA may have started as 'objective analysis' to provide initial conditions in NWP, but soon became a research topic of mathematical methodology and has been recognized as an important science in itself (Kalnay 2003) since around the 1980s when variational methods and Kalman filters appeared and were developed in

meteorology. In the late 1990s, each major NWP centre, including JMA, began a re-analysis project to provide long-term 3-dimensional atmospheric data constructed through forecast and analysis cycles of DA. These analyses are homogeneously available in time and space for several decades, and they have already proved to be valid and became essential in a variety of meteorological and climatological studies (Kalnay et al. 1996; Berrisford et al. 2011; Kobayashi et al. 2015; Harada et al. 2016). Furthermore, DA can provide detailed analyses of the atmosphere and a research method to integrate the observational approach and simulation approach for understanding meteorological phenomena (Tsuyuki 2008). Because simulations by numerical models are based on physics, DA has the potential to give the best estimate of the atmosphere by combining the law of physics and real observations. How to bridge the gap between the theory and the real world may involve many technical issues; however, the basic principle is based on mathematical theories.

There are several well-known textbooks about DA (e.g., Reich and Cotter 2015). We here overview the theory of variational methods used in this study briefly based on Kalnay (2003) and Tsuyuki (2008). Among different kinds of methods for DA, variational methods may be most widely used in today's NWP centres around the world.

In variational methods, the best estimate (analysis, $\mathbf{x_a}$) is defined as the most likely value of the state variables ($\mathbf{x}$) given the background forecast ($\mathbf{x_b}$), the observation ($\mathbf{y_o}$), and their statistical errors as the form of the error covariance matrix ($\mathbf{B}$ and $\mathbf{R}$, respectively). The Bayes formula for a conditional probability distribution of $\mathbf{x}$ is

$$p\,(\mathbf{x} \mid \mathbf{x_b}, \mathbf{y_o}) = \frac{p(\mathbf{x_b},\ \mathbf{y_o} \mid \mathbf{x})p(\mathbf{x})}{p(\mathbf{x_b},\ \mathbf{y_o})} \quad . \tag{1.1}$$

When $\mathbf{x_b}$ and $\mathbf{y_o}$ happen independently for the atmospheric state $\mathbf{x}$, Eq. (1. 1) can be rewritten as

$$p\,(\mathbf{x}\mid \mathbf{x_b}, \mathbf{y_o}) = \frac{p(\mathbf{x_b}\mid \mathbf{x})p(\mathbf{y_o}\mid \mathbf{x})p(\mathbf{x})}{p(\mathbf{x_b},\ \mathbf{y_o})}\ . \tag{1.2}$$

The analysis $\mathbf{x_a}$ is obtained by maximizing *a posteriori* estimate of Eq. (1. 2) as

$$\mathbf{x_a}\ = arg\ \max_x[p(\mathbf{x_b}\mid \mathbf{x})p(\mathbf{y_o}\mid \mathbf{x})p(\mathbf{x})]\ . \tag{1.3}$$

$p(\mathbf{x})$ can be considered to be climatological and uniform distribution, so excluded from Eq. (1. 3). Then,

$$\mathbf{x_a}\ = arg\ \max_x[p(\mathbf{x_b}\mid \mathbf{x})p(\mathbf{y_o}\mid \mathbf{x})]\ . \tag{1.4}$$

Instead of solving Eq. (1. 4), $\mathbf{x_a}$ is determined when it minimizes a cost function,

$$J(\mathbf{x}) = -\,log[p(\mathbf{x_b}\mid \mathbf{x})] - log[p(\mathbf{y_o}\mid \mathbf{x})]\ , \tag{1.5}$$

$$\mathbf{x_a} = \ arg\ \min_x J(\mathbf{x})\,.$$

We assume to have $\mathbf{x_b}$ of n-variables without any bias; thus, its probability can be given by the Gaussian distribution,

$$p(\mathbf{x_b}\mid \mathbf{x}) = \frac{1}{(\sqrt{2\pi})^n\sqrt{|\mathbf{B}|}} \times exp\left[-\frac{1}{2}(\mathbf{x_b}-\mathbf{x})^T\mathbf{B}^{-1}(\mathbf{x_b}-\mathbf{x})^T\right]. \tag{1.6}$$

$|\cdot|$ denotes a determinant. $\mathbf{B}$ is a $n \times n$ positive definite matrix and called as background error covariance matrix, defined by,

$$\mathbf{B} = \ \langle(\mathbf{x_b}-\mathbf{x_t})(\mathbf{x_b}-\mathbf{x_t})^T\rangle\,. \tag{1.7}$$

$\mathbf{x_t}$ is the true state of $\mathbf{x}$. In the same way, $p\ (\mathbf{y_o}|\ \mathbf{x})$ is given by,

$$p(\mathbf{y_o}\mid \mathbf{x}) = \frac{1}{(\sqrt{2\pi})^{\,m}\sqrt{|\mathbf{R}|}} \times exp\left[-\frac{1}{2}\big(\mathbf{y_o}-H(\mathbf{x})\big)^T\mathbf{R}^{-1}\big(\mathbf{y_o}-H(\mathbf{x})\big)^T\right], \tag{1.8}$$

where m is the number of observations and H is the observation operator. $\mathbf{R}$ is a $m \times m$ positive definite matrix and the observation error covariance matrix defined by

$$\mathbf{R} = \ \langle\big(\mathbf{y_o}-H(\mathbf{x_t})\big)\big(\mathbf{y_o}-H(\mathbf{x_t})\big)^{\boldsymbol{T}}\rangle\,. \tag{1.9}$$

Eqs. (1. 6) and (1. 8) into Eq. (1. 5), we obtain the cost function of the variational method as

$$J(\mathbf{x}) = \frac{1}{2}(\mathbf{x}-\mathbf{x}_\mathrm{b})^T\mathbf{B}^{-1}(\mathbf{x}-\mathbf{x}_\mathrm{b}) + \frac{1}{2}(H(\mathbf{x})-\mathbf{y}_\mathrm{o})^T\mathbf{R}^{-1}(H(\mathbf{x})-\mathbf{y}_\mathrm{o}). \tag{1.10}$$

Since $\mathbf{x_a}$ gives the minimum value of Eq. (1. 10), we obtained $\mathbf{x_a}$ by solving

$$\nabla J(\mathbf{x_a}) = \mathbf{B}^{-1}(\mathbf{x} - \mathbf{x}_\mathrm{b})^T + \mathbf{R}^{-1}\,(H(\mathbf{x}) - \mathbf{y}_\mathrm{o})^T = 0. \qquad (1.11)$$

Because we deal with the new observations in this study, we especially have interests in constructing an appropriate **R**, representing all the necessary information regarding the uncertainties of assimilated observations, to properly account for the error characteristics and representativeness of the observations in DA systems.

Observation errors and their correlations are diagnostically estimated based on differences between observations and first-guess or analysis equivalents obtained from assimilation cycles (Hollingsworth and Lönnberg 1986; Desroziers et al. 2005). Bormann and Bauer (2010) summarized the estimation methods in detail, including their assumptions and limitations.

1.3. Mesoscale DA systems of JMA

National NWP centres, including JMA, usually run mesoscale systems beside global systems for limited local domains aiming at short-range prediction of up to 1 to 2 days with horizontal resolutions around 1 km (so-called 'convective-scale') to several kilometers. Gustafsson et al. (2018) review mesoscale and convective-scale DA systems operated by major NWP centres in detail. The choice of DA methods depends on the computational cost for running in real-time with frequent updates in high-resolution, the scale of targeted phenomena, and the availability of observations according to different local needs and interests. Most centres operationally assimilate GEO data such as atmospheric motion vector (AMV), clear sky radiance (CSR), and cloud products.

JMA has employed a four-dimensional variational (4D-var) system to provide initial conditions for the Meso-scale Model (MSM) since 2002 and became the first NWP centre to adapt 4D-Var to an operational limited-area system (JMA 2013). The MSM was upgraded to the JMA's Non-Hydrostatic Model, JMA NHM (Saito et al.

2006) in 2004, and the JMA NHM based variational analysis data assimilation (JNoVA; Honda et al. 2005) was introduced in 2009. It had been an operational mesoscale DA system of JMA until March 2020, and we used it in this study. It is a 4D-Var system adopting an incremental approach (Coutier et al. 1994) with a spatial resolution of 5 km and 15 km for the outer and inner models, respectively, of 48 vertical levels, and is updated every three hours. Firstly, an analysis increment is determined at the low-resolution (15 km) inner model to minimize the cost function. Then, the analysis increment is interpolated to the high-resolution (5 km) analysis increment and added to the background forecast field in the outer model to produce a high-resolution analysis. JMA (2013, 2019) describes the details of JNoVA. A wide variety of observations, including surface, upper-air, radar, satellite data, are assimilated hourly within a 3-hour window.

1.4. New-generation geostationary satellite data

Himawari-8 was launched in 2014 and became the first so-called next-generation GEO (CGMS 2018) in operation in 2015, followed by the China Meteorological Agency (CMA) Fengyun-4 (Yang et al. 2017), the National Oceanic and Atmospheric Administration (NOAA) / the National Aeronautics and Space Administration (NASA) Geostationary Operational Environmental Satellite (GOES)-16 and 17 (Rehbein et al. 2020), Geostationary-Korea Multi-Purpose Satellite-2 (GEO-KOMPSAT-2A), and Himawari-9. We hereafter call them new-generation GEOs instead of next-generation ones now that they are operationally run. Himawari-8 is equipped with the Advanced Himawari Imager (AHI) and has 16 observation channels with an enhanced resolution of 0.5 to 1 km for the visible and 2 km for the infrared channels. The temporal resolution has also significantly increased to 10 min for full disk scans. It has already benefited the JMA's operational global and mesoscale NWP with increased quality and quantity of data for

assimilation (e.g., Yamashita 2016; Kazumori 2018). Moreover, Himawari-8 conducted round-the-clock 2.5-min sector scans around Japan and 30-s to 2.5-min rapid scans for continuous monitoring, including tracking typhoons. Several studies have shown the benefits of using such high-frequency Himawari data for assimilation to improve forecasts of heavy rainfalls and typhoons (Kunii et al. 2016; Otsuka et al. 2015; Honda et al. 2018a, b; Sawada et al. 2019). Because low-level inflows trigger most heavy rainfalls that occurred in Japan from over the ocean (Kato 2018), observations over the surrounding sea that cannot be obtained from other than GEOs can be critical to forecasting such torrential rainfalls more accurately.

Although it is pointed out that assimilating frequently available infrared and visible observations from GEOs could give particular benefits for short-range forecasting (Geer et al. 2018), it is not straightforward for mesoscale NWP to deal with such a vast amount of high-resolution data in multi-channels, including cloud and precipitation-affected observations. In addition to the limited predictability of cloud formation and precipitation and the non-linear, discontinuous nature of moist atmospheric processes, direct assimilation of infrared and visible channels poses specific challenges for NWP due to the complexity of parameterizations in radiative transfer models (RTMs) and their overall computational costs (Okamoto et al. 2014; Li et al. 2017; Scheck et al. 2018). Among radiances derived from GEOs, only clear sky (not affected by clouds) infrared channels have been directly assimilated in operational NWP centres. While development towards the assimilation of all-sky radiances in operational NWP is being pursued (Okamoto 2017) and may be achieved soon in the case of infrared channels, most observations obtained by GEOs are currently discarded from the perspective of direct assimilation of radiances.

1.5. Atmospheric motion vectors

Besides infrared clear sky radiances (CSRs), atmospheric motion vectors (AMVs) have been a major component of GEO data assimilated in operational NWP. They are retrieved as wind vectors by tracking clouds and water vapor in consecutive satellite images. They have been used in NWP since as early as the 1970s to successfully identify synoptic air flows due to their wide coverage, including ocean areas. Because they are obtained as u- and v- components of wind that are also analysis and model variables, they do not need RTMs during the assimilation process nor extra computational costs for assimilating all-sky observations in both infrared and visible channels either. The disadvantage of assimilating retrievals such as AMVs is uncertainties added during the process of retrievals. For example, assigning a height to the tracked feature is one of the AMVs' most significant error sources (e.g., Salonen et al. 2015). It is essential to understand the error characteristics of different channels that depend on the retrieval algorithm and particular meteorological situations and adequately consider them in the DA system.

The Meteorological Satellite Center (MSC) of JMA attaches a quality index (QI) flag (Holmlund 1998) to each vector of AMV according to the recommendation by CGMS (Schmetz et al. 1999). *QI* takes a value between 0 to 1 and is a weighted sum of each *QI_i* that shows the consistency with the observation of a previous time, neighboring wind vector, model forecast wind, and others. A *QI_i* is a simple tanh-based function taking a value between 0 to 1. For example, *QI_dir* checks whether V_1, the wind vector obtained from the first and the second images among the three consecutive images that eventually produce AMV, and V_2, from the second and third images, are consistent in direction.

$$QI\_dir = 1 - \left[\tanh\left(\frac{Dif_{dir}}{A\exp\left(-\frac{V_{2s}}{B}\right) + C}\right)\right]^D , \qquad (1.12)$$

where Dif_{dir} is the difference of wind direction between V_1 and V_2, V_{2s} is the speed of V_2, and A, B, C and D are constant parameters (Hayashi and Shimoji 2013). A larger QI_dir means a better agreement between the two. Then QI is calculated as

$$QI = \frac{\sum W_i QI\_i}{\sum W_i}, \tag{1.13}$$

where QI_i is an individual test index, and its weight is W_i. Although a higher QI overall indicates a better quality, it may not work well when winds change in a relatively short span of space and time (Bedka and Mecikalski 2005). AMVs usually go through other QCs than QI flags before assimilation.

JMA/MSC operationally provides high-resolution AMVs derived from 10-min full-disk scans of Himawari-8 on a 20 km grid (at nadir) over the Japan region in six different channels, one visible, one near-infrared, and four infrared (including three water vapor) channels (Shimoji and Nonaka 2016). Because different infrared channels have sensitivities in different height ranges as their weighting functions show how the transmittance varies with height (Shimizu et al. 2017), AMVs can depict wind field profiles in the troposphere. These AMVs have been assimilated in the JMA's mesoscale DA systems since March 2016, together with global scale Himawari-8 AMVs with a 34 km resolution. Yamashita (2016) reported that they positively impacted analyses and improved the forecasts of typhoons and heavy rainfall cases.

Himawari-8 has enabled AMVs' production with even higher resolution derived from every 2.5-min rapid scans. Reducing the time interval between images can better capture the local-scale flow in the atmosphere, thus benefiting mesoscale NWP. Multi-functional transport satellites (MTSATs), the former JMA's geostationary satellites before Himawari-8, also conducted 5-min rapid scan operations and provided high-frequency AMVs only daytime in summer. Although some recent studies suggested assimilation of such rapid scan AMVs (RS-AMVs)

in mesoscale NWP improved the forecasts of heavy rainfalls and typhoon tracks (e.g., Kunii et al. 2016), the error characteristics of such high-resolution and multi-channel data have yet to be understood to fully utilize them in DA.

1.6. Optimal cloud analysis

Apart from the two major GEO products utilized for mesoscale DA, namely, CSR and AMV, cloud properties retrieved from radiances may be another candidate for DA. Some NWP centres have assimilated cloud properties such as cloud top pressure (CTP), cloud optical thickness (COT), or cloud fraction in mesoscale DA systems by adjusting humidity fields (e.g., Renshaw and Francis 2011). These cloud properties provide useful information on water vapor fields where clouds exist with a resolution as fine as a few kilometers. They are usually derived from infrared and visible radiances together with temperature profiles of models. Hayashi and Watts (2016) developed Himawari-8 Optimal Cloud Analysis (OCA), which employs the radiances of all sixteen channels of AHI to estimate CTP, COT, cloud effective radius (CRE), and cloud water path (CWP) through optimal estimation (Poulsen et al. 2012). Assimilation of OCA can also make use of the information from visible and near-infrared channels, while direct assimilation of radiations in such channels is far more complex than those in infrared channels and may not be achieved so soon in operational NWP.

1.7. Purpose of the study

This study investigates the nature and characteristics of the new-generation GEO data, which must be accounted for in assimilating into mesoscale NWP systems to produce better initial conditions in order to improve mesoscale forecasts. We focus on RS-AMV and OCA among the new GEO data as candidates to be used in mesoscale DA for better understanding wind and water vapor fields that caused

significant mesoscale weather events such as torrential rainfalls. Because RS-AMV and OCA are retrieved from visible and infrared radiances before assimilation, they have the advantages mentioned in Section 1.5 when utilized in mesoscale DA: fewer computational costs, and direct and easy-to-understand relationships with model variables. They are both newly developed products and still have difficulties being adequately utilized in NWP. While the recent studies mentioned in Section 1.4 suggested the potential benefits of using these data, their data characteristics have yet to be fully understood. Once optimally assimilated in NWP, they would contribute to constructing the state of the atmosphere more accurately with their finer resolution and wide coverage, improve the initial states for forecasts, and provide detailed analyses required for various meteorological and climatological research purposes.

In the following Chapters 2, 3, and 4, we evaluated their data characteristics through comparisons with other observations and model outputs, examined their error characteristic to construct a proper **R** described in Section 1.2 and to consider QC methods before assimilation, and test their performance and impacts on analysis and forecasts in several case studies. Our study focuses on data characteristics of these new data at this moment rather than the improvement of forecasts in real-time routine mesoscale NWP. We generally chose the cases for DA experiments to distinguish their impacts on assimilation results to see how their data representativeness and error characteristics affected reproduced meteorological fields through assimilation. The RS-AMV and OCA used in this study were still under-development products and produced on a trial basis. We somewhat arbitrarily selected the cases where RS-AMV and OCA seemed to capture atmospheric movement better than other observations, especially over the ocean. Introducing these new data into routine NWP may involve many more test cases in more

extended periods for assimilation and other necessary tunings in the system, which is beyond the scope of this study.

Chapter 1 includes some of Otsuka et al. (2019) and reviewed what has already been discussed in DA of GEO data in mesoscale NWP. The rest of the paper is structured as follows.

In Chapters 2 and 3, RS-AMVs were evaluated compared to other observations and models and used in assimilation experiments to see their impact on analysis and forecast fields. Chapter 2 utilizes RS-AMVs derived from MTSAT, the former JMA's satellite before Himawari-8, and focuses on how high-frequency observation and assimilation timing impacted the meteorological analysis and forecast fields on a heavy rainfall event in summer. Although MTSAT RS-AMV were obtained with a coarser horizontal resolution (about 0.5° in latitude and longitude) compared to those from Himawari-8 (about 0.04°) in this study, high temporal resolution (5 min) may still be beneficial to mesoscale DA if they could represent a small-scale movement of clouds and water vapor that then ordinary AMVs (30 min) failed to capture. No MTSAT RS-AMVs were obtained over land because there was not enough information to distinguish clouds from landscapes and other objects with such a low resolution in a few channels. For the same reason, it was also much harder to obtain low-level winds by MTSAT. In addition, the 5-min rapid scan of MTSAT was run only during the daytime in a few summer seasons. The heavy rainfall event for assimilation in Chapter 2 was mainly chosen as an example from a limited number of observations where MTSAT RS-AMVs seemed to represent the wind field from low to high levels near the stationary front in the sea better than ordinary AMVs. We attempted to assimilate them with JNoVA with as high a frequency as every 10 min for the first time. It required thorough understandings of their error characteristics to be taken into account for DA; in particular, observation error

correlations in time and space were statistically examined. The contents of Chapter 2 were cited from Otsuka et al. (2015).

Himawari-8 RS-AMV has overcome some of the defects of MTSAT RS-AMV. Firstly, AHI onboard Himawari-8 has an increased spatial resolution and a higher-spectral resolution from MTSAT. The rapid scan has been operated every 2.5 min for 24 hours every day. The advancement enabled higher-resolution RS-AMVs in 7 channels using a newly developed algorithm that was more suitable for high-resolution AHI (Shimoji 2014). As mentioned above, a few studies already assimilated Himawari-8 RS-AMVs on heavy rainfall events and suggested they were beneficial for the prediction. However, high-resolution multi-channel RS-AMVs may introduce other problems, including observation error correlations in conducting data thinning and data selection before assimilation (Kunii et al. 2016), which cannot be solved without thorough knowledge about their data characteristics. Chapter 3 describes the error characteristics of Himawari-8 RS-AMV through data verification and assimilation experiments and discusses how these high-resolution and multi-channel wind observations can be better utilized in future mesoscale NWP. We examined how different error characteristics from different channels affected wind analysis and forecast fields in a cold vortex event in northern Japan as a case example. Chapter 3 was cited from Otsuka et al. (2018).

Although we saw the potential of RS-AMVs to improve mesoscale wind fields and provide better initial conditions for short-range forecasts in Chapters 2 and 3, it seemed not enough to predict heavy rainfall cases where water vapor transportation from the sea play a key role. In Chapter 4, we targeted water vapor observations by Himawari-8. Chapter 4 describes data evaluation of Himawari-8 OCA and their utilization in assimilation experiments on heavy rainfall events to see their impact on water vapor analysis fields and the extended forecasts in the later hours. We chose three heavy rainfall cases caused by stationary rainbands and typhoons, where

southerly inflows of moist air from the sea might have triggered the torrential rainfalls. Chapter 4 was based on Otsuka et al. (2021). Finally, we present our general summary in Chapter 5, which also includes a part of Otsuka et al. (2019).

Chapter 2

Assimilation experiments of MTSAT rapid scan atmospheric motion vectors on a heavy rainfall event

2.1. Introduction

The Multi-functional Transport Satellite (MTSAT-1R), a geostationary satellite of the Japan Civil Aviation Bureau and JMA, began rapid-scan operations in 2011 and provided images of Japan and the neighboring area (from 20°N, 120°E to 50°N, 150°E) as frequently as every 5 min during the daytime in summer for the purpose of monitoring severe convective weather, volcanic ash plumes, and other phenomena that might affect air traffic. JMA MSC produced RS-AMVs, which are wind vectors derived from three consecutive RS images by tracking the spatial distributions of clouds and water vapor in the atmosphere. Because of the high frequency of observations, RS-AMVs increased the amount of data available, and they were also expected to capture atmospheric movements that were too short-lived to be depicted by routine hourly AMVs (RTN-AMVs), which were derived from images obtained at 15-, 30-, or 60-min intervals.

Because AMVs have good spatial and temporal coverage even over the ocean where other wind observations are scarce, they have been widely used since as early as the 1970s in national forecast centres around the world (Menzel 2001). Their impact on forecasts can be significant when assimilated by NWP systems (Tomassini et al. 1999; Rohn et al. 2001; Zapotocny et al. 2008; Ishibashi 2011; Joo et al. 2013). Although they are mainly used to identify air flows at the synoptic-scale for the purpose of data assimilation, especially for global-scale models, AMVs can also be used to identify mesoscale winds associated with convective clouds at much finer spatial and temporal scales (Bedka and Mecikalski 2005). Because the

movements of low cumulus and stratocumulus clouds are not necessarily consistent with environmental winds, which are generally obtained by tracking high-level clouds, mesoscale AMVs may be excluded from data sets by quality control processes and thus not be fully utilized in current NWP systems. Nevertheless, these small cloud movements can carry useful information regarding the initiation and development of mesoscale convections, so it is worthwhile to explore the possibility of improving mesoscale forecasts by assimilating them.

Earlier studies have suggested that many good-quality AMVs, especially those at low levels that represent mesoscale cloud movements, can be obtained by RS operations. Fujita et al. (1975) showed that the optimal scan time interval for computing wind vectors depends on the horizontal scale of the clouds that are used for tracking. Saito and Takano (1986) showed that low-level AMVs derived from images obtained at short time intervals by Geostationary Meteorological Satellite-3 satisfactorily captured the characteristic wind field near a cyclone or a sub-synoptic scale cold front than those derived from images obtained at 30-min intervals. Velden et al. (2005) compared AMVs from 5-, 10-, 15-, and 30-min imagery and concluded that the optimal time interval for retrieval was 5 min for visible-channel winds and 10 min for infrared winds. In addition, Johnson and Suchman (1980) reported that the number of low-level wind vectors calculated from 3-min RS imagery of the Geostationary Operational Environmental Satellite (GOES) was almost ten times the number of wind vectors derived from the 30-min imagery.

Techniques for assimilation of geostationary satellite data with high temporal resolution have been improving in recent years (Munro et al. 2004; Peubey and McNally 2009; Berger et al. 2011; Okamoto 2013; Wu et al. 2014). Yamashita (2010) reported that track forecast errors for typhoon SINLAKU were reduced by 9 %–12 % on average by the assimilation of RS-AMVs in the experiments conducted during the THORPEX Pacific Asian Regional Campaign 2008 (Nakazawa et al.

2010). Langland et al. (2009) conducted assimilation experiments for Hurricane Katrina in 2005 and showed that the track forecast was improved when AMVs from 5-min GOES imagery were assimilated. However, not many investigations have examined the impacts of RS-AMVs on observation system experiments; instead, RS data seem to be primarily used for forecasting or monitoring. Considering the future possibility of obtaining high-quality RS-AMVs from Himawari-8 and the development of assimilation techniques for cloud-resolving models, it is worthwhile to examine the characteristics of RS-AMVs and to develop optimal methods for assimilating them into NWP models.

The purpose of this study was to investigate the advantages of assimilating RS-AMVs into a mesoscale NWP system for better forecasting of mesoscale phenomena such as heavy rainfall events. First, the quality of RS-AMVs was evaluated in terms of their consistency with NWP forecast winds. Forecast winds obtained from the JMA Non-Hydrostatic model (NHM; Saito et al. 2006) with a 2-km horizontal resolution in the area east of Japan were compared with RS-AMVs every 10 min. Next, experiments in which RS-AMV data were assimilated were performed for a heavy rainfall event that occurred in summer using the JMA NHM-based 4D variational data assimilation (4D-Var) system (JNoVA; Honda et al. 2005) with a 5-km resolution.

The rest of this chapter is organized as follows: Section 2.2 describes the experimental system and verification measures used in the study. Section 2.3 presents the results, and Section 2.4 presents a summary and our conclusions.

2.2. Data and methods

2.2.1. AMV data

The RS-AMVs used in this study were derived from MTSAT-1R RS imagery obtained every 5 min by infrared-1 (IR1, 10.8 μm), water vapor (WV, 6.8 μm), and

visible (VIS, 0.63 μm) channels. They were computed using the same procedures as RTN-AMVs, except for using shorter time intervals, by pattern-matching techniques based on cross-correlation statistics for tracking targets (Leese et al. 1971; Hamada 1979). The details of the AMV retrieval algorithm used at the MSC are described by Hayashi and Shimoji (2013). AMVs at upper or middle atmospheric levels were obtained by tracking high- or mid-level clouds such as cirrus clouds or water vapor using IR1 and WV channels, and lower-level AMVs target cumulus and other low-level clouds in the IR1 and VIS imagery. The horizontal resolution of the AMV data set was 0.5°of latitude and longitude, and each AMV target box was 16 pixels × 16 pixels or 32 pixels × 32 pixels (per pixel resolution, 1 and 4 km at nadir for VIS and IR1/WV, respectively). The observation height was determined by comparing the infrared brightness temperature of the target box with a vertical temperature profile computed by a fast radiative transfer model using the first-guess field (forecasts of previous forecast analysis cycles) from a global spectral model (GSM) as input and taking into account attenuation by the atmosphere along the path. A quality indicator flag (QI; Holmlund 1998) developed by the European Organization for the Exploitation of Meteorological Satellites attached to individual AMV data indicates the data quality; the QI value is based on consistency checks with the GSM first-guess field, neighboring wind vectors, and previous observations: the better the data agree with these, the higher the QI value and the better the data quality. Other quality control procedures within the retrieval algorithm, which remove gross errors and perform internal consistency checks of various parameters during the tracking process and height assignment, are described by Hayashi and Shimoji (2013).

2.2.2. Verification of AMV data

We examine the quality of the RS-AMVs and their characteristics by calculating first-guess departure statistics (observation minus the NWP model first

guess) before using them for data assimilation. RS-AMVs were compared with the forecast winds obtained every 10 min by the JMA NHM with a horizontal resolution of 2 km during August 2011, excluding the period from 3 to 16 August. During this period, no RS data were obtained because MTSAT-1R was performing the routine operations of MTSAT-2, which was having mechanical troubles. Comparisons of AMV data with the first-guess field provide overall estimates of the observation error characteristics of different channels, in particular, whether the distribution of the first-guess departures is Gaussian-like. This information is critical for determining whether the data are appropriate for assimilation because most data assimilation schemes, including the 4D-Var system used in this study, assume Gaussian distributions of the observation errors. Yamashita (2012) calculated similar statistics by hourly comparing both RS-AMVs and RTN-AMVs with the NHM first-guess field, which had a horizontal resolution of 5 km. Because we intended to assimilate RS-AMVs as frequently as every 10 min and to perform forecasts with a horizontal resolution of up to 2 km in this study, the comparison is performed at higher temporal and spatial resolutions compared with a similar study by Yamashita (2012).

The NHM forecast domain was selected to include mainly eastern Japan (33°N, 135°E to 38°N, 142°E), and its horizontal resolution was 2 km (350 × 350 grid points) with 60 vertical levels. A 15-h forecast from the initial time 2100 UTC was conducted every day of August 2011 using 3-h JMA meso analyses as initial and boundary conditions. NHM forecast winds were obtained every 10 min. The RS-AMVs were compared with the nearest forecast winds, which were vertically interpolated to a pressure level that is closest to the RS-AMV assigned height. The AMVs with QI values larger than 0.85 were used in this comparison according to operational MSC recommendations. As indicators of the differences between the RS-AMVs and NHM forecast winds, we calculated the mean error (ME), root mean

square difference (RMSD), and root mean square vector difference (RMSVD) as follows:

$$ME = \frac{1}{N}\sum_{n=1}^{N}\left(\sqrt{{u_n}^2 + {v_n}^2} - \sqrt{{U_n}^2 + {V_n}^2}\right), \tag{2.1}$$

$$RMSD = \sqrt{\frac{1}{N}\sum_{n=1}^{N}\left(\sqrt{{u_n}^2 + {v_n}^2} - \sqrt{{U_n}^2 + {V_n}^2}\right)^2}, \tag{2.2}$$

$$RMSVD = \sqrt{\frac{1}{N}\sum_{n=1}^{N}[(u_n - U_n)^2 + (v_n - V_n)^2]}, \tag{2.3}$$

where N is the number of RS-AMVs used to calculate the statistics, u_n and v_n are zonal and meridional wind components of the RS-AMVs, and U_n and V_n are zonal and meridional wind components of the NHM forecast wind, respectively. ME and RMSD indicate the differences in wind speed between the AMV observations and first-guess field, whereas RMSVD indicates their differences in both wind direction and speed. Smaller values of these indicators are considered to correspond to better quality RS-AMV data.

The verification of RS-AMV was performed using the data collected in August 2011, while the estimation of observation error correlations and the data assimilation experiments were conducted with data collected in August 2012 (Sections 2.3 to 2.4). There were no changes in the retrieval algorithm of RS-AMV during the 2011–2012 period. We regarded that the verification in 2011 was relevant to the data in 2012 used for assimilation.

2.2.3. Data assimilation system and estimation of observation error correlations

In this study, the experiments were conducted using the JNoVA data assimilation system. JNoVA is the incremental 4D-Var system for mesoscale

analysis used operationally at JMA, and its incremental formulation is based on Courtier et al. (1994). The modified version of the JNoVA system used in this study is shown schematically in Fig. 2.1. The high-resolution outer loop model (5-km horizontal resolution, 50 vertical levels) is used for the computation of the first-guess field, and the low-resolution inner loop model (15-km horizontal resolution and 40 vertical levels) is used to solve the iterative minimization problem. Pre-analysis procedures such as data selection through QI numbers, data thinning, and various QC checks are applied before analysis. JNoVA is able to assimilate a wide variety of observational data within a 3-h time window, including surface, upper air, radar, satellite, and ground-based Global Navigation Satellite System data (JMA 2013). In addition, RS-AMVs were assimilated in the experiments, whereas RTN-AMVs, which are assimilated in operational use, were excluded so that the impacts of the RS-AMVs could be distinguished. The JNoVA system was modified to collect 5-min RS-AMVs into 10-min time slots instead of the 1-h time slots used operationally for the other observation data. Thus, calculations of the first-guess departures and quality control of the RS-AMV observational data were conducted every 10 min.

Assimilating high-density data without considering possible spatial correlations of observation errors can cause degradation of the analysis results (Liu and Rabier 2003). To avoid this problem, a common approach taken in operational data assimilation systems is to spatially thin the observations. In the operational version of JNoVA, satellite observations, including RTN-AMVs, are thinned so that they are no closer than 2° (approximately 200 km) in the horizontal and 100 hPa in the vertical within each 3-h window. Because RS-AMVs are expected to represent smaller-scale winds, the threshold distance for thinning where correlations between the observation errors become small enough to be neglected might be shorter than that in the case of RTN-AMVs, as reported in Yamashita (2012). For optimal use of

these new data for assimilation, it was necessary to estimate the degree of observation error correlation to determine the optimal thinning scale.

To estimate observation errors and their correlations, we used the Hollingsworth–Lönnberg method (Bormann and Bauer 2010), which is based on the first-guess departure statistics. Observation error correlations were estimated by calculating covariances of pairs of first-guess departures as a function of their separation in space and time. The statistics of departures from three sequential JNoVA cycles, run from 0000 to 0900 UTC every day of August 2012 when RS-AMVs were available, were calculated. To increase the departure sample size, the horizontal scale of RS-AMV thinning was reduced to 0.5°, which is equal to the observational resolution; as a result, almost all of the RS-AMVs were eventually used to calculate the statistics. Correlations between pairs of observations within the same 3-h time window were calculated and binned by the spatial and temporal distance between the two observations, and the contents of each bin were averaged. Binning intervals were every 25 km (0–200 km) or 50 km (200–500 km) in horizontal distance and every 10 min in time.

2.2.4. Assimilation experiments and precipitation forecast verification

Assimilation experiments were performed for a precipitation event associated with a front that moved slowly across the Japan Sea on 13 August 2012 and brought locally heavy rainfall over some parts of western Japan. In the experiments, three forecast analysis cycles of JNoVA, each with a 3-h window, were run during the daytime (0000–0900 UTC), when RS-AMVs could be obtained and assimilated. Then, using the analyses at 0900 UTC as initial conditions and the JMA GSM forecasts as boundary conditions, a 15-h forecast was performed with a horizontal resolution of 2 km (350 × 350 grid points) and 60 vertical levels. The JNoVA and NHM forecast domains are shown in Fig. 2.2. RS-AMVs were assimilated in four

different experiments (four test cases) with different combinations of time slot length and time interval of spatial data thinning. In addition, a control run was executed without assimilation of RS-AMVs. We then compared the test cases with each other to determine how different experimental configurations affected the results and with the control run to identify the impacts of RS-AMV assimilation.

We evaluated the impact of RS-AMVs on forecast results by comparing precipitation forecasts against observations. In the experiments, the forecast precipitation data obtained at the original model resolution of 2 km were mapped onto a 5-km grid for comparison with radar/rain gauge-analyzed precipitation (RAP) data with the latter resolution. RAP is an operational precipitation observation product of JMA that covers all of Japan; it is based on radar measurements that have been calibrated using data from around 10,000 rain gauges. To verify the forecast results of each experiment, we computed index scores based on dichotomous forecast results arranged in a contingency table. In the contingency table, the frequencies of the four possible combinations of "yes" and "no" forecasts and observations are tabulated: hit (yes forecast, yes observation), miss (no forecast, yes observation), false alarm (yes forecast, no observation), and correct rejection (no forecast and no observation). Then, to evaluate how well the forecast predicted precipitation in each grid cell, we computed the threat score (TS) and bias score (BS):

$$TS = \frac{hits}{hits + misses + false\ alarms}, \tag{2.4}$$

$$BS = \frac{hits\ +\ false\ alarms}{hits\ +\ misses}. \tag{2.5}$$

2.3. Results

2.3.1. Verification of RS-AMVs

RS-AMVs were compared with NHM forecast winds at 10-min intervals for August 2011, as described in Section 2.2.2. The numbers of RS-AMVs obtained in the whole RS area in August by the IR1, WV, and VIS channels are shown according to pressure level in Fig. 2.3. The number of wind vectors at levels above 400 hPa was much larger than the number of wind vectors at levels below 700 hPa, and very few mid-level (400–700 hPa) RS-AMVs were obtained. The AMV retrieval algorithm used by the MSC does not allow computation of lower-level winds over land, because it is difficult to distinguish orographic cloud movements from representative wind vectors. Thus, the sample size of lower-level winds available for computation of the error statistics was much smaller than that of upper-level winds.

Overall, the distributions of the differences between RS-AMV and NHM wind speeds (Fig. 2.4) have Gaussian-like shapes, which means that the quality of the RS-AMV data is sufficient for 4D-Var assimilation, though a slight negative bias can be seen in the distribution of the IR upper and middle winds (Fig. 2.4a), and a positive bias can be seen in that of the VIS lower winds (Fig. 2.4d).

The error statistics for the RS-AMVs and RTN-AMVs are shown in Tables 2.1a and 2.1b, respectively. Because of the lower temporal resolution of RTN-AMVs, the sample sizes of RTN-AMVs were much smaller than those of RS-AMVs. The RMSDs of IR and WV middle- and upper-level winds of the AMVs compared with NHM winds were similar between RS-AMVs (around 3.5 m s^{-1}) and RTN-AMVs, but the RMSDs of the latter were slightly lower. The same was true for RMSVDs between RS-AMVs and RTN-AMVs. Yamashita (2012) calculated similar statistics to describe the first-guess departures of RS-AMVs and RTN-AMVs derived by the same MSC algorithm used in this study and found that standard deviations of RS-AMVs were slightly larger than those of RTN-AMVs for both upper- and lower-

level winds, which is consistent with the results of this study. In ME, RTN-AMV IR1 winds at all levels showed significant negative biases, and these biases were alleviated in RS-AMV IR1 winds. This bias toward wind speeds lower than the observed is a well-known problem that has been attributed to either height-assignment or tracking errors (Bresky et al. 2012). The results of this comparison with NHM forecast winds show that the quality of RS-AMVs is as high as that of RTN-AMVs, and that they are equally suitable for use in the operational 4D-Var assimilation system. In this study, we did not compute error statistics between RS-AMVs and wind observations from sonde, aircraft, or other observational networks. Yamashita (2012) has already shown that RS-AMVs agree well with collocated sonde and aircraft wind observations. The correlation coefficient of 0.91 was as high as the correlation coefficients between the RTN-AMVs and collocated sonde (0.90) and aircraft (0.91) wind observations. In addition, the MSC routinely compares AMVs with sonde wind observations, following the recommendations of the Coordination Group for Meteorological Satellites and reports the results on a monthly basis. These MSC statistics show average differences (RMSVDs) of 5–8 m s^{-1} for upper-level winds and of up to 4 m s^{-1} for lower-level winds (Hayashi and Shimoji 2013).

2.3.2. Observation error correlations and data thinning scale

Figure 2.5 shows the averaged correlation values of pairs of RS-AMV observations extracted from the three daily forecast analysis cycles during August 2012, binned by the separation distance, as described in Section 2.3.1. As expected, the correlation coefficient decreases with increasing distance. Liu and Rabier (2003) indicated that the error correlation between two adjacent observations greater than the threshold value (around 0.2) degrades the analysis and forecast. If a maximum correlation value of around 0.2 is considered optimal for determination of the

thinning scale, then the minimum thinning distance is within 100–200 km, which is below the 200-km threshold currently used operationally. Therefore, it seems feasible in the case of RS-AMV observations to reduce the distance threshold for thinning from 200 km to around 150 km in order to increase the amount of data available.

When the correlation values shown in Fig. 2.5 were binned and averaged by time intervals between observation pairs and distance intervals (Fig. 2.6), they did not necessarily decrease for longer time intervals, contrary to expectation; this result may be due to noise by the small sample size or other unknown reasons. When the spatial distance was ≤ 150 km, correlation values as high as 0.5 were seen in almost all the time bin range. In contrast, correlation values were ≤ 0.3 at spatial distances of over 150 km, with few exceptions even when the time interval was short (10–30 min). Consequently, we considered only spatial observation error correlations in the assimilation experiments conducted in this study, and we assumed that temporal observation error correlations were not significant provided that the distance between observations was sufficient. Therefore, we decided to thin the data density to 1.5°, approximately 150 km, for the assimilation of RS-AMVs.

2.3.3. Data assimilation experiments with RS-AMV

Assimilation experiments were performed by utilizing RS-AMVs for a heavy rainfall event that occurred in western Japan on 13 August 2012. The weather chart at 0000 UTC on that day showed that there was a stationary front over the Japan Sea that extended as far as the Korean Peninsula and the eastern coast of the Asian continent (Fig. 2.7). As the front slowly moved southward from 13 to 14 August, the warm, humid air transported from the south was responsible for heavy rainfalls in many parts of western Japan. A combined IR/VIS image at 0005 UTC on 13 August (Fig. 2.8) distinctly showed a convective cloud band corresponding to the front. In

5-min RS imagery, the cloud band streamed from southwest to northeast while gradually shifting southward, and bands of low cumulus clouds over the East China Sea, off the western coast of Kyushu, moved up toward the front from the southwest. The lower-level AMVs associated with these cloud motions indicated southwesterly winds in the area of the cumulus clouds, and many upper-level AMVs, representing the jet stream, were recognized in the vicinity of the front. The distribution of upper-level RS-AMVs that were assimilated in the experiments during 0000–0900 UTC off western Kyushu includes some divergent upper-level flows (Fig. 2.9, circled), and the lower-level distribution indicated inflows toward the front. We investigated how this characteristic wind field introduced by the assimilation of RS-AMVs influenced forecasts by conducting data assimilation experiments.

Experiments were conducted for four test cases in which RS-AMVs were assimilated during nine daytime hours (0000–0900 UTC), i.e., three JNoVA cycles. In each test case, the analysis results at 0900 UTC were used as the initial conditions, and a 15-h forecast was obtained. The lengths of assimilation time slot and data thinning intervals were varied among the four test cases (Table 2.2). The forecast results of each experiment were compared with a control experiment (CNTL, no assimilation of RS-AMVs). In the RSAMV10_10min experiment, the RS-AMVs were collected into 10-min time slots and assimilated 18 times in the 3-h assimilation window, and spatial thinning was applied every 10 min. In the RSAMV10_3h experiment, although the RS-AMVs were also assimilated in 10-min time slots, spatial thinning was not performed until the end of the 3-h window, i.e., after all RS-AMVs had been collected. In contrast, in the RSAMV_1h and RSAMV_3h experiments, the RS-AMVs were assimilated in 1-h time slots, and spatial thinning was performed at 1 and 3 h, respectively. In all experiments, the same horizontal thinning scale (1.5°, approximately 150 km) was applied. As shown in Section 2.3.2, the observation error correlation values in both space and time were acceptable when

a 10-min time slot was combined with data thinning at 3 h (RSAMV10_3h) provided that the data were thinned to 150 km. However, because of the possibility that 3-h data thinning might reduce the amount of unique information obtained using high-frequency RS-AMVs, we also conducted an experiment that combined 10-min assimilation with a 10-min thinning interval (RSAMV10_10min), which almost doubled the amount of available data compared with RSAMV10_3h. Because RTN-AMVs and other observations are assimilated hourly and thinned every 3 h in the operational model, we also examined hourly RS-AMV assimilation and 3-h thinning (RSAMV_1h and RSAMV_3h). We compared these four test cases with each other and with CNTL to determine the optimal strategy for RS-AMV assimilation by the JNoVA system.

Threat scores (TSs) and bias scores (BSs) averaged over the whole forecast period of 15 h for 3-h precipitation thresholds (0.1, 1, 3, 5, 10, 15, 20, 25, 30, 35, 40, 45, and 50 mm) are shown in Fig. 2.10. In the test runs, except for RSAMV_3h, with RS-AMV data, most TSs were improved compared with CNTL (Fig. 2.10a). In RSAMV10_10min, in particular, TSs were higher for precipitation thresholds ranging from 0.1 to 30 mm, compared with both CNTL and the other test cases. For almost all precipitation thresholds, TSs were better in RSAMV10_3h than in RSAMV_3h. The length of assimilation time slot is the only different factor between RSAMV10_3h and RSAMV_3h, suggesting that assimilating RS-AMVs at shorter time intervals and comparing the first-guess field and observations with a relatively shorter time lag might have a positive impact on mesoscale forecasts. In addition, RSAMV10_10min scores were better than RSAMV10_3h scores. Spatial thinning of the observations was applied every 10 min in RSAMV10_10min, whereas thinning was applied to all observations assimilated within the 3-h assimilation window in RSAMV10_3h. Excessive thinning in the latter experiment was likely responsible for the relatively poor TSs. The BSs of all four test experiments were

much larger than 1.0 for precipitation thresholds above 30 mm, indicating that the assimilation of RS-AMVs resulted in over-forecasts when rainfall was heavy (Fig. 2.10b). We next compared TSs and BSs for the 10-mm precipitation threshold as a function of forecast time (FT, Fig. 2.11). In RSAMV10_10min, both scores were better at FT03 (3 h FT), and the TS was also better at FT06, compared with CNTL and the other tests. However, the BS at FT06 was worse than the CNTL BS. Because the verification results of RSAMV10_10min showed a better overall performance than the other tests, we selected RSAMV10_10min (hereafter called TEST) for further comparisons with CNTL to assess the impact of RS-AMV assimilation on forecasts.

Next, we examined differences in the analysis results between TEST and CNTL. Many upper-level RS-AMVs in the vicinity of the front were assimilated at near 250 hPa, whereas lower-level RS-AMVs were assimilated at around the 850 hPa level. We therefore compared wind speed and wind vectors in the analyses at 250 and 850 hPa and at the surface with those of CNTL (Fig. 2.12). Winds were slightly different from CNTL at 250 hPa in the vicinity of the front, and increased divergence was observed in some areas near the front (Fig. 2.12a, green contours marked with a plus sign). At 850 hPa, southerly and southwesterly wind speeds were increased (Fig. 2.12b, the area circled with a dotted line), corresponding to the observed and assimilated flows toward the front, shown in Fig. 2.9; westerly wind speeds were also increased along the coast near the front (circled with a solid line), between Chugoku and the Korean Peninsula. Significant differences were also observed in the wind field at the surface. In particular, the wind vectors show intensified convergence in the coastal area off Chugoku (Fig. 2.12c, enclosed by an ellipse). In addition, the water vapor mixing ratio at 500 m above the surface (Fig. 2.12d) was increased in the area north of where the upper-level divergence and lower-level inflow were observed in Fig. 2.9 (enclosed by a circle in Fig. 2.12d).

We next examined differences in the forecast results between TEST and CNTL. In Fig. 2.13, forecasts of the hourly amount of precipitation at every 3 h (FT = 03, 06, 09) by TEST and CNTL are shown along with RAP observations at the corresponding times. Although no obvious differences are seen between TEST and CNTL in terms of distribution and timing of rainfall during the whole forecast period, rainfall amounts were slightly higher in TEST. Both the TEST and CNTL forecasts show a rain band that stretches from west to east along the coast at FT03 and moves southward at FT06 and FT09, matching the observations well, although small areas with weak rainfall around Kyushu at FT03 and the sharp linear rain band at FT06 seen in the observations are not accurately illustrated. The rainfall amount in the coastal area off Chugoku was increased in TEST at FT03 and FT06 from CNTL. As mentioned earlier, the verification results (Fig. 2.11) showed that, compared with CNTL, the precipitation forecasts of TEST at FT03 and FT06 were improved, as indicated by its TSs and BSs. The assimilation of RS-AMVs apparently changed the initial wind field by intensifying the frontal system at the surface. Consequently, an increased amount of precipitation was forecast.

2.4. Summary and conclusions

We evaluated the quality of RS-AMVs obtained using new MTSAT-1R RS imagery and the impact of their assimilation on a mesoscale forecast of a precipitation event along a stationary front in western Japan. First-guess departures (RMSDs) of the RS-AMVs, obtained every 10 min, from 2-km NHM forecast winds were on average around 3.5 m s^{-1} for upper-level winds and 2.0 m s^{-1} for lower-level winds. The distributions of wind speed differences between observations and forecasts were generally Gaussian-like. However, a slight negative bias in IR middle- and upper-level winds and a positive bias in VIS lower-level winds were recognized. These results did not differ significantly from those obtained by

comparing NHM winds and RTN-AMVs in operational use, so we consider the quality of the RS-AMVs to be sufficiently high to be used with JNoVA. The advantage of RS-AMVs over RTN-AMVs is the increased data volume by shortening the time interval used in the retrieval algorithm. In the future, the algorithm should be improved, e.g., narrowing the target area without degrading the tracking accuracy or by assigning height more accurately, so that more detailed information can be extracted from the RS imagery. Furthermore, there is room for improvement in the current quality control procedures, which depend primarily on QI values. Some data with small QI numbers may represent local features but fail to pass the quality control step and be rejected.

Next, we examined and modified some procedures of the current assimilation system in order to exploit the high-resolution RS-AMV data. We estimated observation error correlations and determined that the optimal horizontal thinning scale was 150 km, somewhat shorter than the 200-km threshold currently used operationally, thus allowing more data to be assimilated. The temporal observation error correlations were neglected in this experiment provided an appropriate horizontal thinning scale was used; however, this issue should be explored further in the future. We also evaluated the effect of shortening the assimilation time slot length with different data thinning intervals by verifying precipitation forecasts of the selected rainfall event from four assimilation experiments. We concluded that a 10-min assimilation time slot length with data thinning at 10-min intervals (TEST) yielded the best results among the experiments.

We evaluated the impact of RS-AMV assimilation by comparing differences in the analysis and forecast results between TEST and CNTL (no RS-AMV assimilation). The rainfall event on 13 August 2012 followed a pattern of typical of heavy rainfall associated with a stationary front over the Japan Sea, one that is often seen during the Meiyu or early autumn rainy season. The RS-AMVs that were

obtained and assimilated in the area of interest exhibited a characteristic wind field in the vicinity of the front, including jet stream and divergent winds at the upper level and inflows toward the front at lower levels. These characteristics matched very well with cloud movements that could be clearly recognized in the RS imagery. The analysis results showed that RS-AMV assimilation increased surface wind convergence and higher water vapor mixing ratios near the surface, and in the early forecast results, RS-AMV assimilation resulted in an intensified front and an increased amount of precipitation compared with CNTL. More case studies are required to further characterize the influence of assimilating RS-AMVs on precipitation forecast.

Assimilation of RS-AMVs may have a positive impact on the timing and intensity of heavy rainfall forecasts because of their high resolution and the capability to track clouds more accurately, especially at low levels. If lower-level RS-AMVs could be obtained over not only the ocean but also land areas for the depiction of small-scale features of low-level flows, it might be possible to improve the forecast on the development of severe local convections. To utilize RS-AMVs more effectively in NWP, improved assimilation techniques for data quality control, data thinning, and the estimation of observation error correlations are required, and AMV-retrieval algorithms more suitable for high-resolution RS observations should be developed.

Chapter 3

Characteristics of Himawari-8 rapid scan atmospheric motion vectors utilized in mesoscale data assimilation

3.1. Introduction

JMA MSC began routinely computing AMVs using imagery from their first geostationary meteorological satellite in 1978, and the JMA started to use them in their NWP system the next year. Advances in both satellites and NWP systems over the years have made more highly spatial and temporal AMV datasets available for assimilation into operational NWP systems with finer model resolutions. AMVs are considered to be useful for representing local-scale flow in mesoscale systems as well as synoptic winds in global systems (Bedka and Mecikalski 2005; Velden et al. 2005; Bedka et al. 2009). Now that recent satellites such as Himawari and the Geostationary Operational Environment Satellite (GOES) series are operated in rapid scan (RS) mode, the possibility of producing even higher temporal resolution AMVs is expanding.

The benefits of reducing the time interval between images for computing AMVs have been discussed in earlier studies as described in Chapter 2. Among recent studies that use RS imagery from multifunctional transport satellites (MTSAT-1R and 2R), Oyama et al. (2016) showed that upper tropospheric AMVs can be used to detect the intensification, and Hamada and Takayabu (2016) estimated vertical velocities at the convective cloud top.

Furthermore, attempts to assimilate high-resolution RS-AMVs into NWP systems to improve forecasts of tropical cyclones have been getting more attention. MTSATs conducted RS operations during the summers of 2011–2014 and some other periods, and RS-AMVs were produced accordingly by MSC. MTSAT RS-

AMVs derived from three images at 5-min intervals proved to be useful in global and mesoscale assimilation and typhoon analyses in some studies as described in Chapter 2. Berger et al. (2011) and Wu et al. (2014, 2015) investigated the impact of assimilating enhanced AMVs processed by the Cooperative Institute for Meteorological Satellite Studies (CIMSS, University of Wisconsin–Madison) from MTSAT RS imagery obtained for the THORPEX Pacific Asian Regional Campaign in 2008 (Nakazawa et al. 2010).

Since July 2015, with additional varieties of channels and improved sensor performance, Himawari-8 has been able to produce higher resolution AMVs such as hourly computed AMVs from 10-min full disk scans for routinely operated NWP systems (RTN-AMV) and RS-AMVs from 2.5-min rapid scans. Assimilation of Himawari-8 RTN-AMVs into the JMA's operational global and mesoscale NWP systems positively impacted analyses and improved typhoon and rainfall forecasts (Yamashita 2016). The assimilation of Himawari-8 RS-AMVs by an ensemble Kalman filter implemented with a regional mesoscale model improved precipitation forecast scores for a heavy rainfall event (Kunii et al. 2016) and wind forecasts in another case study (Otsuka et al. 2016). Although these results suggest that the impacts of Himawari-8 RS-AMVs on mesoscale forecasts are positive and promising, they still seem to be case dependent since there is no established method for making better use of such a large amount of high-resolution RS-AMV data and their data representativeness and error characteristics are not sufficiently taken into account. It is necessary to understand more about the features and qualities of RS-AMV data before developing optimal methods for data selection, data thinning, quality control, and other pre-processing procedures to utilize them more efficiently in a mesoscale NWP system. In addition to the increase in resolution and frequency, Himawari-8 RS-AMVs are available in more channels than MTSAT RS-AMVs, including the two new water vapor channels (WV) and the CO_2 absorption channel

(CO_2). The data characteristics of RS-AMVs in each channel had not yet been fully examined in the previous studies. We also need to study the characteristics of different channels and provide useful information so as to better handle these multi-channel RS-AMVs in the assimilation system.

The purpose of this study was to clarify the data characteristics of RS-AMVs in terms of their use in mesoscale data assimilation for the improvement of short-range forecasts. First, their data quality and observation error characteristics were examined based on the statistics of the differences from JMA mesoscale analyses, radiosonde, and wind profiler observations, and JMA-NHM forecasts. Next, assimilation experiments were conducted for a mesoscale cold vortex event to investigate the impacts of RS-AMVs on the analyses and forecasts and to see how the data characteristics were reflected in the results of the assimilation.

The rest of the chapter is structured as follows. Section 3.2 describes the data verification and error characteristics of RS-AMVs, Section 3.3 describes the assimilation experiments, and Section 3.4 provides the discussion. Finally, we present our conclusions in Section 3.5.

3.2. Verification and error characteristics of RS-AMVs

3.2.1. Data verification

a. Data and methods

Himawari-8 RS-AMVs were derived from image triplets at 2.5-min intervals for the visible (VIS) channel and at 5-min intervals for the near-infrared and infrared (IR) channels, three WV channels, and the CO_2 channel, extracted from 2.5-min rapid scan observations over two rectangular areas around Japan (Fig. 3.1). They were computed every 10 min for each of the seven channels of the Advanced Himawari Imager (AHI) using the same AMV software used for RTN-AMVs, which was developed to adapt to the high spectral, spatial, and temporal resolutions of the

AHI (Shimoji 2014). Figure 3.2 shows the number of RS-AMVs by pressure level for the month of June 2016. As mentioned in Shimoji and Nonaka (2016), improvements in cloud feature tracking and cloud height assignment methods in the software and the increased number of channels enabled Himawari-8 to produce many more low- and middle-level winds as well as additional high-level winds than previous satellites. It should be noted that low-level winds over land finally became available because the high resolution of the AHI made it possible to distinguish cloud movements from land features. The horizontal resolution of the RS-AMV dataset was about 0.04° in latitude and longitude, and the target box size used for cloud tracking in the computation was 5 pixels × 5 pixels. The total number of data for the month was more than 20 times the number of RTN-AMVs, owing to the higher space and time resolution of the RS-AMV data.

Because each channel of the AHI has a unique specification and sensitivity to atmospheric conditions as described in Bessho et al. (2016), RS-AMVs of different channels are expected to represent wind fields with different horizontal scales and at different heights. For example, high clouds such as cirrus or water vapor features with relatively large horizontal scale are tracked in mid- to upper air in IR or WV for the retrieval of AMVs, while local cumulus clouds are targeted in VIS and IR at low levels. It is necessary to understand their data characteristics before putting them to use for assimilation. As shown in Table 3.1, RS-AMVs were computed in seven channels: VIS with the highest spatial resolution of 0.5 km (B03), IR included in the short-wave infrared band (B07) and the infrared band (B13), WV in the water vapor absorption bands (B08, B09, and B10), and CO_2 in the CO_2 absorption band (B16). AMVs have been computed in almost the same bands as B03, B07, B08, and B13 since the MTSAT series, while B09, B10, and B16 are entirely new for AMV retrieval. WV AMVs were obtained only in cloudy conditions, so they were supposed to track cloud tops similarly to high-level IR winds (Velden et al. 1997).

CO_2 AMVs also track clouds since CO_2 is normally well mixed in the troposphere (Shimizu et al. 2017). Though the CO_2 band is often used in height assignment as auxiliary information, it seems convenient for tracking because land features are not so apparent at low levels in its imagery and tracking features are more recognizable at high levels than in those of WVs.

The RS-AMV datasets were compared with the JMA's Mesoscale Analysis (MA) and upper-air observational data for the month of June 2016. Figure 3.3 maps out the GPS radiosonde and wind profiler (WPR) stations in the JMA's upper-air observation network used for the comparisons. The distance between a pair of compared observations was within 150 km horizontally, 25 hPa vertically, and 1.5 hours in time for sonde observations following the recommendation of the Coordination Group for Meteorological Satellites (Schmetz et al. 1999). Moreover, WPR observations used for comparison were within 50 km, 10 hPa, and 10 min, respectively. The statistical analysis for the verification was separately made for each group of three different height classes: low (below the 700 hPa pressure level), middle (700–400 hPa), and high (above 400 hPa) levels.

b. Results of verification

First, RS-AMVs were compared with MA at the nearest grids. Table 3.2 shows the differences (RS-AMV minus MA) averaged over the entire month of June 2016. The root mean square vector differences (RMSVDs) in the VIS and IR (B03, B07, and B13) channels were around 3.4–4.6 m s^{-1} at low levels, 4.5–4.8 m s^{-1} at mid-levels, and 5.4–5.6 m s^{-1} at high levels. They were somewhat smaller compared to those in the WV channels (B08, B09, and B10) at mid- or high levels. The root mean square differences (RMSDs) for the u- and v-components and wind speed were also slightly larger in WV than in the VIS and IR channels, and slight positive biases were noticeable in the mean differences (MD) for wind speed in B08 and B09. B10

showed the smallest differences among the three WV channels. As for the CO_2 channel, its low-level winds had larger RMSVDs and RMSDs compared to VIS and IR, while its errors for mid- and high-level winds were comparable to VIS and IR and smaller than the WV channels.

The comparisons with sonde observations (Table 3.3) showed similar results, with slightly larger RMSVDs and RMSDs in the WV channels than in the VIS, IR, and CO_2 channels. In contrast to the results of the comparison with MA, MDs of the u-component and wind speed suggested that RS-AMVs in VIS and IR had significant negative biases above mid-level. High-level winds in CO_2 also showed a slight negative bias. Furthermore, in the WV channels, slight positive biases were seen at high levels in B08 and at mid-level in B09 and B10. Low-level winds in VIS and IR showed slight positive biases, which were not distinctly seen in comparison with MA.

With their higher spatial and temporal data resolutions than sonde observations, WPR observations could validate many more local winds at low level. Table 3.4 shows the differences of low-level RS-AMVs in the VIS, IR, and CO_2 channels from WPR observations. Overall, they appear consistent, except for a slight negative bias in the u-component and wind speed of B16. RMSVD, RMSDs, and MDs were smallest in the VIS channel, as expected, because it has the highest spatial and temporal resolutions of all of the channels. The positive wind speed biases that were seen in the comparison with low-level sonde winds in VIS and IR were not recognized in the comparison with WPR observations.

In summary, the quality of Himawari-8 RS-AMVs is sufficient for assimilation. The VIS and IR channels that were inherited from the MTSAT series proved to produce better RS-AMVs than the WV channels, including the two new channels (B09 and B10), in terms of consistency with MA, sonde, and WPR observations; however, negative biases against sonde observations above mid-level were

significant. In fact, this negative bias has been a well-known issue in AMV communities for many years (Schmetz et al. 1993; Velden and Bedka 2009); it has been considered because of either height assignment errors or target tracking errors, especially in and near jet streams, and was recognized in MTSAT-1 RS-AMV as well (see Chapter 2). Although Shimoji and Nonaka (2016) reported that the negative biases against sonde were somehow alleviated in Himawari-8 RTN-AMVs compared to MTSAT RTN-AMVs, the same trend was still found. The reason why they were not conspicuous in the comparison with the MA may be that RTN-AMVs were already assimilated during the construction of the MA. Velden and Bedka (2009) showed that errors associated with height assignment contributed an important part of AMV data uncertainties by comparing with collocated rawinsonde profiles. It was found that many AMVs in the location of jet streams were assigned to be higher than the level of best fit determined with the rawinsonde collocation. Similar issues of the height assignment uncertainties and the vertical representativeness were addressed in other studies as well using space-borne lidar observations (Weissmann et al. 2013; Folger and Weissmann 2014, 2016) or simulated AMVs (Hernandez-Carrascal and Bormann 2014; Lean et al. 2015). In contrast to IR channels, WV channels, B08 in particular, tended to show a positive bias above mid-level. Velden et al. (1997) reported that WV high-level winds were similar to those of IR but exhibited slightly lower heights because of the spectral response functions. This may partly explain the bias difference between IR and WV. Another new channel, CO_2, also seemed to produce winds of good quality comparable to those of VIS and IR, except at low level. Low-level winds in VIS and IR, including those over land areas, were in good agreement with WPR, so that they could possibly capture characteristic wind features near the surface that are useful for mesoscale prediction. It should be noted that low-level winds in B03 were of

better quality than other winds, probably because that channel has the highest resolution in both space and time.

We applied the same kind of statistical analysis to RTN-AMVs and found that the tendency and magnitude of the differences from MA and upper-air observations for each channel were similar to those of RS-AMVs regardless of their differences in temporal resolution (not shown). This result means that the characteristics of AMVs found in the data originated from the AHI specifications as well as from the new retrieval algorithm (Shimoji 2014). The advantages of using a 2.5-min rapid scan over the routine 10-min scan for AMV retrieval seemed to be in the increased number of data and higher density and frequency rather than the data quality.

3.2.2. Inter-channel observation error correlation

a. Data and method

We estimated the inter-channel correlation of observation errors of RS-AMV based on first-guess departure (RS-AMVs minus NHM first-guess winds) statistics using the so-called Hollingsworth–Lönnberg method (Bormann and Bauer 2010; Waller et al. 2016). This method is limited in its ability to estimate accurately observation error correlation between observations because first-guess departures may also be influenced by correlated first guesses between the two observations. However, it may serve our purpose in this paper for obtaining an overall view of the relationships of the error characteristics among the multichannel RS-AMVs. The first-guess samples were taken every 10 min from the 15-hour NHM forecasts, which were run every day at an initial time of 0000 UTC from 1 to 10 June 2016 with a horizontal resolution of 5 km (721 × 577 grid points) and 50 vertical levels. Among the 15-hour forecasts, those in the first six hours were discarded as spin up and not used for the computation. First-guess departures were obtained as RS-AMVs minus NHM forecast winds (first guess) at the time of RS-AMV observations every

10 min from the 6-hour Forecast Time (FT06) to FT15. Correlations of first-guess departures between pairs of observations within the same 3-hour window and within a distance of 50 km in the horizontal and 25 hPa in the vertical were calculated and averaged for the 10-day period.

b. Estimated observation error correlations

Table 3.5 shows the estimated inter-channel observation error correlations for the u- and v-components. It is generally considered that an error correlation between two adjacent observations greater than around 0.2 degrades the analysis and forecast (Liu and Rabier 2003). The values were around 0.20 to 0.35, indicating moderately high correlations between the channels. The two IR channels, B07 and B13, were most strongly related, with values of 0.35 for both u and v. The three WV channels also showed relatively high correlation with each other and were well correlated with B13, with values above 0.25. B16 showed the strongest correlation with B13 and rather high correlations with WVs and B07 as well. B03 showed the highest correlation value with B13 compared with the other channels. These relationships among the channels seem reasonable, assuming similar error characteristics for channels of the same category as we saw in the data verification results in Section 3.2.2. The differences or similarities of data distribution by layers (Fig. 3.2) between the channels could also be a factor to decide their relationships.

3.3. Assimilation experiments

The features of the RS-AMV observation errors were presented in the previous sections. For the next step, this section shows how their data characteristics are reflected in their assimilation behavior, which is one of our major interests in this paper.

3.3.1. The data assimilation system and experimental design

Assimilation experiments were conducted using the JNoVA data assimilation system (Honda et al. 2005). Because details of the system are described in JMA (2013), here we only explain the modifications that were made for the purpose of assimilating RS-AMVs in this study. First, 10-min RS-AMV observations were collected into 10-min time slots within a 3-hour time window instead of the ordinary interval of 1 hour used for the other observation data, including surface, upper air, radar, satellite, and ground-based Global Navigation Satellite System data. Thus, data for each slot were compared with the NHM first guess and quality controlled every 10 min in the case of RS-AMV. Second, RTN-AMVs around Japan were excluded when RS-AMVs were assimilated to avoid the redundancy that might be caused using two AMV datasets obtained from the same Himawari-8. It should be noted that the domain of excluded RTN-AMVs was almost the same as the MA area (Fig. 3.4a) and much broader than the rapid scan area in Fig. 3.1. Finally, the horizontal scale of RS-AMV thinning was reduced to 0.5° or 1.0° from the operational setting of 2.0° to exploit these high-density data. Two different thinning scales were used to examine the impact on the analysis and forecast by the length of data thinning. A thinning distance of 0.5° may be slightly too short, considering possible observation error correlations in space. However, its use can be justified because we intended to distinguish the expected impact using as many RS-AMV data as possible and to demonstrate their effects in a case study on mesoscale disturbance. The vertical thinning scale was 100 hPa, the same as that for RTN-AMVs. The data thinning was done once during a 3-hour window in the same way as RTN-AMVs to avoid observation error correlations in time-space. Through the thinning procedure, a representative RS-AMV vector was chosen from all of the RS-AMVs of all of the channels in a three-dimensional thinning box space of 0.5° × 0.5° × 100 hPa (1° × 1° × 100 hPa) collected in 10-min timeslots in a 3-h assimilation

window. It was determined based on combining three factors with weights, the time difference from the analysis time, distance from the center of the thinning box, and the value of the quality indicator flag (QI; Holmlund 1998). A vector that is closer to the analysis time and the box center and has a higher QI value was prioritized. In this way, we could usually avoid inter-channel observation error correlations. The possible nearest distance between adjacent observations was approximately 50 (100) km and 100 hPa in space and 10 min in time.

RS-AMVs were selected based on QI, which was attached to individual data in the first phase of quality control, before going through the thinning process and other quality checks such as gross errors. The QI value is based on consistency checks with the first guess field of a global spectral model, neighboring wind vectors, and previous observations. A higher QI value means better data quality. The QI thresholds used in the experiments were determined depending on the channel categories and height classes, taking into account the results of data verification (Table 3.6). The observation errors were the same as those used operationally during the time of the MTSAT series (Table 3.7). The magnitudes of the observation errors were determined according to pressure height levels, regardless of the differences among channels.

Table 3.8 summarizes the designs of the test experiments. In a test experiment for a certain channel, RS-AMVs derived only from that channel were assimilated to examine their impact independently, while those of all seven channels were used in ALL. In ALL, two experiments with different thinning scales, namely, ALL with 0.5° and ALL1.0 with 1.0° thinning scale, were performed. The forecast results of each test were compared with a control experiment (CNTL), in which no RS-AMVs and only RTN-AMVs were assimilated. As for CNTL, an additional experiment with 0.5° thinning, CNTL0.5, was also conducted in order to compare the RTN-AMV dataset with the RS-AMVs in the same thinning scale. In B03, only low-level winds

were assimilated to examine the impact of the local scale winds with higher resolution than other data. Low-level winds of B16 were not used because they were few in number and of worse quality than those of VIS and IR, as seen in Section 3.2.1.

The domains of assimilation and forecasts are shown in Fig. 3.4. The assimilation experiments described in Table 3.8 were conducted during 12 hours in the daytime when VIS AMVs were available (2100 UTC 19 to 0900 UTC 20 June 2016), i.e., four forecast-analysis cycles of JNoVA, during which a cold vortex, described in the next section, passed over the northern Tohoku region from the Japan Sea to the Pacific side of Japan. In each experiment, the analysis results at 0900 UTC 20 were used as the initial conditions, and a 24-h forecast was obtained.

3.3.2. The selected event

Assimilation experiments with RS-AMVs were performed for a cold vortex event that occurred on 20 June 2016. On that day and the next, a Baiu stationary front extended across from China to the southern coast of the main island of Honshu (Figs. 3.5a, b, c), and a low appeared in the Japan Sea off the coast of northern Japan, Hokkaido and Tohoku. At 500 hPa, there was an upper level low over the Japan Sea accompanied with a cold vortex of −15°C (Fig. 3.5d) that moved eastward during the day, passed across the northern part of Tohoku and out on to the Pacific at night (Figs. 3.5e, f).

Figures 3.6a, b, c, and d show the distributions of the Himawari-8 AMVs that were assimilated in the experiments of CNTL, ALL, CNTL0.5, and ALL1.0 during the fourth cycle, 0600－0900 UTC 20 June. RS-AMVs in ALL (Fig. 3.6b) distinctly represent the wind field near the cold vortex over northern Japan with much denser data than RTN-AMVs in CNTL (Fig. 3.6a), which also indicated the location of the vortex but less clearly with many fewer data. CNTL0.5 (Fig. 3.6c) assimilated a

larger amount of RTN-AMVs than CNTL but still failed to capture wind vectors near the vortex in detail compared to ALL or ALL1.0 (Fig. 3.6d). It seemed that RS-AMVs had the advantage of detecting mesoscale flow fields near the vortex with higher temporal resolution than RTN-AMVs. Figures 3.6e and f show the first-guess departures of wind vectors in the ALL experiment during the same period. The low-level winds around the low over the Japan Sea seemed to have changed to strengthen cyclonic flow, and the weakening of westward winds was significant above 400 hPa. Hereafter, we focus on the changes that occurred only in the vicinity of the cold vortex in northern Japan because our strongest interest was in those local winds near the vortex that were expressed well with RS-AMVs but not with RTN-AMVs.

3.3.3. Results of assimilation experiments

a. Analysis

The differences in the analyses at the end of the four cycles at 0900 UTC on 20 June 2016 between ALL and CNTL experiments are shown in Fig. 3.7. The cold vortex was over northern Tohoku at that time and moving eastward. Differences in the wind vector and wind speed fields at 500 and 300 hPa (Figs. 3.7a, b) corresponded well with the wind field of the first-guess departures in the last assimilation circle (Figs. 3.6e, f) described in the previous section. Westward winds near the cold vortex were weaker at 300 hPa in ALL, which might affect the eastward-moving speed of the cold vortex. In ALL, geopotential heights of 500 hPa were higher to the north of the vortex and lower to its south (Fig. 3.7c), and temperatures at 500 hPa were slightly lower around the cold vortex than in CNTL (Fig. 3.7d)

b. Forecast

Next, the forecasts in ALL and CNTL were compared at 1200 UTC on 20 June (FT03). The maps in Figs. 3.5b and e show that the center of the cold vortex was off the Pacific coast of northern Tohoku, a low at 500 hPa was over the strait between Tohoku and Hokkaido, and surface lows appeared on both the Japan Sea and Pacific sides of the upper low. The ALL experiment simulated the positions and scales of the cold core and upper low (Fig. 3.8a) nearly as well as CNTL (not shown). Although the temperatures at 500 hPa did not show significant differences around the vortex (Fig. 3.8c), geopotential heights at 500 hPa (Fig. 3.8b) and surface pressures (Fig. 3.8d) in ALL were lower than those in CNTL in that area. These changes seem to agree with the changes in wind field analyses where cyclonic flows at low or mid-levels were enhanced by RS-AMVs. It is probable that assimilation of RS-AMVs caused the slight change in the intensity of the vortex.

The mesoscale cold vortex had weakened and lost its circular structure as it moved to the northeast over the Pacific in later hours. By 0000 UTC on 21 June (FT15), circulation of the cold vortex was no longer identifiable, the intensity of the low had weakened (Fig. 3.8e), and two small cold-core lows appeared side by side in the area between Hokkaido and Tohoku (Fig. 3.5f). The geopotential heights of 500 hPa near the lows were lower in ALL than in CNTL (Fig. 3.8f), indicating their slight intensification.

The forecast winds and temperatures at FT03 and FT15 were validated using sonde data at the observational sites over northern Japan (Fig. 3.9). At FT03, the RMSVDs were smaller overall in ALL than CNTL from 850 to 300 hPa levels, except at around 600 hPa (Fig. 3.9a), indicating a positive impact on the wind fields near the cold vortex. Furthermore, the temperature errors improved slightly at mid- to high levels (300–600 hPa) but degraded at the lowest and uppermost levels (below 800 hPa and above 250 hPa; Fig. 3.9b). The RMSVDs at FT15 showed better

agreement in ALL than CNTL from 700 to 300 hPa (Fig. 3.9c). The temperatures at 500 and 600 hPa were worse than CNTL, but the improvement was seen at some levels, especially above 400 hPa (Fig. 3.9d).

As described in Section 3.3.2, two additional experiments, CNTL0.5 and ALL1.0 besides CNTL and ALL in which the scales of data thinning were changed, were also conducted. CNTL0.5 exhibited similar results to CNTL besides the winds at FT15. It also outperformed ALL at low levels at that time, the reason for which we do not look into further here. It might be because its dense coverage in a much broader area than ALL had some advantages in later hour forecasts. As for ALL1.0, the results showed no or little improvement compared to ALL, except for the temperatures at FT03. More RS-AMVs with a shorter length thinning scale might cause a more positive impact; however, we do not further discuss the reason for it. We can deduce that we could safely use the thinning scale of 0.5° in assimilating RS-AMVs for the purpose of this paper without fear of degradation originated from observation error correlations among neighboring observations. Hereinafter, we refer to the ALL experiment with the data-thinning scale of 0.5° only. In the comparison with ALL, CNTL with the operational thinning scale of 2.0° was used because our main purpose was to distinguish the impact of RS-AMV and investigate their characteristics in the current operational system.

3.3.4. Impact by channel

The analyses and forecasts for the seven experiments where the RS-AMVs of each individual channel were assimilated were examined in the same way as ALL in the previous section. Because the RS-AMVs of the seven channels were assimilated in ALL, the contribution from each channel mixed with the others, so it was not easy to track it to its source. As we saw in Section 3.2.1, the different characteristics of winds in different channels might affect the results of the

assimilation in ALL differently. We compared the assimilation results of individual channel experiments to those of ALL.

Figure 3.10 shows the analysis and forecast differences of 500 hPa geopotential heights in each experiment at FT00 (Figs. 3.10b–h), FT03 (Figs. 3.10j–p), and FT15 (Figs. 3.10r–x). We can tell whether analyses and forecasts obtained in each experiment contradicted those in ALL (Figs. 3.10a, i, q) by the appearance of the color patterns in the figures. At FT00 and FT03, the analysis and forecast differences from CNTL around northern Japan in ALL corresponded well overall to those in the seven experiments, with the exceptions of B03 and B08. It may be reasonable that B03 or B08 showed patterns dissimilar to ALL and the others because their RS-AMVs covered only low or high levels. IR (B07 and, in particular, B13) was in fairly good agreement with ALL, as expected. This agreement is probably because a sufficient number of RS-AMVs were assimilated to cover all of the layers from lower to upper. B10 and B16 also had results similar to ALL, with a good amount of wind at mid- and high levels, although the negative region over the central part of Honshu was shifted eastward in both B10 and B16 at FT00. B09 showed a few contradictions, but still, some similarities were found. The negative region in B09 seemed smaller compared to the negative regions in other experiments at FT00 and FT03, except for B03 and B08. At FT15, when the differences from CNTL became much smaller than those in previous hours as the cold vortex disappeared, only IR showed results similar to ALL. The three WV channels (B08, B09, and B10) and B16 sometimes showed more similarity to each other than to ALL or IR. In addition to the differences of layers covered by the data, the channel categories might have such different patterns because of their different data characteristics.

The differences of RMSVDs against sonde winds from those of CNTL (RMSVDs with RS-AMV minus RMSVDs without RS-AMV) for each experiment at FT03 and FT15 are shown in Fig. 3.11. Negative (positive) values mean

improvement (degradation) compared with CNTL. At FT03 (Figs. 3.11a−d), B03, B13, and B10 slightly improved at low levels below 700 hPa. B07, B08, B09, and B16 showed no or little improvement at low levels but improved at 500–400 hPa. B13, B09, B10, and B16 showed slight improvements at 300–200 hPa. Because ALL improved below 700 hPa and at 500–300 hPa as mentioned in the previous section, the results of individual channel experiments partly contradicted and were partly consistent with ALL. B13 showed the most similarity to ALL in the RMSVD profiles. At FT15 (Figs. 3.11e−h), VIS, IR, B10, and CO_2 improved from CNTL around 700 hPa, but B08 and B09 showed no or little improvement at that level. Moreover, WV (B08, B09, and B10) showed some improvements at 400–200 hPa, whereas the other channels showed overall degradation.

3.3.5. Validation of forecast winds against wind profiler observations

Wind profiler observations enabled more frequent and closer comparison for low- to mid-level winds than sonde observations. The forecast winds below the 400 hPa level were compared with WPR winds in northern Japan at each forecast hour up to 24 hours. The RMSVDs for ALL and CNTL experiments showed little difference (Fig. 3.12a); however, the values were slightly smaller in ALL in the early hours before FT12. This result seems to be consistent with the fact that the winds below 700 hPa and at 500–300 hPa in ALL at FT03 were in better agreement with sonde winds than CNTL, as we saw in Section 3.3.3. The same statistical analysis was also applied to the other seven experiments (B03–B16), in which the RS-AMVs of an individual channel were assimilated. A tendency to show a slight improvement from CNTL in the earlier hours and no or little improvement in the later hours was commonly found among all the channels, with the exception of B03 (not shown in the figures).

Figure 3.12b shows the profiles of RMSVDs averaged over the entire forecast period of 24 hours. In ALL, RMSVDs were somewhat smaller in nearly all of the layers, especially at 900 to 800 hPa, indicating a slight improvement from CNTL. The RMSVD profiles for individual channel experiments are shown in Fig. 3.13 as the differences from CNTL. They were nearly the same pattern as CNTL, although slight differences were seen in wind height levels where improvement or degradation occurred according to the channels. B03 also showed a slight improvement at 900 to 800 hPa (Fig. 3.13a), and in addition, B13 excelled at that level and also at 600 to 400 hPa (Fig. 3.13b). B07 improved above 700 hPa at mid-levels (Fig. 3.13b). Overall, WV channels and B16 showed degradation below 700 hPa without any low RS-AMVs assimilated, but slight improvements were seen at some levels in mid-layers (Figs. 3.13c, d). When averaged over entire layers, RMSVDs were smallest in ALL compared with the other experiments. These results of the comparisons with WPR are roughly consistent with those with sonde data, as described in the previous section.

3.4. Discussion

The results of both the data verification and assimilation experiments suggest some ideas for building a future strategy for dealing with such high-density data as Himawari-8 RS-AMVs in a mesoscale data assimilation system. The process of data selection should be refined to pick up the most beneficial information from an enormous amount of data without causing possible degradation of the analysis due to observation error correlations. As the number of channels available for AMV retrieval has increased from four to seven by the change from MTSAT to Himawari-8, it is necessary to optimize the use of data from all of these channels. We found that channels of the same category shared similar error characteristics, which, as a consequence, could have similar impacts on the assimilation experiments. For

example, in Section 3.2.1, negative biases were observed in upper air in IR channels, while in some WV channels, positive biases were seen at the same levels. When these negative IR winds and positive WV winds are assimilated together, their effects might be somehow mixed and produce an unexpected impact. It can be said that the ALL experiment in Sections 3.3.3 to 3.3.5 provided fairly reasonable assimilation results, with overall consistency with the individual channel experiments despite a few exceptions. We need to develop a method to prioritize data of better quality to make better use of multi-channel RS-AMVs.

In the experiments described in this paper, the data selection relied on QI number thresholds and other basic QCs such as gross error checks that are embedded in the pre-processing procedures of JNoVA. Because QI can sometimes assign a low number to a mesoscale AMV (Bedka and Mecikalski 2005), we may need to lower the thresholds or disable the forecast check test and develop an additional quality check tailored to high-resolution RS-AMVs. Concerning the negative wind speed biases in upper layers that are also recognized in RTN-AMVs, Yamashita (2016) introduced a new QC procedure in the JMA global NWP system to reject u-components with negative bias around jet streams. Shimoji and Nonaka (2016) reported that estimated heights of Himawari-8 showed some improvement in accuracy compared to those of MTSAT-2 in terms of collocation with backscatter plots of Cloud-Aerosol Lidar and Infrared Pathfinder Satellite Observations (CALIPSO), which is probably due to the new height assignment method (Shimoji 2014) with more variety of channels. However, the available samples for collocation were limited, and the accuracy of the CALIPSO product as a reference was not exactly known. Future work should include estimation of height assignment uncertainties and representative errors of Himawari-8 AMVs based on best-fit statistics (Salonen et al. 2015). It is necessary to consider these error characteristics

in QC or other pre-processing procedures to better utilize RS-AMVs in data assimilation.

The data-thinning procedure is another important issue in dealing with high-density RS-AMVs. Judging from the results of the assimilation and their comparison with CNTL, data thinning on a scale of 50 km once within a 3-hour time window for RS-AMVs for all of the channels seems to have been adequate for the purpose of this study. It is necessary to find an optimal scale and time interval for data thinning by trying other cases in different settings. A super observation approach is another option if the data representative scale can be properly taken (Wu et al.2014; Yamashita 2016; Kunii et al. 2016). In dealing with multiple channels, it may be worthwhile to try to assimilate RS-AMVs for each channel separately as different kinds of observation. In this study, RS-AMVs of all channels were formed into one box observation through the data thinning process to avoid possible inter-channel correlations.

3.5. Conclusion

Himawari-8 RS-AMVs obtained in June 2016 were more than 20 times the number of RTN-AMVs obtained in the same month, and they had much higher density and frequency. Their data quality proved to be sufficiently good for assimilation when compared with MA and upper-air observations. Different error characteristics were observed in different channels, which can be classified by the categories VIS, IR, WV, and CO_2. The channels in the same categories showed characteristics similar to each other in terms of data quality. Among the categories, VIS and IR showed a relatively high degree of similarity, and CO_2 fell in between these two and WV. Such tendencies in the relationships between channels and categories were also recognized in the estimated inter-channel observation error correlations.

Assimilation experiments for a cold vortex event on 20 Jun 2016 were conducted with JNoVA using RS-AMVs from the seven channels. Although the differences in analysis and forecast results between the experiments with and without RS-AMVs were subtle, some interesting changes were found. First, RS-AMVs seemed to slightly intensify the upper low at 500 hPa. Second, the verifications against sonde and WPR observations indicated small improvements in low- to mid-level winds over northern Japan in the vicinity of the cold vortex, especially in the early forecast hours before FT12. In addition, the results from the experiments that used each individual channel might reflect similarities in the error characteristics among channels. The experiment in which all seven channels were assimilated performed better than the individual channel experiments in terms of the agreement of wind forecasts with upper-air observations. The better coverage of RS-AMVs from low to high levels may be the reason for the better forecast results. Although the spatial and temporal resolutions of the RS-AMV data set were improved over that of RTN-AMVs, the domain of rapid scan observations was limited, which might be a reason for the subtle impact of RS-AMVs, particularly in later hours.

To exploit these high-density and high-frequency data, we need to further investigate optimal methods for data selection and QCs before assimilation, based on what we found in this work.

Chapter 4

Data validation and mesoscale assimilation of Himawari-8 optimal cloud analysis products

4.1. Introduction

Geostationary satellites (GEO) together with low-Earth orbit satellites (LEO) are major components of the spaced-based Global Observing System (WMO 2010). Data obtained from visible (VIS) and infrared (IR) imagers and additional sensors onboard satellites have been an important source of the information assimilated by numerical weather prediction (NWP) systems for a number of years. The emergence of so-called new-generation GEOs, starting with Himawari-8, which launched in 2014, has added even more significance to their roles, because these new satellites provide unprecedented amounts of data obtained by advanced sensors and high-frequency observations (Coordination Group for Meteorological Satellites 2020). Atmospheric motion vectors (AMVs) and clear sky radiances (CSRs) are two of the primary GEO products currently used for assimilation in major operational NWP centres, including the Japan Meteorological Agency (JMA). No centres yet use direct assimilation of cloud-affected IR radiances operationally, though the assimilation of high-frequency GEO radiances has the potential to benefit short-range forecasts (Geer et al. 2018), as has been demonstrated recently in mesoscale systems utilizing Himawari-8 data (Honda et al. 2018b; Minamide and Zhang 2018; Okamoto et al. 2019). Although the direct assimilation of VIS reflectances operationally seems to take extra time, fast radiative transfer models are under development. Scheck et al. (2018) pointed out that the ability of VIS channels to detect low clouds with a high resolution is beneficial to convective scale assimilation.

Besides the direct assimilation of radiances, another approach is to assimilate retrieved products such as cloud properties and wind vectors. Retrievals have the advantage of requiring fewer resources during the assimilation process without any need for complicated radiative transfer models, and they are often the same meteorological variables as those used in the model (Migliorini 2012; Jones et al. 2013). The disadvantage of retrievals is that uncertainties and untraceable errors are added during the retrieval process (Swinbank 2010).

Cloud properties retrieved from satellites such as cloud optical thickness (COT), cloud top pressure (CTP), and cloud fraction (CF) that have been assimilated into mesoscale systems, mostly by adjusting humidity fields (e.g., Macpherson et al. 1996; Lipton and Modica 1999; Fan and Tilley 2005; Storto and Tveter 2009; Renshaw and Francis 2011), have improved analysis and forecast fields, especially for precipitation and cloudy conditions. It might be better, however, to initialize hydrometeor variables individually for the purpose of mesoscale short-range forecasting, although in a four-dimensional variational (4D-Var) assimilation system, the hydrometeor fields can be determined from the initial dynamical and humidity fields (Geer et al. 2018). Jones et al. (2013) developed a forward operator to assimilate cloud water path (CWP) data derived from GOES observations that was able to reproduce convection associated with a severe weather event well.

Optimal cloud analysis (OCA) is an optimal estimation method for extracting cloud parameters such as phase, CTP, COT, cloud effective radius (CRE), and CWP from satellite data; it was originally developed by the European Organization for the Exploitation of Meteorological Satellites, EUMETSAT (2016a). Poulsen et al. (2012) described the algorithm of optimal estimation and its technical details of cloud property retrieval. Hayashi and Watts (2016) adapted the 2-layer retrieval method of Watts et al. (2011) and developed an OCA scheme that employs all 16 spectral imaging channels of the Advanced Himawari Imager (AHI). Validation

against retrievals from the Moderate Resolution Imaging Spectroradiometer (MODIS) and cloud top heights (CTH) and cloud detection by the CloudSat and the Cloud-Aerosol Lidar and Infrared Pathfinder Satellite Observation (CALIPSO) satellites for samples collected in a few days showed Himawari-8 OCA retrievals to be of sufficiently good quality. They provide useful information on water vapor in clouds with good horizontal resolution (about 0.02°) and coverage, including over the ocean. Given that most heavy rainfall events in Japan are caused by low-level inflows from over the ocean (Kato 2018), it is clear that water vapor information from over the surrounding sea areas, which cannot be obtained except by satellites, is useful to produce better initial conditions for mesoscale assimilation.

Compared with the previous MTSAT series, Himawari-8 has more channels and enhanced resolutions, of 0.5 to 1 km for VIS and near-IR channels and of 2 km for IR channels, and it performs observations with higher frequency (Bessho et al. 2016). It thus benefits the operational JMA mesoscale NWP system by providing more, higher quality AMV and CSR data for assimilation (Yamashita 2016; Kazumori 2018). Case studies in which AMVs assimilated with much higher resolution obtained from 2.5-min sector rapid scans (Kunii et al. 2016; Otsuka et al. 2018) have demonstrated the potential of these new data, which are yet to be fully employed operationally. The results of direct assimilation of all-sky radiances of water vapor channels for a heavy rainfall event (Honda et al. 2018a) and a local convective storm (Sawada et al. 2019) suggest such assimilation has a positive impact on both the analysis and forecast fields. The most important advantage of assimilating OCA cloud properties, compared with the assimilation methods used by these previous studies, is that, by using the products derived from all 16 channels, OCA can extract more information from Himawari-8 observations. For example, VIS, near IR, and IR window channels are sensitive to COT, CRE, and CTP,

respectively. Direct assimilation of these Himawari-8 channels, however, has not yet been investigated.

In this study, our aim was first to clarify OCA data characteristics and representativeness by validating OCA data against surface and upper-air observations. Then we examined the data from the point of view of exploiting them for mesoscale data assimilation by comparing them with mesoscale model CWP and CTP outputs. On the basis of these verification results, we decided to assimilate OCA products as relative humidity (RH) data using JMA's Non-Hydrostatic model-based variational data assimilation system (JNoVA; Honda et al. 2005). Finally, we conducted assimilation experiments for a few heavy rainfall events to examine the impact of the OCA data assimilation on short-range precipitation forecasts. The rest of the chapter is structured as follows: Section 4.2 describes the verifications conducted against observations and model outputs. Section 4.3 explains the method used to construct the pseudo-RH data set and the experimental settings, and it presents the results of the assimilation experiments for heavy rainfall events. We further discuss the verification and assimilation results in Section 4.4, and we present our conclusions in Section 4.5.

4.2. OCA data characteristics

Himawari-8 OCA data were produced from 10-min full-disk scans of the domain within 20°−50° N and 120°−150° E with a horizontal resolution of 0.02 degrees of latitude and longitude. They were compared with different types of observations as well as with outputs of JMA-NHM. The data range and other features are different between daytime and nighttime because VIS channels are available only in the daytime; thus, only daytime data were used for this study. Each OCA product has an error estimate, and each pixel is accompanied by the final fit to the measurement, that is, the solution cost (EUMETSAT 2016b). We did not directly

use such error information attached to retrievals in order to fully examine this newly developed Himawari-8 OCA without reducing the amount of available data.

A cloud mask scheme (Ishida et al. 2018) was used in deciding which pixels to process for OCA retrievals. The OCA scheme was run in a single cloud mode or quasi 2-layer mode as described in Hayashi and Watts (2016) using the Radiative Transfer for TOVS (RTTOV) version 11 (Saunders et al. 2018), because our assimilation targets were eventually low to middle water clouds, which might be retrieved more accurately with a single cloud mode due to the restrictions to IR channels in the 2-layer mode (Watts et al. 2011). Hayashi and Watts (2016) have shown that Himawari-8 OCA COT and CRE retrievals are consistent with those derived from MODIS (correlation coefficient, 0.91 and 0.84, respectively). OCA CTHs were compared with the CloudSat cloud profiling radar (CPR) and showed good agreement (correlation coefficient, 0.85). The CTHs were also compared with 523 nm total backscatter of the Cloud−Aerosol Lidar with Orthogonal Polarization (CALIOP) onboard CALIPSO for a snapshot. While these validation with more advanced imagers and active sensors on board LEOs are useful, the observation repeat time of A-train data (NASA 2003) is not enough for evaluating high-frequency observations utilized in mesoscale assimilation. In addition, even active sensors may have difficulty in accurately detecting clouds where precipitation occurs (Mitrescuet al. 2010).

To begin with, the accuracy and representativeness of Himawari-8 OCA need to be better understood, because these cloud properties have not been utilized previously in our data assimilation system. Nor have they been used for weather monitoring or other operational uses. Therefore, in Sections 4.2.1 and 4.2.2, we first verify the data against conventional data sets to determine how well OCA data generally reflect meteorological conditions. To obtain pseudo-RH profiles for assimilation, we estimated cloud base heights (CBHs) from OCA products using

methods similar to those used for the product derived from the Visible Infrared Imaging Radiometer Suite onboard the Suomi National Polar Orbiting Partnership satellite (Seaman et al. 2017) as described in the Section 4.3.1. We examined how OCA data characteristics differ depending on cloud structure, in particular, the relationships between CTP, COT, and cloud classification, which was helpful to estimate CBH. Comparisons with human observations made at JMA surface stations gave us useful information in that regard.

4.2.1. Cloud fraction, cloud type, and cloud occurrence in comparison with surface observations

Within the OCA data coverage area for July 2017, there are 59 surface stations, where cloud types, amounts, and heights, as well as present weather, are routinely observed by humans every 3−6 h for surface synoptic reports (SYNOP). First, the CF in the OCA data at each station was estimated and compared with SYNOP data from the same hour. OCA data points within a 5-km radius from a station were counted to compute cloud fraction. The ratio of the number of cloudy points to the maximum possible number of OCA data grids within that radius was defined as the CF at the station. The CFs determined by SYNOP and by OCA, described in tenths from 0 to 10, during daytime hours in July 2017, were compared. A total of 5,253 cases were available for this comparison. These sample cases were also used for other statistics, as described later in this subsection.

The CFs based on OCA and SYNOP observations were well correlated (correlation coefficient, 0.70). The mean CFs during the comparison period were 7.3 and 7.8 for OCA and SYNOP, respectively. Because SYNOP observers determine CF for the whole sky, the SYNOP value can include upper- and mid-level clouds at distances of more than 5 km from the station. The SYNOP value was, therefore, usually larger, except when cloud heights were much less than the cloud widths

(Bretherton et al. 1995). Thus, the correlation results suggest that OCA data within a radius of 5 km adequately represent cloud conditions in the vicinity of a station. Hereafter, we use OCA COT, CTP, CRE, and CWP data averaged over the area within a radius of 5 km from a station in our comparisons with SYNOP and upper-air sonde observations.

Next, we examined the dependence of OCA data characteristics on weather conditions by dividing the 5,253 cases into three categories of conditions: fair, cloudy, or rainy. SYNOP present weather (PW) codes (WMO 2011) for fair and cloudy conditions that range from 00 to 49, and they signify that no precipitation was occurring at the station at the observation time. Fair and cloudy SYNOP categories are separated by a CF threshold value of 5; cases with CFs less than or equal to 5 were considered fair, and those with CFs greater than 5 were considered cloudy. Cases with PW codes greater than 49 and CF greater than 5 were designated as rainy. Only one case, with a PW of 80 and CF of 4, was not included in any of the three categories. Frequencies of OCA COT, CTP, CRE, and CWP values in each of the three weather categories are shown in Fig. 4.1. The COT and CWP histograms were similar; most fair cases were in the smallest bin, rainy cases were scattered among the high-frequency bins, and cloudy cases were intermediate in frequency. The most frequent CTP values were around 950−1000 hPa in fair and 250−300 hPa in cloudy and rainy cases. In fair cases, CRE values were mostly below 30 μm, whereas CRE values in cloudy and rainy cases spread over a relatively wide range. These differences among the weather categories could be explained by the types of clouds that were prominent under these different weather conditions.

Table 4.1 summarizes the average COT values, SYNOP cloud types, and their corresponding cloud types in the International Satellite Cloud Climatology Project (ISCCP) classification method (Rossow and Schiffer 1991) in each of the three weather categories and in each of the three OCA CTP layers: high (above 440 hPa),

middle (680 to 440 hPa), and low (below 680 hPa). SYNOP cloud types are listed in the order of their appearance frequency in the table. ISCCP cloud types were determined by applying the averaged OCA CTP and COT values as parameters to the ISCCP cloud classification chart of nine cloud types. This chart is commonly used to estimate cloud vertical structure from CTP and COT values obtained from VIS and IR radiances (Young et al. 2013). We used the classification as an indicator to verify the consistency of OCA CTP, COT, and SYNOP PW and cloud types.

In fair cases, low cumulus (Cu) clouds were most likely to be seen, often accompanied by upper- and middle-level clouds such as cirrus (Ci) and altocumulus (Ac). Though not many, there were some fair cases with high- or mid-level CTP values and Ci and Ac as the primary clouds in SYNOP. COT at around 2.0 was much smaller than that in the other categories, an indication that the clouds were not as developed vertically. The COT was greater in cloudy cases than in fair cases because of the fact that cirrostratus (Cs) and altostratus (As) were observed as well as Ci and Ac by SYNOP. In most rainy cases and in many cloudy cases, mid- to high-level cloud types were labeled "N/A" (not available) in SYNOP, because low clouds occupied almost the whole sky and obstructed the view of the observers. COT values in rainy cases were larger than those in fair and cloudy cases, apparently because of the formation and development of multilayered clouds and deep convection, which were suggested by the coincident SYNOP cloud types. OCA CTP tended to be high and seemed to capture only the uppermost cloud layer in such cases. The relationships among OCA CTP, COT, and SYNOP PW and cloud types agreed overall with the ISCCP classification. Thus, in general, OCA represented surrounding meteorological conditions properly.

When OCA cloud occurrences were validated against surface observations (Table 4.2), the accuracy rate was around 60 % for high-level clouds and 50 % for mid- to low-level clouds. The number of misses (false negatives) was larger for

lower-level clouds than for mid- to high-level clouds. This result can be explained by the fact that a passive IR and VIS imager cannot see through to the lower-level clouds when upper-level clouds cover the sky.

4.2.2. Cloud top pressure and cloud occurrence in comparison with upper-air observations

In one commonly used way of determining cloud locations from temperature and RH profiles of sonde observations, a cloud layer is detected where RH is above a threshold value (e.g., Wang and Rossow 1995). Costa-Surós et al. (2014) have comprehensively reviewed several different methods of obtaining cloud vertical structures from such profiles. We used different RH threshold values depending on height, as described in Zhang et al. (2010), and inferred cloud layers from upper-air sonde observations conducted at 17 JMA stations at 0000 UTC every day in July 2017. Observed RH at temperatures below 0 °C was converted to RH with respect to ice instead of liquid water for the comparison with the threshold values.

First, OCA CTPs within a radius of 5 km from upper-air sonde stations were compared with the CTPs derived from the sonde profiles obtained at the stations. If one or more cloud layers were detected in a sonde profile, each layer was compared with the OCA CTP at the level closest to them. When no clouds were detected either by sonde or OCA, the comparison was not made. Figure 4.2 shows some examples of the relationships among RH and temperature profiles, cloud layers identified by sonde observation, and OCA CTPs in the vicinity of a station. In some cases, OCA failed to detect sonde-observed cloud layers or falsely detected them at much lower or higher positions. Figure 4.2c illustrates a typical rainy situation where OCA clouds are present only around the top of the deep cloud layer, regardless of the existence of multilayers in the sonde profile. Figure 4.3 shows histograms of the differences in CTP and CTH between OCA and sonde observations at all stations

during July 2017. The mean error was -7.0 hPa (180 m) for clouds at all levels. Therefore, OCA CTPs and sonde observations were in good agreement overall.

Second, cloud occurrence matches were evaluated in the same way as described in Section 4.2.1. For this comparison, 533 sample pairs were used, and the results are summarized in Table 4.3. OCA matched well with sonde observations at mid- to high levels with an accuracy rate of around 75 %; at low levels, the accuracy rate was 48 %. In contrast to the results of the surface observation comparisons, there was a notable number of misses at high levels. Considering the horizontal distance traveled by a sonde as it ascends, the 5 km radius might be too small for collocation, especially for upper-air observations. In addition, sondes sometimes ascend through cloud breaks or patchy clouds and fail to detect cloud layers (Naud et al. 2003), a circumstance that may partly explain why the frequency of false cases was significant at low levels; these cases were probably related to cloud layers consisting of scattered, small, low-level cumulus clouds.

The results of the OCA validation against conventional data sets showed that OCA cloud products were of sufficiently good quality to represent cloud conditions at synoptic scale to mesoscale. However, especially in the case of vertically developed precipitable clouds, OCA may have difficulty obtaining information from below the top of the uppermost clouds.

4.2.3. Cloud top pressure and cloud water path in comparison with model

We next investigated the OCA data characteristics in comparison with model outputs to get prior information before eventually utilizing them for mesoscale data assimilation. JMA-NHM with 60 levels in the vertical and a horizontal resolution of 2 km was run using JMA's mesoscale analysis as initial and boundary conditions. The runs were started at 1800 UTC every day from 6 to 9 September 2015 to obtain 15-h forecasts. First-guess departure statistics (observation minus model first guess)

were obtained from hourly forecast data during 0000−0900 UTC 7−10 September and OCA data at the same hour. Model cloud layers corresponding CTP and CWP were determined by the method of Jones and Stensrud (2015). For each grid point and model level, the mixing ratios of hydrometeor variables, including cloud water, cloud ice, graupel, rain, and snow, were summed to obtain the total cloud mixing ratio. A model cloud layer is resolved where the total cloud mixing ratio exceeds 0.01 g kg^{-1}. The levels for the top of the uppermost cloud layer and the bottom of the lowest cloud layer are defined as the model CTP and cloud base pressure (CBP). The total mixing ratio Q_k of the layer at the P_k pressure level is integrated from CBP(P_0) to CTP(P_n) and divided by gravity g to obtain model CWP:

$$CWP_{model} = \sum_{k=1}^{n} \frac{Q_k(P_k - P_{k-1})}{\mathrm{g}} \tag{4.1}$$

OCA does not retrieve CWP directly because it is difficult to estimate the vertical distribution of cloud properties such as cloud water. Instead, OCA CWP is derived from COT τ and CRE r_e as follows:

$$CWP_{oca} = \frac{2}{3}\rho\tau r_e \tag{4.2}$$

where ρ is the density of liquid water or ice (Stephens 1978). OCA classifies cloud-flagged pixels into three different phase categories, water, ice, and multilayer. Because OCA data in a single cloud layer mode were used in this study, each OCA pixel was classified as water or ice. When multiple cloud layers are present, OCA CWP is likely to include both the liquid water path (LWP) and the ice water path (IWP), regardless of the flagged cloud phase. The accuracy of CWP is greatly affected by retrieval uncertainty of COT, which generally increases as the COT increases (Nakajima and King 1990), due to saturation of VIS channel signal in thick

clouds (EUMETSAT 2016b). We used OCA CWPs having COT values equal to 100 or below for the validation.

OCA data were compared with JMA-NHM outputs at the nearest grid during the period. Because OCA and NHM did not necessarily resolve clouds in the same locations at the same time, roughly one-third of the collocated model grids had cloud layers where samples for first-guess departure statistics were available.

Figure 4.4 shows frequency histograms of CWP and CTP differences between OCA and NHM (OCA minus NHM) during the whole period. The histograms for CWPs look slightly left-skewed, especially in the case of ice clouds (Fig. 4.4a). The mean error was -198.0 g m^{-2} and -460.3 g m^{-2} for water and ice clouds, respectively. The large discrepancy between OCA and NHM CWPs seemed to be associated with precipitation clouds, that is, when fairly a large amount of rain, snow, and graupel was present in the NHM grid and resulted in a much larger CWP than OCA CWP.

The mean error and the root mean square error (RMSE) of OCA CTPs relative to NHM CTPs at all levels were 25.3 hPa and 213.7 hPa, respectively; thus, OCA CTPs showed a slight positive bias but with a peak at around 0 (Fig. 4.4b). When OCA CTPs were divided into the three height categories (Fig. 4.4c), the histogram for low-level CTP had two peaks, at around 0 and 600 hPa. The latter peak was due to cases when the low clouds in the OCA data were collocated with NHM clouds at high levels. About half of those cases had small CWP values, around 10 g m^{-2} with COT well below 1; these values indicate optically very thin clouds with large uncertainty in the OCA retrieval (EUMETSAT 2016b). The mean error and RMSE for low clouds were 182.9 hPa and 317.7 hPa, respectively. The histogram for mid-level clouds also had two peaks, a negative peak and a positive one. The resulting mean error and RMSE were 60.9 hPa and 235.3 hPa, respectively. Many OCA mid-level clouds seemed to be collocated with low or high NHM clouds because NHM

resolved fewer clouds at mid-levels. For high clouds, the mean error and RMSE were -20.9 hPa and 172.7 hPa, respectively.

Figure 4.5 shows example distributions of COT, CTP, and CWP derived from OCA, and the differences of CWP between OCA and NHM at 0200 UTC 8 September 2015. At this time, Typhoon Etau was in the sea south of Honshu Island, and a stationary front stretched along the Honshu coast. In the vicinity of the typhoon center and this front, there were some areas where the CWP was large, with high-level CTPs and thick COTs, but OCA CWP was substantially reduced compared to NHM CWP. This underestimation of CWP seemed to have been caused by large errors of COT, which are generally seen in association with deep clouds of tropical convections or extratropical fronts (EUMETSAT 2016b).

4.3. Assimilation experiments with pseudo-relative humidity derived from OCA products

4.3.1. Construction of pseudo-relative humidity

We next proceed to the assimilation of OCA products. Given the fact that large gaps between OCA CWP and NHM CWP were occasionally found in the first-guess departure statistics, and because hydrometeor species are not analysis variables in JNoVA, we decided to assimilate OCA products as pseudo-RH. For the construction of pseudo-RH, it is first necessary to detect cloud layers. Once cloud layers are determined, RH profiles within the clouds are set at around 90 %, with slight variations with height, as described in Zhang et al. (2010). Thus, we obtain pseudo-RH data where clouds exist. Previous studies, as mentioned in Section 4.1, have attempted to assimilate such retrieved RH by similar methods. RH assimilation is easy to implement but may seem rather ad hoc compared with more sophisticated approaches such as direct assimilation of radiances. As a first step, our focus was on the feasibility of assimilating these OCA products, the first to be derived from all 16

AHI channels. Thus, the main objective of these assimilation experiments was to examine the characteristics of these high-resolution and multi-channel products when utilized for mesoscale data assimilation.

Considering the results of the data verifications, we targeted only liquid clouds having COT below 50 and CTP below the 440-hPa level for assimilation to avoid OCA data with large uncertainties due to the presence of multilayered clouds and deep convection. In order to avoid uncertainties in optically thin clouds, the lower threshold value was also set for LWP (≧30 g m^{-2}).

OCA estimates CTP and CTH directly, but the corresponding cloud base height (CBH) is obtained by subtracting cloud geometric thickness (CGT) from CTH. For liquid clouds, CGT is defined as the ratio of LWP to the cloud-averaged liquid water content (LWC, Seaman et al. 2017). In this study, a fixed value of 0.30 g m^{-3}, supposedly representing ordinary cumulus and stratus clouds, was used for LWC. CGT and CBH were calculated as in Eqs. (4. 3) and (4. 4).

$$CGT = \frac{LWP}{LWC}\,, \tag{4.3}$$

$$CBH = CTH - CGT\,. \tag{4.4}$$

Underestimation of LWP due to precipitation effects may therefore result in a high bias in CBH. Estimated OCA CBHs were validated by CBHs observed by ceilometer at eight airports in the southern Kanto Region and the Izu Islands in the Pacific Ocean during the daytime on 7−10 September 2015. Because ceilometers only reliably detect cloud layers below 4,000 m (Poyer and Lewis 2009), OCA CBHs having CTHs below that level were compared. OCA CBHs tended to be higher than ceilometer CBHs: the correlation coefficient between OCA CBH and ceilometer CBH was 0.30, and their mean difference was 885.6 m.

4.3.2. Experimental design

Assimilation experiments were conducted with JNoVA for heavy rainfall events that occurred on three different days, 9 September 2015, and 4 and 5 July 2017. We focus mainly on the 2015 case to investigate the impact of the assimilation of OCA pseudo-RH on the analysis and forecast fields of various variables, as described in Section 4.3.3.

JNoVA is an incremental 4D-Var system for mesoscale analysis of the area around Japan; it has a 5-km (outer model) and 15-km (inner model) horizontal resolution and 50 vertical layers. Surface and upper-air observations obtained by sondes and wind profilers, radar, and satellites, including Himawari-8 AMVs and CSRs, are assimilated hourly within a 3-h time window (JMA 2019). The JNoVA domain, the topography around Japan, and the names of the regions mentioned in this article are shown in Figure 4.6. Note that the OCA data do not cover some western parts of the JNoVA domain (west of 120°E).

In TEST experiments, pseudo-RH data derived from OCA products were assimilated in four forecast-analysis cycles of JNoVA during the daytime (0000 to 0900 UTC) each day, along with other observational data used for operational JMA NWP. In CNTL experiments, only operationally used data were assimilated. The analysis results at 0900 UTC were used as the initial conditions for 39-h forecasts. We compared the analyses and the forecasts between TEST and CNTL to evaluate the impact of pseudo-RH assimilation.

OCA pseudo-RH data, which were originally obtained in OCA pixels with a 2-km resolution, were thinned to around 40 km before assimilation. When CBH was below 300 m, pseudo-RH data above that level were used to avoid the effects of obstructions nearby the surface. The magnitude of the observation error was fixed at 30 %. In the quality control process, if OCA did not detect any clouds in a certain grid where the first-guess RH was above the threshold value for the existence of a

cloud, following Zhang et al. (2010), the pseudo-RH in that gird was set to a climatological clear-sky value derived from sonde observations from the past 10 years (Table 4.4). Then, they went through general pre-analysis QC procedures, including gross error, internal consistency, and spatial checking.

4.3.3. Results for the heavy rainfall event on 9 September 2015

The first assimilation experiment case was for a heavy rainfall event on 9 September 2015. Figure 4.7 shows the weather map and the Himawari-8 IR and VIS composite image at 0000 UTC on that day. Typhoon Etau was on the verge of making landfall on Japan's main island (Honshu Island); it later moved northward and then over the Japan Sea in the evening. Another typhoon (Typhoon Kilo) located over the sea southeast of Typhoon Etau was moving northwestward. The moist air circulating around these typhoons brought torrential rainfalls to a wide area of Japan and, in particular, to the Kanto and Tohoku regions of eastern Japan, and this rainfall continued into the next day. The northward movement of low clouds over the sea south of Honshu, recognized in consecutive Himawari-8 images, suggested continuous low-level inflows to these regions.

Figure 4.8 shows the first-guess and analysis departure statistics during the whole assimilation period and the distribution map of pseudo-RH data points assimilated in the last time slot of the fourth cycle. Overall, assimilated OCA pseudo-RH had a slight positive bias against the first-guess and analysis RH. As expected, pseudo-RH data of around 90 % were obtained for the whole area, including over the ocean south of Japan, where low clouds, possibly associated with low-level inflows mentioned above, were observed. In contrast, pseudo-RH data of around 70 % or less were obtained where OCA did not detect clouds, but first-guess RH values exceeded the threshold for the existence of clouds. Figure 4.9 shows differences in the analysis results between TEST and CNTL at the end of the

assimilation period. Significant changes in water vapor fields were seen in the lower to middle levels (Fig. 4.9a–c). Sea surface pressure and wind speed at the surface and at 850 hPa were also slightly changed in TEST compared with CNTL.

Next, the extended forecast results in TEST and CNTL were examined. Figure 4.10 shows the differences of RH and wind speed at 850 hPa between TEST and CNTL at forecast times (FTs) of 9 h, 12 h, and 15 h. Bands of increased RH stretched from the southwest, over the ocean, toward the Kanto Region (marked by dashed ellipses in Figs. 4.10a─c), and gradually shifted northward and intruded farther over Kanto. An increase in southerly wind speed concurrent with these humidity changes suggests that the low-level inflows from the sea south of Japan had intensified over the area. This relationship between humidity and wind speed changes can be explained by the so-called 4D-Var tracer effect (Geer et al. 2018). In a 4D-Var system, winds were inferred from constituent transport including humidity through the adjoint of the model. Intensified convergences in northern Kanto and, later, in southern Kanto, suggested by the meeting of increased southwest to south winds with southeast winds, could eventually cause changes in the intensity and distribution of the heavy rainfalls continuing over the region during those hours.

In Fig. 4.11, forecasts of the 3-h precipitation amount at the same hour by TEST and CNTL are shown along with radar and rain gauge observations (radar/rain gauge-analyzed precipitation; RAP). The heavy rainfall bands over the region were better reproduced by TEST than by CNTL. When validation was conducted in the whole forecast domain over a longer forecast time (3 h to 24 h), threat and bias scores of the 3-h amount of forecast rainfall improved overall, especially in the early forecast hours, though a tendency for TEST to overestimate the amount prevailed in later hours (Fig. 4.12).

Finally, profiles of forecast RH, temperature, wind, and geopotential height were validated against sonde observations. Figure 4.13 shows their differences from

observations (averages at the 17 sonde stations) at 3-h, 15-h, and 27-h FTs. The RH mean error profiles differed slightly between TEST and CNTL, mostly within a few percent. At FT03, TEST showed a positive bias at around 850 hPa and below in contrast to CNTL (Fig.4.13a). The tendency toward slightly wetter conditions at low levels in TEST compared to CNTL was also seen at FT15 and even at FT27 (Figs. 4.13e and 13i). The temperature mean error profiles in TEST were quite similar to those in CNTL, except that they exhibited a little stronger negative bias at mid- to low levels (Figs. 4.13b, f, and j). The shapes of the u- and v-component wind speed profiles sometimes varied between TEST and CNTL, though the bias differences were within 1 m s^{-1}. The geopotential height validation results were almost the same in TEST and CNTL (not shown). The RMSE profiles of all variables in TEST indicated no improvement compared with CNTL.

4.3.4. Results for the heavy rainfall event on 4 - 5 July 2017

The other two experiments, conducted on 4 and 5 July 2017, were examined in the same manner. Here we focus on only the precipitation forecast results. The heavy rainfalls over these two days were associated with a stationary front typical of the early summer rainy season in Japan. Because OCA data for the assimilation cycles were available during only the daytime, separate experiments were conducted on 4 and 5 July.

Figure 4.14 shows the weather map, the IR and VIS composite image, and the distribution of RH analysis differences at 700 hPa between TEST and CNTL at 0000 UTC each day. At 0000 UTC 4 July, a stationary front extended from the Korean Peninsula to northern Japan across the Japan Sea, and Typhoon Nanmadol was over Kyushu. The typhoon moved eastward, crossing western Japan, and then became extratropical and dissipated over the Pacific. In contrast, the front over the Japan Sea gradually moved southward toward western Japan, and the meeting of this front with

the southerly inflows caused heavy rainfall (as much as roughly 350 mm) in the coastal Japan Sea areas from the late evening (0900 UTC) to the next morning. At 0000 UTC 5 July, this front was over western Japan, and it stayed in the region for the next few days. As warm, moist air from the south streamed toward the front from 5 to 6 July, heavy rainfall bands formed in northern Kyushu, and one of these bands brought localized heavy rainfall of 500 mm or more within 24 h.

On both 4 and 5 July, water vapor fields in the initial conditions were changed in TEST compared with CNTL as a result of the assimilation of pseudo-RH (Fig. 4.14). However, on 4 July, deep convection around the front over western Japan and the typhoon in Kyushu (represented by white in Fig. 4.14b) prevented pseudo-RH data from being obtained; as a result, information about the southerly inflows to these regions was lacking. On 5 July, however, low clouds in the vicinity of the front were recognizable. Moving images from Himawari-8 showed that these clouds, transported by northwesterly and southwesterly winds on either side of the front, were streaming into northern Kyushu from the East China Sea during the daytime period corresponding to the assimilation cycles. Accordingly, the OCA pseudo-RHs were derived from these clouds.

The precipitation forecast differences between TEST and CNTL are shown in Fig. 4.15 as the threat and bias scores for 3-h rainfalls at FTs of 3 to 24 h. On 5 July, but not on 4 July, the scores showed overall improvement in TEST compared with CNTL. The small differences between TEST and CNTL on 4 July may be owing to the lack of pseudo-RH data from the south and southwest side of the front, where the low-level inflows to western Japan presumably occurred.

Distributions of the 3-h rainfall in the TEST and CNTL forecasts were compared with observations at FTs of 3 to 12 h on 5 July (Fig. 4.16). In TEST, the heavy rainfall areas in northern Kyushu were more locally concentrated than in CNTL, and more like the observations at FT03. At later FTs, when heavy rainfalls

spread from the northwest to the east coast of Kyushu, TEST was not able to capture some areas of intensified rainfall, but it still seemed overall to reproduce rainfall better than CNTL. CNTL underestimated rainfall intensities in the region during the forecast period, as is also indicated by the much smaller bias scores of CNTL compared with TEST (Fig. 4.15d).

4.4. Discussion

Though cloud properties retrieved by satellites have been previously compared with conventional data sets, with Himawari-8 data, we were able to perform comparisons at an unprecedented high resolution and frequency over all of Japan. The approximately 60 % to 70 % agreement that we found between the OCA and conventional data seems acceptable with reference to previous studies (e.g., Hahn et al. 2001), though the resolution of satellite cloud data was poorer in past studies. Because the OCA data were obtained with much higher spatial and temporal resolutions than the data used for verification, most OCA data could not be evaluated in this study. Determining how to perform a data comparison properly between data sets with different representativeness is a challenging task.

Ground-based remote-sensing observations by instruments such as ceilometers may be useful for verifying high-resolution satellite data. Several studies have found that ceilometers are better able to capture CBH at low levels (Costa-Surós et al. 2013; Sharma et al. 2016), whereas satellites sometimes fail to obtain low-level CBHs, especially for precipitable clouds. Meerkötter and Zinner (2007) found that CBHs of optically thin water clouds in their earliest formation stage are consistent between satellite and ceilometer measurements. In this study, we targeted such water clouds mainly for assimilation, and we carried out our comparisons for them only. CWC was a fixed value under the assumption of a homogeneous cloud vertical structure. To perform accurate validations of various kinds of clouds, including mid- to high-

level clouds, more realistic settings for vertical distributions and the utilization of other types of observations such as spaceborne radar observations (Seaman et al. 2017) will be necessary. The comparison with passive microwave satellite observations may also be helpful (e.g. Greenwald et al. 2018). As for estimation of CBH, Noh et al. (2017) developed a statistical algorithm to consider more realistic vertical distribution of CWP within the cloud profile. Their algorithm showed better performance than Seaman et al. (2017) when validated against CloudSat CPR observations and is currently used in the National Oceanic and Atmospheric Administration Joint Polar Satellite System cloud products. It would be worthwhile to derive OCA CBH by using this algorithm and see whether the estimate accuracy improves.

In the comparison with model outputs, a significant bias was detected in OCA CWP. It seemed that there were too large gaps between model hydrometeor mixing ratios and those of OCA to deal with them as control variables in JNoVA. We therefore decided to assimilate OCA data as pseudo-RH without making major changes to the current system. The method used to construct the pseudo-RH data set and the preprocessing settings in JNoVA, including quality control, the magnitude of observation error, and data thinning, were established on a rather ad hoc basis and may need improvement. The main purpose of this study was to demonstrate the characteristics and possible impact of the new data when utilized in mesoscale assimilation. The results of the assimilation experiments suggest that pseudo-RHs well captured low-level water vapor transport from the ocean. They helped show the creation and intensification of convergences as low-level inflows continued to stream toward the rainfall areas. However, pseudo-RHs were not obtained from mature or aging convection cells around a stationary front, as seen in the experiment on 4 July 2017; as a result, the assimilation of pseudo-RH had little effect on the reproduction of intensified rainfall in the vicinity of the front.

In a future study, other variables more directly related to cloud properties than pseudo-RH should be targeted for assimilation. The assimilation of cloud properties such as OCA could be an alternative way to effectively utilize cloud- and precipitation-affected data in existing mesoscale data assimilation systems, given the fact that the direct assimilation of all-sky infrared radiances and visible reflections has not been realized operationally. Further data verification and experimental assimilation attempts may also lead to the development of the observation operators that will be needed when the radiances from which these products are derived are directly assimilated in future systems.

4.5. Conclusion

Newly developed Himawari-8 OCA products derived from all 16 AHI channels were evaluated, mainly from the perspective of utilizing them in mesoscale data assimilation to produce better initial conditions for heavy rainfall predictions. We conducted data verification and preliminary assimilation experiments to examine the data characteristics and impacts on analysis and forecast fields.

Data verifications against different types of observations and model outputs were performed to assess the data representativeness of the new products and to detect potential biases. The data consistencies seemed satisfactory when OCA data were obtained under single cloud layer conditions without strong vertical development, whereas large uncertainties were found when multilayer or convective clouds were present. These evaluation results can also provide necessary information for utilizing OCA data for uses other than the development of assimilation strategies, such as nowcasting and weather monitoring.

OCA products were assimilated as RH data with JNoVA for heavy rainfall cases. Assimilation of OCA pseudo-RH caused substantial changes to water vapor fields in the initial conditions, especially where OCA clouds were detected at low

levels over the ocean. When they successfully captured low-level inflows to the rainfall regions, they were able to significantly impact the precipitation forecasts at later forecast times.

Although the data used for assimilation were limited to water clouds at relatively low levels and the methods used to assimilate them as pseudo-RH are not so very refined, our results suggest that OCA data have the potential to improve rainfall forecasts by providing high-resolution water vapor information at high frequency and with wide coverage. Ways to further utilize these superior data obtained by new-generation GEOs in mesoscale assimilation need to be explored.

Chapter 5 Discussion and conclusion

5.1. Discussion

Based on the conclusions in Chapters 2, 3, and 4, we further discussed some remaining issues regarding the mesoscale NWP in dealing with high-resolution GEO data. The DA experiments conducted in this study included a heavy rainfall caused by a stationary front in the Kyushu and Chugoku Regions (in Chapter 2), a cold vortex in northern Japan (in Chapter 3), a torrential rainfall event in the Kanto and Tohoku Regions, and other two heavy rainfall cases in the northern Kyushu and Chugoku Regions (in Chapter 4). JNoVA was the DA system used in all the experiments. While the impacts of the new Himawari data on analyses and forecasts around Japan were overall positively found, it is necessary to check whether their impacts were rational and optimal by comparing each conclusion. We need to formulate a future strategy to utilize the data better to understand mesoscale weathers further.

5.1.1. Observation error correlations in the assimilation of high-resolution data

In Chapters 2 and 3, we verified and used RS-AMVs derived from MTSAT-1R (Himawari-6) and Himawari-8 in mesoscale DA experiments. RS-AMVs represented local scale winds in the vicinity of a front and a cold vortex better than ordinary AMVs, thus resulted in a slight improvement in the extended forecasts, especially in the early hours. As discussed in Chapter 3, one of the reasons why the impacts were positive but subtle may be that the rapid scan areas where RS-AMVs were obtained were limited to just around Japan, and the assimilation impacts on initial conditions disappeared relatively soon as the disturbances moved eastward while the effects of boundary conditions gradually prevailing. In addition and more importantly, it may be necessary to improve the DA systems so that they can extract

meaningful information more effectively out of high spatial and temporal GEO data. This study examined the optimal thinning length scale, assimilation frequency, and data selection to avoid spatial, temporal, and inter-channel observation error correlations. While such measures were necessary and adequate to some extent, a large amount of data were discarded, and some vital information may have been missed.

Since DA systems, including JNoVA, usually assume that the observation error for each observation is uncorrelated with the errors of all other observations, the observation error covariance matrix (**R** appeared in Eq. 1.9 of Chapter 1) is set to be diagonal. For a very dense observation network, it is necessary to spatially thin original data to some distances to avoid degradation of analysis (e.g., Liu and Rabier 2003). However, Rainwater et al. (2015) demonstrated with simple models that such data thinning and observation inflation methods could lead to grossly suboptimal analyses, particularly for small-scale features. Because severe mesoscale events associated with fronts, tropical cyclones, and convective systems include important small-scale features that GEOs can capture, future DA algorithms should adequately consider correlated observation error while considering the extra computational cost. Recent studies, or even a few operational NWP systems, consider observation error correlations using non-diagonal observation error covariance matrices (Bormann et al. 2016; Campbell et al. 2017). Okamoto et al. (2019) directly assimilated all-sky Himawari-8 infrared radiances into a mesoscale DA system and showed that spatial and inter-channel observation error correlations were higher in cloudy conditions than under clear sky. Dealing with this observation error correlation issue may be the key to making the best use of these new high-resolution GEO data, including cloud and precipitation affected observations.

5.1.2. Effects of water vapor transportation from the sea

Next, we focused on OCA, another new product of Himawari-8, in Chapter 4. In contrast to those of RS-AMVs, the assimilation experiments of OCA showed significant impacts on the initial states of water vapor fields, and the effects on the precipitation forecasts lasted pretty long, especially in the Kanto and Tohoku case where low-level inflows from over the ocean seemed to play the crucial role. While Kunii et al. (2016) assimilated Himawari-8 RS-AMV in the same case and suggested the importance of moisture advection by the ensemble-based correlation analysis, this study directly evaluated the assimilation impact of water vapor information retrieved from all the channels of AHI. The pseudo-RHs were successfully obtained at low to mid-levels with broad coverage, and their assimilation impacts on rainfall forecasts were significant. In the same Kanto and Tohoku case, a few studies (e.g., Kitabatake et al. 2017; Nakamura et al. 2020) have found that the characteristics in the synoptic-scale fields, including upper-tropospheric trough, the two typhoons around Japan and the Okhotsk high pressure formed favorable conditions for the intensification and duration of rainfalls. GEO observations are generally good at capturing such synoptic-scale phenomena either by wind vectors or by water vapor information with their wide coverage. Besides such case-dependent environmental factors, there may be some possible reasons for the relatively more significant impact of OCA compared to RS-AMV: Firstly, OCA was derived from 10-min full disk scans, thus obtained in the broader area than RS-AMV in Chapter 3. Secondly, because assimilation of water vapor in the form of RHs can also extract wind information through the tracer effect in 4D-var (Bonavita et al. 2020), the advection of the moisture from the sea that could help intensify rainfalls might be better captured. Currently, only Himawari-8 seems to be able to provide such water vapor information with good coverage at low to high levels both on land and sea with such a frequency as 10 min. The results of this study showed that the new GEO could

capture low-level moisture advection that triggered mesoscale heavy rainfalls as well as the synoptic-scale environment.

5.1.3. Other issues for further study

In Chapters 2, 3, and 4, the assimilation impacts seemed different from case to case, depending on the space-time scales of phenomena and data representativeness. In order to optimize DA to get the maximum impacts of RS-AMV and OCA, further case studies and statistical evaluation in a longer assimilation period may be necessary. Although it is still difficult to directly use non-diagonal **R** to assimilate high-resolution GEO data, especially in the current routine NWP, further research efforts should keep going, as mentioned above.

Lastly, we focused only on the observation error characteristics in DA systems from the perspective of utilizing the new GEO data in the existing DA system. In order to realize genuinely optimal DA for GEO data, other factors including observation operators, related model processes, and DA methods should also be considered and developed, which seems challenging for the moment because it requires a major change in the DA system, thus would be remaining tasks for future study.

5.2. Conclusion

We investigated the observational error characteristics and data representativeness of Himawari RS-AMV and OCA by evaluating with different kinds of observations and mesoscale model simulations. Then, we examined the optimal settings in mesoscale DA, such as observation error, the length scale of data thinning, assimilation interval time, and QC methods. Finally, we conducted DA experiments on significant mesoscale meteorological events in several regions of Japan, including heavy rainfalls caused by stationary fronts and typhoons. The

results showed that assimilation of multi-channel high spatiotemporal resolution Himawari-8 data provides a potential to improve wind and water vapor analysis fields around Japan and the forecasts of those prognosis variables and rainfalls in later hours. The findings obtained from Chapters 2, 3, and 4 are summarized as follows:

In Chapter 2, RS-AMVs derived from MTSAT-1R (Himawari-6), the former JMA's GEO before Himawari-8 were assimilated with JNoVA using different lengths of assimilation time slot and time intervals of spatial thinning. When these conditions were optimally set, the impacts of RS-AMVs were positively seen as the improvement of wind analyses in initial conditions for a heavy rainfall event in western Japan in August 2012. The forecasted rainfall amount was increased near the stationary front, and the verification scores were slightly improved in the early forecast hours. It seemed that RS-AMVs were capable of tracking clouds more accurately with their higher time resolution as expected and enabled to detect smaller-scale wind variations. It is revealed that the upper divergence and the lower convergence near the front at sea only captured by RS-AMVs may have corresponded with the intensified convective activities and led to the increase in the amount of precipitation.

In Chapter 3, Himawari-8 RS-AMVs in 7 channels were validated and assimilated in a cold vortex case in northern Japan in June 2016. While Chapter 2 focused on the benefits of a higher frequency of observations, Chapter 3 investigated the new multi-channel RS-AMVs obtained from the new imager, AHI, of high space-time resolution in terms of their data characteristics. Observation error characteristics in each channel were examined as well as inter-channel observation error correlations among the channels. Errors were slightly larger in WV than in VIS and IR channels. Significant negative biases relative to sonde winds were seen at high levels above 400 hPa in VIS, IR, and CO_2, whereas slightly positive biases were

noticeable in WV at mid- to high levels (700−400 hPa). The DA results varied slightly depending on the channels used for assimilation, which might be caused by different error characteristics of RS-AMVs in different channels. When RS-AMVs in all the channels were assimilated in an optimized way, the wind forecasts in northern Japan agreed best with sonde and wind profiler observations, probably because of their better coverage from low to high levels. The initial wind analyses near the cold vortex were changed to intensify the convergence around its center slightly, thus positively affecting the forecasts in later hours. It may be necessary to investigate further optimal methods of data selection and QC for these multi-channel high-resolution GEO data to be fully utilized.

In Chapter 4, Himawari-8 OCA derived from all 16 channels of the AHI were validated with different datasets to determine their data characteristics and detect potential biases in July 2017 in Japan. OCA data seemed to be consistent with observations of water clouds with moderate optical thicknesses. Assimilation of OCA pseudo-relative humidities significantly improved the initial conditions of water vapor fields on a few heavy rainfall events that happened in September 2015 in eastern Japan and in July 2017 in the Kyushu Region. When the OCA data captured low-level inflows from over the ocean, they positively impacted precipitation forecasts at later forecast times. The results of the DA experiments successfully demonstrated the characteristics and possible positive impacts of the new data. The method to construct the pseudo-RH data and the preprocessing settings in JNoVA, including quality control, the magnitude of observation error, and data thinning, were established on a somewhat ad hoc basis and may need to improve in the future study.

Emerging new-generation GEOs have brought opportunities to improve mesoscale forecasts with better data of increased quantity and quality. However, we need further developments in order to exploit them in existing DA systems. The

difficulties of dealing with a vast amount of high-resolution data in multi-channels, including cloud and precipitation affected observations, are primary issues and seem to hinder the benefits of GEO data. How to make the best use of these novel observations still requires further research efforts. Further understanding of their data characteristics can help design the DA systems optimally, thus estimating the atmospheric state in detail as accurately as possible and improving the initial conditions of the mesoscale forecast. They also help understand a variety of mesoscale atmospheric phenomena by adding high-resolution wind and water vapor information particularly over the ocean and applying models to simulate these phenomena better. In addition, the feedback from our study may help develop more valuable products obtained by the current and future advanced satellite sensors.

References

Bedka, K. M., and J. R. Mecikalski, 2005: Application of satellite-derived atmospheric motion vectors for estimating mesoscale flows. *J. Appl. Meteor.*, **44**, 1761–1772.

Bedka, K. M., C. S. Velden, R. A. Petersen, and W. F. Feltz, and J. R. Mecikalski, 2009: Comparisons of satellite-derived atmospheric motion vectors, rawinsondes, and NOAA wind profiler observations. *J. Appl. Meteor.*, **48**, 1542–1561.

Berger, H., R. Langland, C. S. Velden, C. A. Reynolds, and P. M. Pauley, 2011: Impact of enhanced satellite-derived atmospheric motion vector observations on numerical tropical cyclone track forecasts in the western North Pacific during TPARC/TCS-08. *J. Appl. Meteor. Climatol.*, **50**, 2309–2318.

Berrisford, P., D. Dee, P. Poli, R. Brugge, K. Fielding, M. Fuentes, P. Kallberg, S. Kobayashi, S. Uppala, and A. Simmons, 2011: The ERA-Interim archive version 2.0, *ERA Report Series 1, ECMWF*. [Available at https: //www.ecmwf.int/node/8174.]

Bessho, K., K. Date, M. Hayashi, A. Ikeda, T. Imai, H. Inoue, Y. Kumagai, T. Miyakawa, H. Murata, T. Ohno, A. Okuyama, R. Oyama, Y. Sasaki, Y. Shimazu, K. Shimoji, Y. Sumida, M. Suzuki, H. Taniguchi, H. Tsuchiyama, D. Uesawa, H. Yokota, and R. Yoshida, 2016: An introduction to Himawari-8/9–Japan's new generation geostationary meteorological satellites. *J. Meteor. Soc. Japan*, **94**, 151–183.

Bonavita, M., A. J. Geer, and M. Hamrud, 2020: All-sky microwave radiances assimilated with an ensemble Kalman filter, *Mon. Wea. Rev.*, **148**, 2737-2760.

Bormann, N., and P. Bauer, 2010: Estimates of spatial and interchannel observation-error characteristics for current sounder radiances for numerical weather prediction. I: Methods and application to ATOVS data. *Quart. J. Roy. Meteor. Soc.*, **136**, 1036–1050.

Bormann, N., M. Bonavita, R. Dragani, R. Eresmaa, M._Matricardi, and A. McNally, 2016: Enhancing the impact of IASI observations through an updated observation-error covariance matrix. *Quart. J. Roy. Meteor. Soc.*, **142**. 1767–1780.

Bresky, W. C., J. M. Daniels, A. A. Bailey, and S. T. Wanzong, 2012: New methods toward minimizing the slow speed bias associated with atmospheric motion vectors. *J. Appl. Meteor. Climatol.*, **51**, 2137–2151.

Bretherton, C. S., E. Klinker, A. K. Betts, and J. A. Coakley, Jr., 1995: Comparison of ceilometer, satellite, and synoptic measurements of boundary-layer cloudiness and the ECMWF diagnostic cloud parameterization scheme during ASTEX. *J. Atmos. Sci.*, **52**, 2736–2751.

Campbell, W. F., E. A. Satterfield, B. Ruston, and N. L. Baker, 2017: Accounting for correlated observation error in a dual-formulation 4D variational data assimilation system. *Mon. Wea. Rev.*, **145**, 1019–1032.

Coordination Group for Meteorological Satellites (CGMS) 2018: Preparing for the next generation of meteorological satellites. Satellite User Readiness Navigator (SATURN). [Available at https: https://www.wmo-sat.info/satellite-user-readiness/.]

Costa-Surós, M., J. Calbó, J. A. González, and J. Martin-Vide, 2013: Behavior of cloud base height from ceilometer measurements. *Atmos. Res.*, **127**, 64–76.

Costa-Surós, M., J. Calbó, J. A. González, and C. N. Long, 2014: Comparing the cloud vertical structure derived from several methods based on radiosonde profiles and ground-based remote sensing measurements. *Atmos. Meas. Tech.*, **7**, 2757–2773.

Courtier, P., J.-N. Thépaut, and A. Hollingsworth, 1994: A strategy for operational implementation of 4D-var, using an incremental approach. *Quart. J. Roy. Meteor. Soc.*, **120**, 1367–1387.

EUMETSAT, 2016a: MTG-FCI: ATBD for Optimal Cloud Analysis Product. EUM/MTG/DOC/11/0654 v5, EUMETSAT, Darmstadt, Germany, 81 pp. [Available at https: //navigator.eumetsat.int/product/EO:EUM:DAT:MSG: OCA/ print.]

EUMETSAT, 2016b: Optimal Cloud Analysis: Product Guide. EUM/TSS/MAN/14/770106 v2A, EUMETSAT, Darmstadt, Germany, 31 pp. [Available at https://navigator.eumetsat.int/product/EO:EUM: DAT:MSG: OCA/ print.]

Fabry, F., and J. Sun, 2008: For how long should what data be assimilated for the mesoscale forecasting of convection and why? Part I: On the propagation of initial condition errors and their implications for data assimilation. *Mon. Wea. Rev.* **138**, 242–255.

Fan, X., and J. S. Tilley, 2005: Dynamic assimilation of MODIS-retrieved humidity profiles within a regional model for high-latitude forecast applications. *Mon. Wea. Rev.*, **133**, 3450–3480.

Folger, K., and M. Weissmann, 2014: Height correction of atmospheric motion vectors using satellite lidar observations from CALIPSO. *J. Appl. Meteor. Climatol.*, **53**, 1809–1819.

Folger, K., and M. Weissmann, 2016: Lidar-based height correction for the assimilation of atmospheric motion vectors. *J. Appl. Meteor. Climatol.*, **55**, 2211–2227.

Fujita, T. T., E. W. Fearl, and W. E. Shenk, 1975: Satellite-tracked cumulus velocities. *J. Appl. Meteor.*, **14**, 407–413.

Geer, A. J., and Coauthors, 2018: All-sky satellite data assimilation at operational weather forecasting centres. *Quart. J. Roy. Meteor. Soc.*, **144**, 1191–1217.

Greenwald, T. J., R. Bennartz, M. Lebsock, and J. Teixeira, 2018: An uncertainty data set for passive microwave satellite observations of warm cloud liquid water path. *J. Geophys. Res.*, **123**, 3668–3687.

Gustafsson, N., T. Janjić, C. Schraff, D. Leuenberger, M. Weissmann, H. Reich, P. Brousseau, T. Montmerle, E. Wattrelot, A. Bučánek, M. Mile, R. Hamdi, M. Lindskog, J. Barkmeijer, M. Dahlbom, B. Macpherson, S. Ballard, G. Inverarity, J. Carley, C. Alexander, D. Dowell, S. Liu, Y. Ikuta, and T. Fujita, 2018: Survey of data assimilation methods for convective-scale numerical weather prediction at operational centres. *Quart. J. Roy. Meteor. Soc.*, **144**, 1218–1256.

Hahn, C. J., W. B. Rossow, and S. G. Warren, 2001: ISCCP cloud properties associated with standard cloud types identified in individual surface observations. *J. Climate*, **14**, 11–28.

Hollingsworth, A., and P. Lönnberg, 1986: The statistical structure of short-range forecast errors as determined from radiosonde data. Part I: The wind field. *Tellus*, **38A**, 111–136.

Hamada, A., and Takayabu, Y. N., 2016: Convective cloud top vertical velocity estimated from geostationary satellite rapid-scan measurements, *Geophys. Res. Lett.*, **43**, 5435–5441.

Hamada, T., 1979: Cloud wind estimation system summary of GMS system. *MSC Technical Note*, Special Issue **II-2**, 15–42 (in Japanese).

Harada, Y., H. Kamahori, C. Kobayashi, H. Endo, S. Kobayashi, Y. Ota, H. Onoda, K. Onogi, K. Miyaoka, and K. Takahashi, 2016: The JRA-55 Reanalysis: Representation of atmospheric circulation and climate variability, *J. Meteor. Soc. Japan*, **94**, 269–302.

Harper, K., L. W. Uccellini, E. Kalnay, K. Carey, and L. Morone, 2007: 50th anniversary of operational numerical weather prediction. *Bull. Amer. Meteor. Soc.* **56**, 527–530.

Hayashi, M., and K. Shimoji, 2013: Atmospheric motion vectors derivation algorithm. *MSC Technical Note*, **58**, 3–109 (in Japanese).

Hayashi, M., and P. Watts, 2016: Two-layer cloud retrieval using visible to infrared bands of Himawari-8. *EUMETSAT Meteorological Satellite Conference*, Darmstadt, Germany, EUMETSAT. [Available at https://www.eumetsat.int/website/home/News/ConferencesandEvents/PreviousEvents/DAT_2833302.html.]

Hernandez-Carrascal, A., and N. Bormann, 2014: Atmospheric motion vectors from model simulations. Part II: Interpretation as spatial and vertical averages of wind and role of clouds. *J. Appl. Meteor. Climatol.*, **53**, 65–82.

Holmlund, K., 1998: The utilization of statistical properties of satellite-derived atmospheric motion vectors to derive quality indicators. *Wea. Forecasting*, **13**, 1093–1104.

Honda, T., S. Kotsuki, G.-Y. Lien, Y. Maejima, K. Okamoto, and T. Miyoshi, 2018a: Assimilation of Himawari-8 all-sky radiances every 10 minutes: Impact on precipitation and flood risk prediction. *J. Geophys. Res.*, **123**, 965–976.

Honda, T., and Coauthors, 2018b: Assimilating all-sky Himawari-8 satellite infrared radiances: A case of typhoon Soudelor (2015). *Mon. Wea. Rev.*, **146**, 213–229.

Honda, Y., M. Nishijima, K. Koizumi, Y. Ohta, K. Tamiya, T. Kawabata, and T. Tsuyuki, 2005: A pre-operational variational data assimilation system for a nonhydrostatic model at Japan Meteorological Agency: Formulation and preliminary results. *Quart. J. Roy. Meteor. Soc.*, **131**, 3465–3475.

Ishibashi, T., 2011: Tangent linear approximation based observation data impact estimation in 4D-Var. *Quart. J. Roy. Meteor. Soc.*, **137**, 1898–1912.

Ishida, H., Y. Oishi, K. Morita, K. Moriwaki, and T. Y. Nakajima, 2018: Development of a support vector machine based cloud detection method for MODIS with the adjustability to various conditions. *Remote Sens. Environ.*, **205**, 390–407.

Japan Meteorological Agency, 2013: Outline of the operational numerical weather prediction at the Japan Meteorological Agency. *Appendix to WMO Technical Progress Report on the Global Data Processing and Forecast System (GDPFS) and Numerical Weather Prediction (NWP)*, 9–40.

Japan Meteorological Agency, 2019: Outline of the operational numerical weather prediction at the Japan Meteorological Agency. *Appendix to WMO Technical Progress Report on the Global Data-processing and Forecasting System and Numerical Weather Prediction Research*, JMA, Tokyo, Japan, 229 pp. [Available at https://www.jma.go.jp/jma/jma-eng/jma-center/nwp/outline2019-nwp/ index.htm.]

Johnson, G. L., and D. Suchman, 1980: Intercomparisons of SMS wind sets: A study using rapid-scan imagery. *Mon. Wea. Rev.*, **108**, 1672–1688.

Jones, T. A., and D. J. Stensrud, 2015: Assimilating cloud water path as a function of model cloud microphysics in an idealized simulation. *Mon. Wea. Rev.*, **143**, 2052–2081.

Jones, T. A., D. J. Stensrud, P. Minnis, and R. Palikonda, 2013: Evaluation of a forward operator to assimilate cloud water path into WRF-DART. *Mon. Wea. Rev.*, **141**, 2272–2289.

Joo, S., J. Eyre, and R. Marriott, 2013: The impact of MetOp and other satellite data within the Met Office global NWP system using an adjoint-based sensitivity method. *Mon. Wea. Rev.*, **141**, 3331–3342.

Kalnay, E., 2003: *Atmospheric Modeling, Data Assimilation and Predictability*. Cambridge University Press, 368pp.

Kalnay, E., M. Kanamitsu, R. Kistler, W. Collins, D. Deaven, L. Gandin, M. Iredell, S. Saha, G. White, J. Woollen, Y. Zhu, M. Chelliah, W. Ebisuzaki, W. Higgins, J. Janowiak, K. C. Mo, C. Ropelewski, J. Wang, A. Leetmaa, R. Reynolds, R. Jenne, and D. Joseph, 1996: The NCEP/NCAR 40-Year Reanalysis Project, *Bull. Amer. Meteor. Soc,* **77**, 437–472.

Kato, T., 2018: Representative height of the low-level water vapor field for examining the initiation of moist convection leading to heavy rainfall in East Asia. *J. Meteor. Soc. Japan*, **96**, 69–83.

Kazumori, M., 2018: Assimilation of Himawari-8 clear sky radiance data in JMA 's global and mesoscale NWP systems. *J. Meteor. Soc. Japan*, **96B**, 173–192.

Kitabatake, N., H. Tsuguti, and T. Kato, 2017: Effects of synoptic scale environmental flows on the heavy rainfall event in the Kanto and Tohoku district in September 2015. *Tenki*, **64**, 887–899 (in Japanese).

Kobayashi, S., Y. Ota, Y. Harada, A. Ebita, M. Moriya, H. Onoda, K. Onogi, H. Kamahori, C. Kobayashi, H. Endo, K. Miyaoka, and K. Takahashi, 2015: The JRA-55 Reanalysis: General specifications and basic characteristics. *J. Meteor. Soc. Japan*, **93**, 5–48.

Kunii, M., M. Otsuka, K. Shimoji, and H. Seko, 2016: Ensemble data assimilation and forecast experiments for the September 2015 heavy rainfall event in Kanto and Tohoku regions with atmospheric motion vectors from Himawari-8. *SOLA*, **12**, 209−214.

Langland, R. H., C. Velden, P. M. Pauley, and H. Berger, 2009: Impact of satellite-derived rapid-scan wind observations on numerical model forecasts of hurricane Katrina. *Mon. Wea. Rev.*, **137**, 1615–1622.

Lean, P., S. Migliorini, and G. Kelly, 2015: Understanding atmospheric motion vector vertical representativity using a simulation study and first-guess departure statistics. *J. Appl. Meteor. Climatol.*, **54**, 2479–2500.

Leese, J. A., C. S. Novak, and B. B. Clark, 1971: An automated technique for obtaining cloud motion from geosynchronous satellite data using cross correlation. *J. Appl. Meteor.*, **10**, 118–132.

Leonhard S., P. Frèrebeau, R. Buras-Schnell, and B. Mayer, 2016: A fast radiative transfer method for the simulation of visible satellite imagery. *J. Quant. Spectrosc. Radiat. Transf.*, **175**, 54–67.

Li, J., Z. Li, P. Wang, T. J. Schmit, W. Bai, and R. Atlas, 2017: An efficient radiative transfer model for hyperspectral IR radiance simulation and applications under cloudy-sky conditions, *J. Geophys. Res. Atmos.*, **122**, 7600–7613.

Lipton, A. E., and G. D. Modica, 1999: Assimilation of visible-band satellite data for mesoscale forecasting in cloudy conditions. *Mon. Wea. Rev.*, **127**, 265–278.

Liu, Z.-Q., and F. Rabier, 2003: The potential of high-density observations for numerical weather prediction: A study with simulated observations. *Quart. J. Roy. Meteor. Soc.*, **129**, 3013–3035.

Macpherson, B., B. J. Wright, W. H. Hand, and A. J. Maycock, 1996: The impact of MOPS moisture data in the U.K. Meteorological Office mesoscale data assimilation scheme. *Mon. Wea. Rev.*, **124**, 1746–1766.

Meerkötter, R., and T. Zinner, 2007: Satellite remote sensing of cloud base height for convective cloud fields: A case study. *Geophys. Res. Lett.*, **34**, L17805, doi:10.1029/2007GL030347.

Menzel, W. P., 2001: Cloud tracking with satellite imagery: From the pioneering work of Ted Fujita to the present. *Bull. Amer. Meteor. Soc.*, **82**, 33–47.

Migliorini, S., 2012: On the equivalence between radiance and retrieval assimilation. *Mon. Wea. Rev.*, **140**, 258–265.

Minamide, M., and F. Zhang, 2018: Assimilation of all-sky infrared radiances from Himawari-8 and impacts of moisture and hydrometer initialization on convection-permitting tropical cyclone prediction. *Mon. Wea. Rev.*, **146**, 3241–3258.

Mitrescu, C., T. L 'Ecuyer, J. Haynes, S. Miller, and J. Turk, 2010: CloudSat precipitation profiling algorithm—model description. *J. Appl. Meteor. Climatol.*, **49**, 991–1003.

Munro, R., C. C. Köpken, G. Kelly, J.-N. Thépaut, and R. Saunders, 2004: Assimilation of Meteosat radiance data within the 4D-Var system at ECMWF: Data quality monitoring, bias correction and single-cycle experiments. *Quart. J. Roy. Meteor. Soc.*, **130**, 2293–2313.

Nakajima, T., and M. D. King, 1990: Determination of the optical thickness and effective particle radius of clouds from reflected solar radiation measurements. Part I: Theory. *J. Atmos. Sci.*, **47**, 1878–1893.

Nakamura, Y., T. Miyakawa, and M. Satoh, 2020: The role of Typhoon Kilo (T1517) in the Kanto-Tohoku heavy rainfall event in Japan in September 2015. *J. Meteor. Soc. Japan*, **98**, 915–926.

Nakazawa, T., K. Bessho, S. Hoshino, T. Komori, K. Yamashita, Y. Ohta, and K. Sato, 2010: THORPEX–Pacific Asian Regional Campaign (T-PARC). *RSMC Tokyo-Typhoon Center Technical Review*, **12**, 1–4.

NASA, 2003: Formation flying: The afternoon "A-Train" satellite constellation. *NASA Facts*, FS-2003-1-053-GSFC. [Available at https://atrain.nasa.gov/publications/A-TrainFactSheet.pdf.]

Naud, C. M., J.-P. Muller, and E. E. Clothiaux, 2003: Comparison between active sensor and radiosonde cloud boundaries over the ARM Southern Great Plains site. *J. Geophys. Res.*, **108**, 4140, doi:10.1029/2002JD002887, D4.

Noh, Y.-J., and Coauthors, 2017: Cloud-base height estimation from VIIRS. Part II: A statistical algorithm based on A-train satellite data. *J. Atmos. Oceanic Technol.*, **34**, 585–598.

Okamoto, K., 2013: Assimilation of overcast cloudy infrared radiances of the geostationary MTSAT-1R imager. *Quart. J. Roy. Meteor. Soc.*, **139**, 715–730.

Okamoto, K., 2017: Evaluation of IR radiance simulation for all-sky assimilation of Himawari-8/AHI in a mesoscale NWP system. *Quart. J. Roy. Meteor. Soc.* **143**: 1517–1527.

Okamoto, K., A. P. McNally, and W. Bell, 2014: Progress towards the assimilation of all-sky infrared radiances: an evaluation of cloud effects. *Quart. J. Roy. Meteor. Soc.*, **140**, 1603–1614.

Okamoto, K., Y. Sawada, and M. Kunii, 2019: Comparison of assimilating all-sky and clear-sky infrared radiances from Himawari-8 in a mesoscale system. *Quart. J. Roy. Meteor. Soc.*, **145**, 745–766.

Otsuka, M., M. Kunii, H. Seko, K. Shimoji, M. Hayashi, and K. Yamashita, 2015: Assimilation experiments of MTSAT rapid scan atmospheric motion vectors on a heavy rainfall event. *J. Meteor. Soc. Japan*, **93**, 459–475.

Otsuka, M., M. Kunii, H. Seko, and K. Shimoji, 2016: Assimilation of Himawari-8 rapid scan atmospheric motion vectors. *Proc. 13th International Winds Workshop*, Monterey, USA. [Available at http://cimss.ssec.wisc.edu/iwwg/iww13/proceedings_iww13/.]

Otsuka, M., H. Seko, K. Shimoji, and K. Yamashita, 2018: Characteristics of Himawari-8 rapid scan atmospheric motion vectors utilized in mesoscale data assimilation. *J. Meteor. Soc. Japan*, **96B**, 111–131.

Otsuka, M., J. Matsumoto, and H. Seko, 2019: Geostationary satellite data assimilation in mesoscale forecast systems: A review. *Geogr. Rep. Tokyo Metro. Univ.*, **54**, 1–10.

Otsuka, M., H. Seko, M. Hayashi, and K. Koizumi, 2021: Data validation and mesoscale assimilation of Himawari-8 optimal cloud analysis products. *J. Atmos. Ocean. Technol.*, **38**, 223–242.

Oyama, R., A. Wada, and M. Sawada, 2016: Intensification of Typhoon Danas (1324) captured by MTSAT upper tropospheric atmospheric motion vectors. *SOLA*, **12**, 135–139.

Peubey, C., and A. P. McNally, 2009: Characterization of the impact of geostationary clear-sky radiances on wind analyses in a 4D-Var context. *Quart. J. Roy. Meteor. Soc.*, **135**, 1863–1876.

Poulsen, C. A., and Coauthors, 2012: Cloud retrievals from satellite data using optimal estimation: Evaluation and application to ATSR. *Atmos. Meas. Tech.*, **5**, 1889–1910.

Poyer, A. J., and R. Lewis, 2009: ASOS product improvement ceilometer replacement testing. *Extended Abstracts, 89th Annual Meeting*, Phoenix, AZ, AMS, 12A.5. [Available at https://ams.confex.com/ams/pdfpapers/146103.pdf.]

Rainwater, S., C. H. Bishop, and W. F. Campbell, 2015: The benefits of correlated observation errors for small scales. *Quart. J. Roy. Meteor. Soc.*, **141**, 3439–3445.

Rehbein, A., M. Rugna, M. P. Hobouchian, A. D. Moral, S. J. Goodman, D. T. Lindsey, and J. Thomas, 2020: A workshop on the next-generation environmental satellite constellations. *Bull. Amer. Meteor. Soc.*, **101**, E763–E770.

Reich, S., and C. Cotter, 2015: *Probabilistic Forecasting and Bayesian Data Assimilation*. Cambridge University Press, 308pp.

Renshaw, R., and P. N. Francis, 2011: Variational assimilation of cloud fraction in the operational Met Office Unified Model. *Quart. J. Roy. Meteor. Soc.*, **137**, 1963–1974.

Rodgers, E., R. C. Gentry, W. Shenk, and V. Oliver, 1979: The benefits of using short-interval satellite images to derive winds for tropical cyclones. *Mon. Wea. Rev.*, **107**, 575–584.

Rohn, M., G. Kelly, and R. W. Saunders, 2001: Impact of a new cloud motion wind product from Meteosat on NWP analyses and forecasts. *Mon. Wea. Rev.*, **129**, 2392–2403.

Rossow, W. B., and R. A. Schiffer, 1991: ISCCP cloud data products. *Bull. Amer. Meteor. Soc.*, **72**, 2–20.

Saito, K., and I. Takano 1986: An analysis of sub-synoptic scale cyclone using low level satellite winds derived from short interval GMS observation data. *MSC Technical Note*, **15**, 67–78 (in Japanese).

Saito, K., T. Fujita, Y. Yamada, J. Ishida, Y. Kumagai, K. Aranami, S. Ohmori, R. Nagasawa, S. Kumagai, C. Muroi, T. Kato, H. Eito, and Y. Yamazaki, 2006: The operational JMA nonhydrostatic mesoscale model. *Mon. Wea. Rev.*, **134**, 1266–1298.

Saito, K., J. Ishida, K. Aranami, T. Hara, T. Segawa, M. Narita, and Y. Honda, 2007: Nonhydrostatic atmospheric models and operational development at JMA. *J. Meteor. Soc. Japan*, **85B**, 271–304.

Salonen, K., J. Cotton, N. Bormann, and M. Forsythe, 2015: Characterizing AMV height-assignment error by comparing best-fit pressure statistics from the Met Office and ECMWF data assimilation systems. *J. Appl. Meteor. Climatol.*, **54**, 225–242.

Saunders, R., and Coauthors, 2018: An update on the RTTOV fast radiative transfer model (currently at version 12). *Geosci. Model Dev.*, **11**, 2717–2737.

Sawada, Y., K. Okamoto, M. Kunii, and T. Miyoshi, 2019: Assimilating every-10-minute Himawari-8 infrared radiances to improve convective predictability. *J. Geophys. Res.*, **124**, 2546–2561.

Scheck, L., M. Weissmann, and B. Mayer, 2018: Efficient methods to account for cloud-top inclination and cloud overlap in synthetic visible satellite images. *J. Atmos. Oceanic Technol.*, **35**, 665–685.

Schmetz, J., K. Holmlund, J. Hoffman, B. Strauss, B. Mason, V. Gaertner, A. Koch, and L. Van De Berg, 1993: Operational cloud-motion winds from Meteosat infrared images. *J. Appl. Meteor.*, **32**, 1206–1225.

Schmetz, J., D. Hinsman, and W. P. Menzel, 1999: Summary of the fourth international winds workshop. *Bull. Amer. Meteor. Soc.*, **80**, 893–899.

Seaman, C. J., Y.-J. Noh, S. D. Miller, A. K. Heidinger, and D. T. Lindsey, 2017: Cloud-base height estimation from VIIRS. Part I: Operational algorithm validation against CloudSat. *J. Atmos. Oceanic Technol.*, **34**, 567–583.

Sharma, S., R. Vaishnav, M. V. Shukla, P. Kumar, P. Kumar, P. K. Thapliyal, S. Lal, and Y. B. Acharya, 2016: Evaluation of cloud base height measurements from ceilometer CL31 and MODIS satellite over Ahmedabad, India. *Atmos. Meas. Tech.*, **9**, 711–719.

Shimizu, A., K. Saito, and M. Yamamoto, 2017: Image characteristics of the 16 bands of Himawari-8's AHI. *MSC Technical Note*, **62**, 39–71 (in Japanese).

Shimoji, K., 2014: Motion tracking and cloud height assignment methods for Himawari-8 AMV. *Proc. the 12th International Winds Workshop*, Copenhagen, Denmark. [Available at http://www.eumetsat.int/website/home/News/ ConferencesandEvents/PreviousEvents/DAT_2441511.html.]

Shimoji, K., and K. Nonaka, 2016: Current status of operational wind product in JMA/MSC. *Proc. 13th International Winds Workshop*, Monterey, USA. [Available at http://cimss.ssec.wisc.edu/iwwg/iww13/proceedings_ iww13/index.html.]

Stephens, G. L., 1978: Radiation profiles in extended water clouds. II: Parameterization schemes. *J. Atmos. Sci.*, **35**, 2123–2132.

Storto, A., and F. T. Tveter, 2009: Assimilating humidity pseudo-observations derived from the cloud profiling radar aboard CloudSat in ALADIN 3D-Var. *Meteor. Appl.*, **16**, 461–479.

Swinbank, R., 2010: Numerical Weather Prediction. *Data assimilation: Making sense of observations*, W. Lahoz, B. Khattatov, and R. Menard, Eds., Springer Science & Business Media, 381–406.

Tomassini, M., G. Kelly, and R. Saunders, 1999: Use and impact of satellite atmospheric motion winds on ECMWF analyses and forecasts. *Mon. Wea. Rev.*, **127**, 971–986.

Tsuyuki, T., 2008: Introduction to data assimilation. *Data Assimilation in Meteorology*, *Meteorological Research Notes*, (217), T. Tsuyuki and T. Kawabata, Eds., Meteorological Society of Japan, 1–32 (in Japanese).

Uchida, H., T. Ohshima, T. Hamada, and S. Osano, 1991: Low-level cloud motion wind field estimated from GMS short interval images in typhoon vicinity. *Geophys. Mag.*, **44**, 37–50.

Velden, C. S., and K. M. Bedka, 2009: Identifying the uncertainty in determining satellite-derived atmospheric motion vector height attribution. *J. Appl. Meteor. Climatol.*, **48**, 450–463.

Velden, C. S., C. M. Hayden, S. J. Nieman, W. P. Menzel, S. Wanzong, and J. S. Goerss, 1997: Upper-tropospheric winds derived from geostationary satellite water vapor observations. *Bull. Amer. Meteor. Soc.*, **78**, 173–195.

Velden, C. S., J. Daniels, D. Stettner, D. Santek, J. Key, J. Dunion, K. Holmlund, G. Dengel, W. Bresky, and P. Menzel, 2005: Recent innovations in deriving tropospheric winds from meteorological satellites. *Bull. Amer. Meteor. Soc.*, **86**, 205–223.

Velden, C., W. E. Lewis, W. Bresky, D. Stettner, J. Daniels, and S. Wanzong, 2017: Assimilation of high-resolution satellite-derived atmospheric motion vectors: Impact on HWRF forecasts of tropical cyclone track and intensity. *Mon. Wea. Rev.*, **145**, 1107–1125.

Vukicevic, T., and J. Paegle, 1989: The influence of one-way interacting lateral boundary conditions upon predictability in bounded numerical models. *Mon. Wea. Rev.*, **117**, 340–350.

Waller, J. A., D. Simonin, S. L. Dance, N. K. Nichols, and S. P. Ballard, 2016: Diagnosing observation error correlations for Doppler radar radial winds in the Met Office UKV model using observation-minus- background and observation-minus-analysis statistics. *Mon. Wea. Rev.*, **144**, 3533–3551.

Wang, J., and W. B. Rossow, 1995: Determination of cloud vertical structure from upper-air observations. *J. Appl. Meteor.*, **34**, 2243–2258.

Watts, P. D., R. Bennartz, and F. Fell, 2011: Retrieval of two-layer cloud properties from multispectral observations using optimal estimation. *J. Geophys. Res.*, **116**, D16203, doi:10.1029/2011JD015883.

Weissmann, M., K. Folger, and H. Lange, 2013: Height correction of atmospheric motion vectors using airborne lidar observations. *J. Appl. Meteor. Climatol.*, **52**, 1868–1877.

WMO, 2010: Guide to the Global Observing System. WMO-No. 488, WMO, Geneva, Switzerland, 215 pp. [Available at https://library.wmo.int/doc_num.php?explnum_id=4236.]

WMO, 2011: Manual on Codes - International Codes, Volume I.1, Annex II to the WMO Technical Regulations: Part A- Alphanumeric Codes. WMO-No. 306, WMO, Geneva, Switzerland, 454 pp. [Available at https://library.wmo.int/doc_num.php?explnum_id=10235.]

WMO, 2017: International Cloud Atlas: Manual on the Observation of Clouds and Other Meteors. 2017 edition. WMO, Geneva, Switzerland. [Available at https://cloudatlas.wmo.int/en/home.html.]

WMO, 2019: General Meteorological Standards and Recommended Practices. Technical regulations, basic documents No. 2, Volume I. 2019 edition. WMO-No. 49, WMO, Geneva, Switzerland, 48pp. [Available at https://library.wmo.int/ doc_num.php?explnum_id=10113.]

Wu, T.-C., H. Liu, S. J. Majumdar, C. S. Velden, and J. L. Anderson, 2014: Influence of assimilating satellite-derived atmospheric motion vector observations on numerical analyses and forecasts of tropical cyclone track and intensity. *Mon. Wea. Rev.*, **142**, 49–71.

Wu, T.-C., C. S. Velden, S. J. Majumdar, H. Liu, and J. L. Anderson, 2015: Understanding the influence of assimilating subsets of enhanced atmospheric motion vectors on numerical analyses and forecasts of tropical cyclone track and intensity with an ensemble Kalman filter. *Mon. Wea. Rev.*, **143**, 2506–2531.

Yamashita, K., 2010: Observing system experiments of MTSAT-2 rapid scan atmospheric motion vector for T-PARC 2008 using the JMA operational NWP system. *Proc. 10th International Winds Workshop*, Tokyo, Japan. [Available at https://www-cdn.eumetsat.int/files/2020-04/pdf_conf_p56_s6_06_yamashit _v .pdf.]

Yamashita, K., 2012: An observing system experiment of MTSAT-2 rapid scan AMV using JMA meso-scale operational NWP system. *Proc. 11th International Winds Workshop*, Auckland, New Zealand. [Available at https://www-cdn.eumetsat.int/files/2020-04/pdf_conf_p60_s4_15_yamashit_v.pdf.]

Yamashita, K., 2016: Assimilation of Himawari-8 atmospheric motion vectors into the numerical weather prediction systems of Japan Meteorological Agency. *Proc. 13th International Winds Workshop*, Monterey, USA. [Available at http://cimss.ssec.wisc.edu/iwwg/ iww13/proceedings_iww13/index.html.]

Yang, J., Z. Zhang, C. Wei, F. Lu, and Q. Guo, 2017: Introducing the new generation of Chinese geostationary weather satellites, Fengyun-4. *Bull. Amer. Meteor. Soc.*, **98**, 1637–1658.

Yoden, S. 2007: Atmospheric predictability. *J. Meteor. Soc. Japan,* **85B**, 77–102.

Young, A. H., J. J. Bates, and J. A. Curry, 2013: Application of cloud vertical structure from CloudSat to investigate MODIS-derived cloud properties of cirriform, anvil, and deep convective clouds. *J. Geophys. Res.*, **118**, 4689–4699.

Zapotocny, T. H., J. A. Jung, J. F. L. Marshall, and R. E. Treadon, 2008: A two-season impact study of four satellite data types and rawinsonde data in the NCEP global data assimilation system. *Wea. Forecasting*, **23**, 80–100.

Zhang, J., H. Chen, Z. Li, X. Fan, L. Peng, Y. Yu, and M. Cribb, 2010: Analysis of cloud layer structure in Shouxian, China using RS92 radiosonde aided by 95 GHz cloud radar. *J. Geophys. Res.*, **115**, D00K30, doi:10.1029/2010JD014030.

Figures

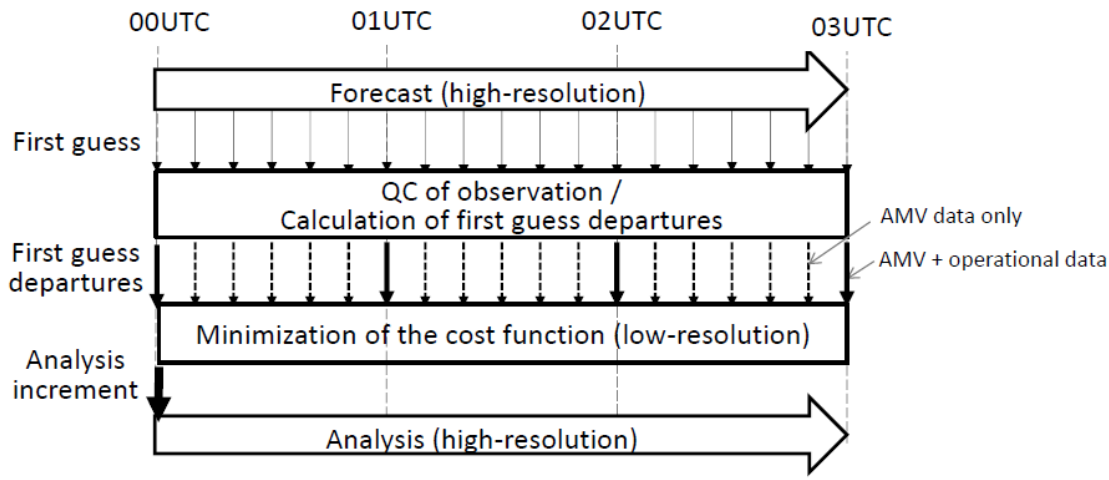

Figure 2.1. Schematic diagram of one analysis cycle. Here, the 0300 UTC analysis is shown as an example. RS-AMVs are assimilated every 10 min, and other observations are assimilated hourly.

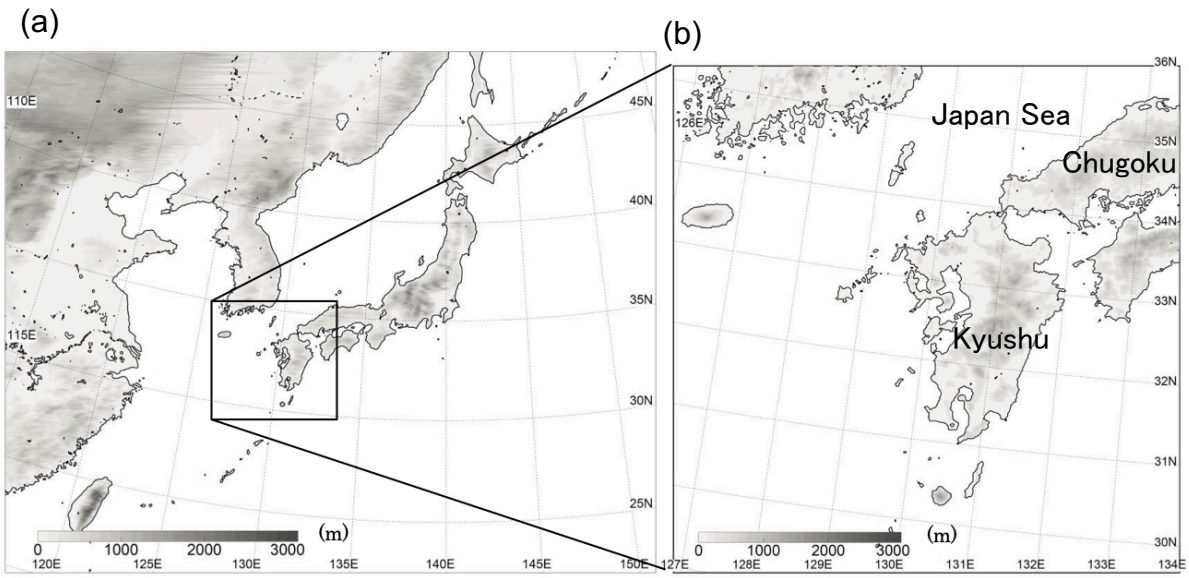

Figure. 2.2. (a) The JNoVA and (b) NHM forecast domains. The JNoVA domain has a 5-km horizontal resolution, and the NHM forecast has a 2-km resolution. Topography (meters above sea level) is indicated by shading.

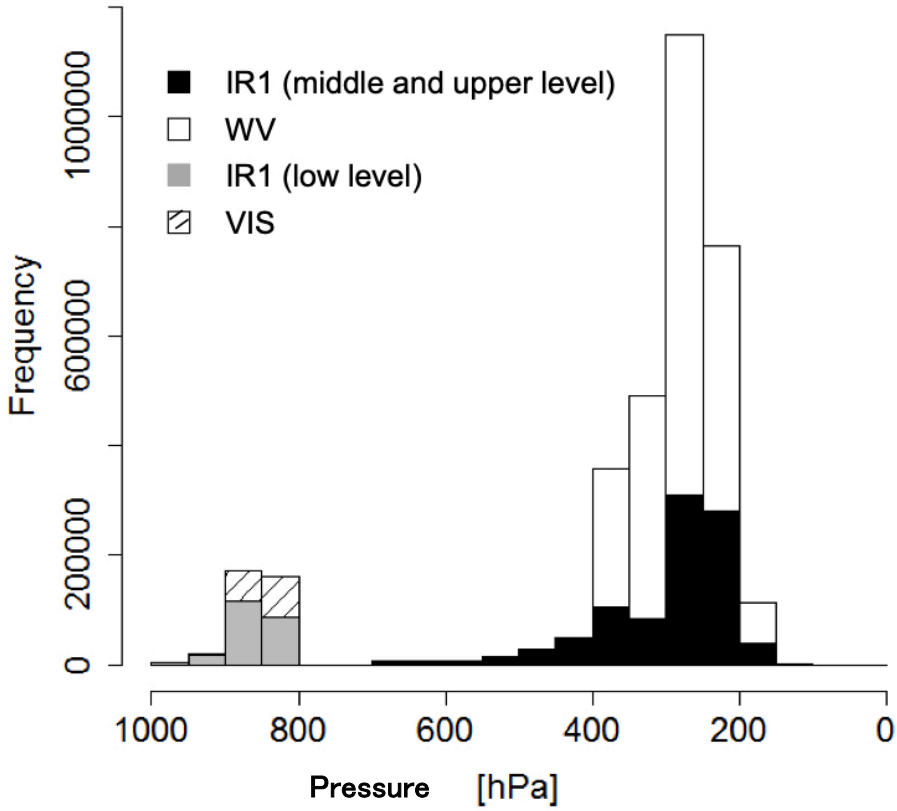

Figure 2.3. Distributions of observations according to pressure level. Black, white, and gray bars show the number of IR1 middle- and upper-level (≤700 hPa) wind observations, WV wind observations, and IR1 lower-level (>700 hPa) wind observations, respectively. Hatched bars show the number of VIS wind observations.

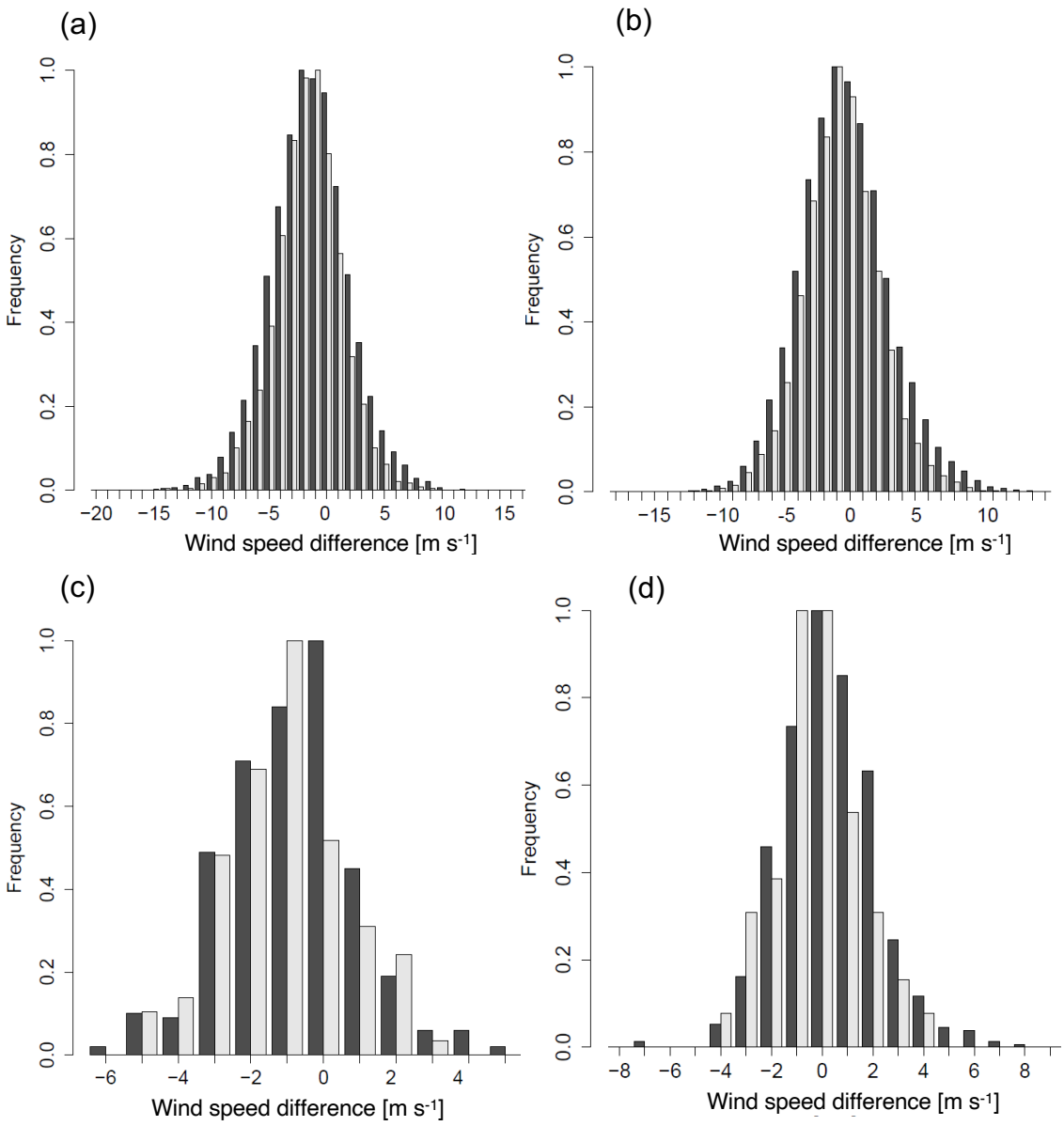

Figure 2.4. Distributions of wind speed (m s^{-1}) differences between AMVs and NHM forecast winds: (a) IR1 middle- and upper-level winds, (b) WV winds, (c) IR1 lower-level winds, and (d) VIS lower-level winds. Dark gray bars represent RS-AMVs, and light gray bars represent RTN-AMVs. Bin widths are 1.0 m s^{-1}. The frequencies are normalized by setting the maximum value to 1.0.

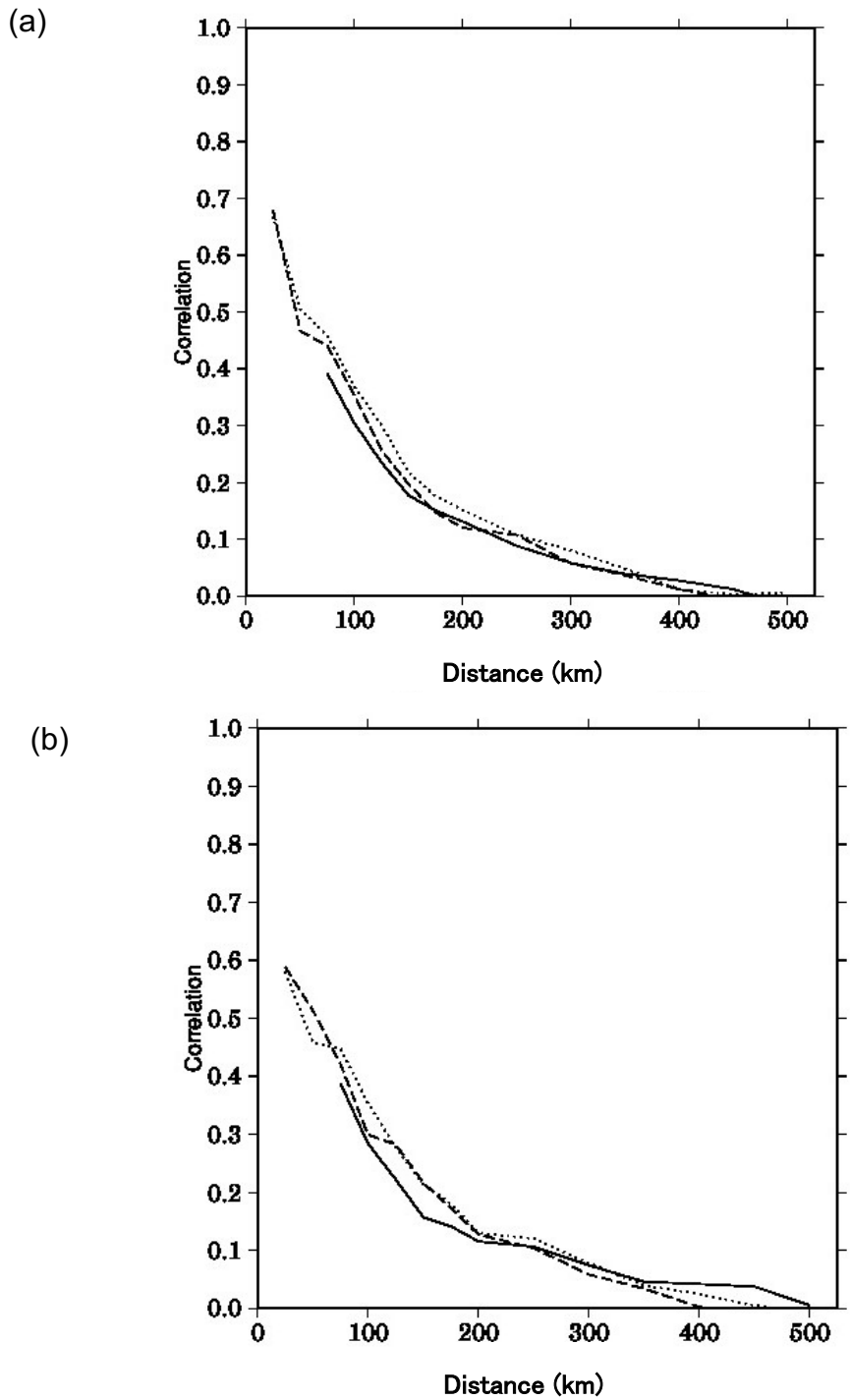

Figure 2.5. Estimated spatial observation-error correlations as a function of the spatial distance between pairs of RS-AMVs. The (a) zonal and (b) meridional components of upper-level (dotted lines), middle-level (dashed lines), and lower-level (solid lines) winds are shown.

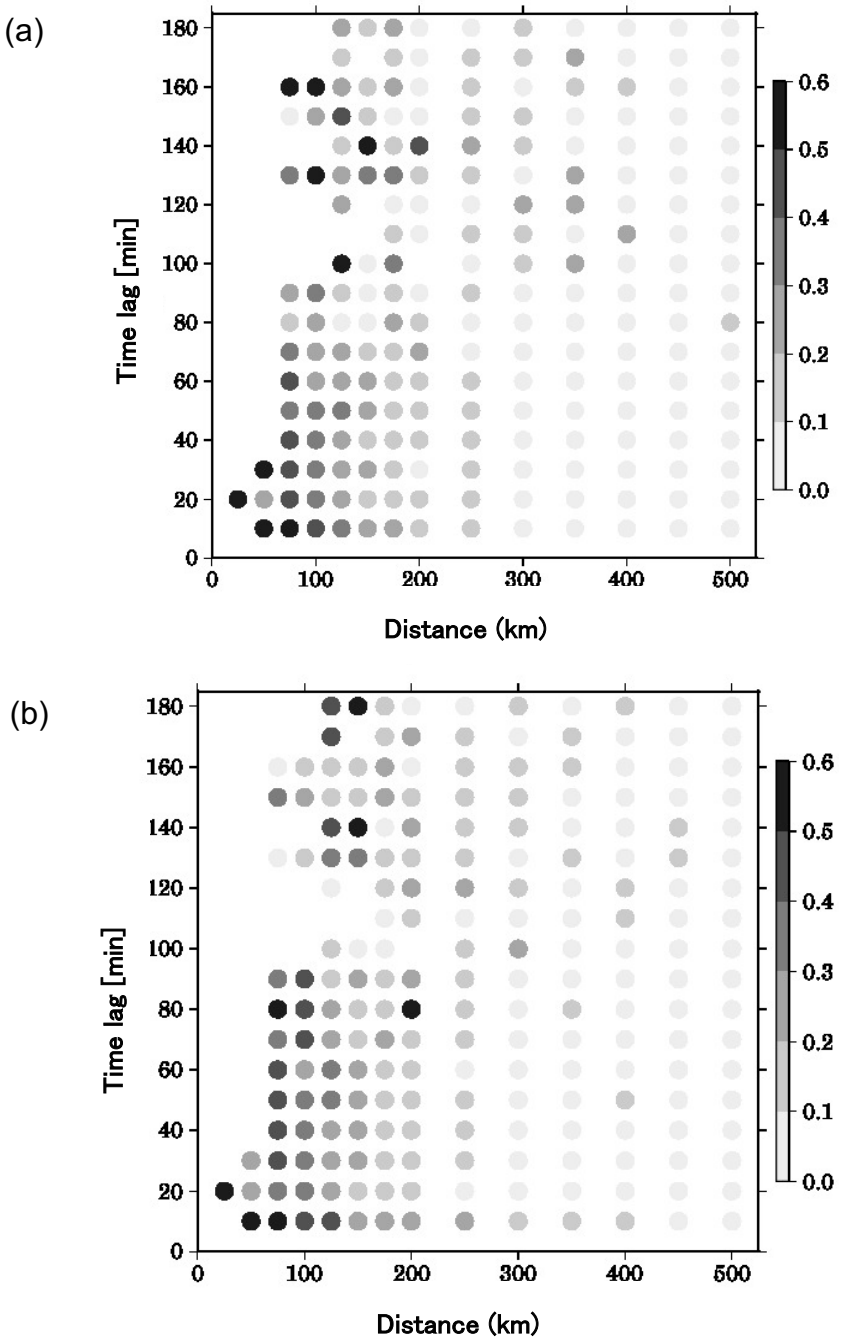

Figure 2.6. Estimated observation-error correlations (shade in circles) as a function of both the spatial and temporal separation of pairs of RS-AMVs. (a) Zonal and (b) meridional wind components.

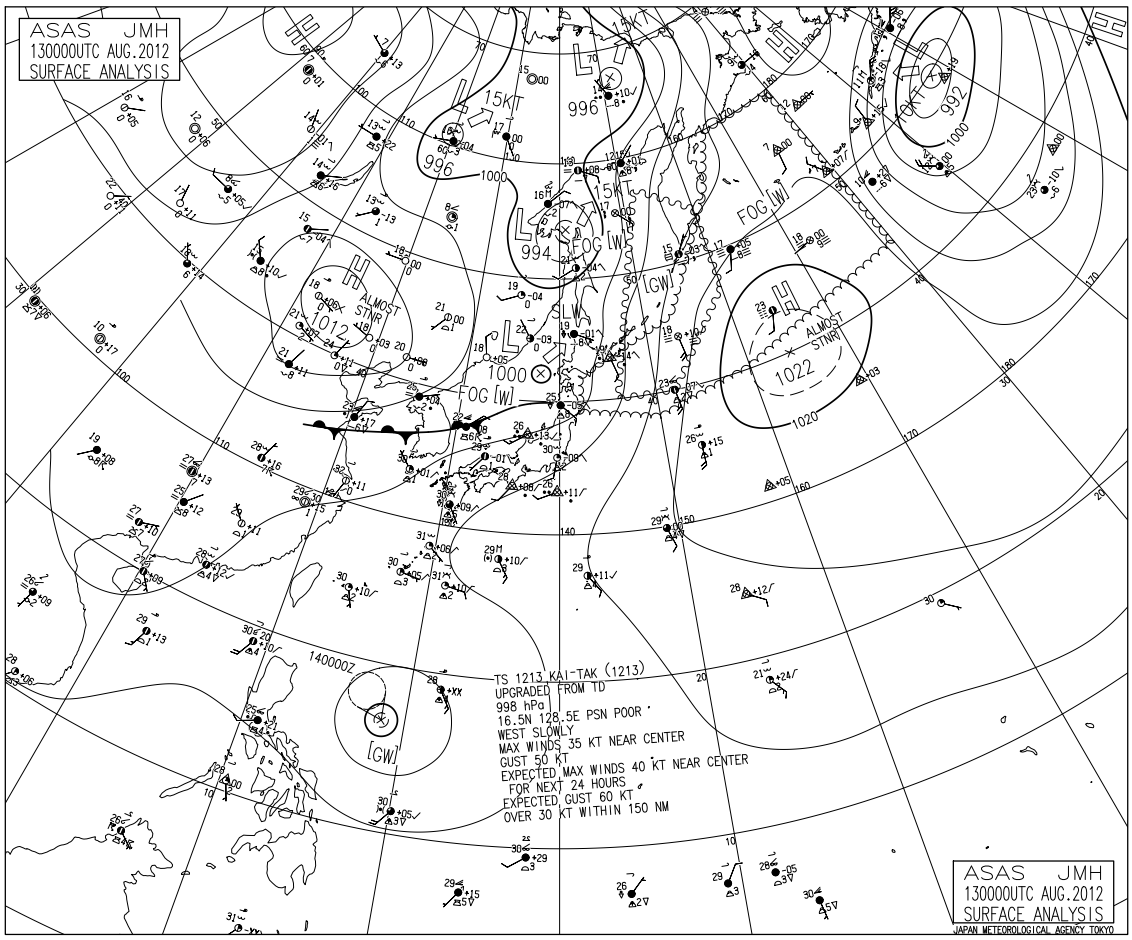

Figure 2.7. JMA produced surface weather analysis at 0000 UTC on 13 August 2012.

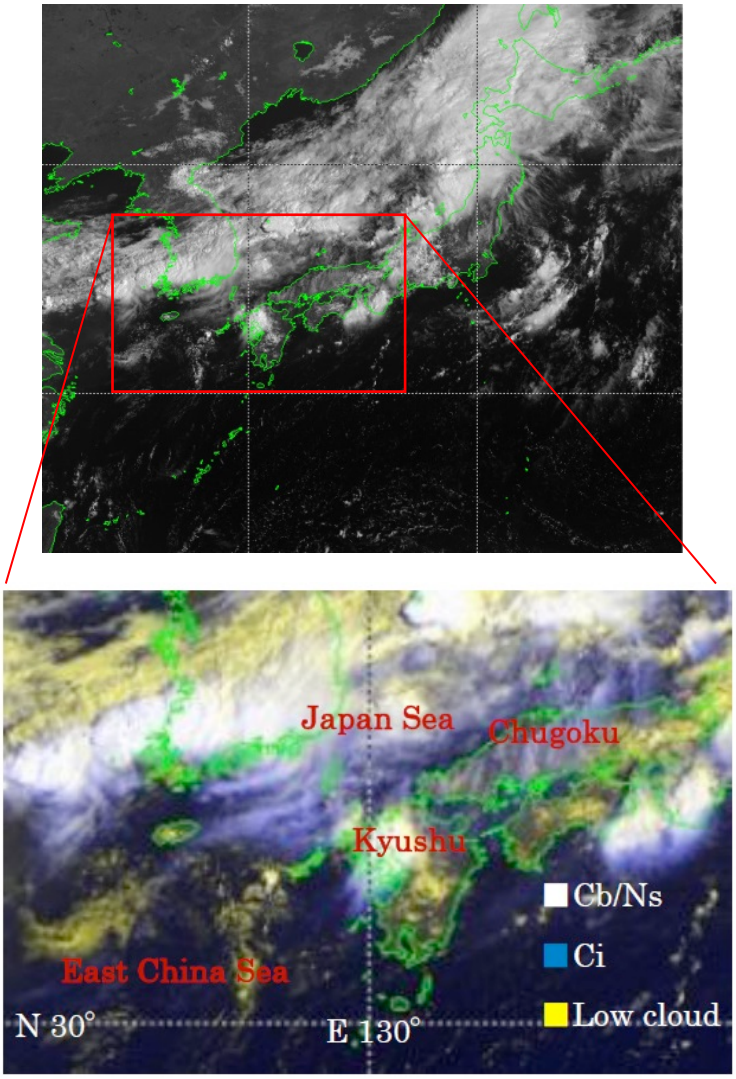

Figure 2.8. IR and VIS combined images obtained by MTSAT-1R at 0005 UTC on 13 August 2012. In the bottom panel, yellow color represents low clouds, white represents thick and high clouds such as cumulonimbus and nimbus clouds, and blue represents cirrus clouds.

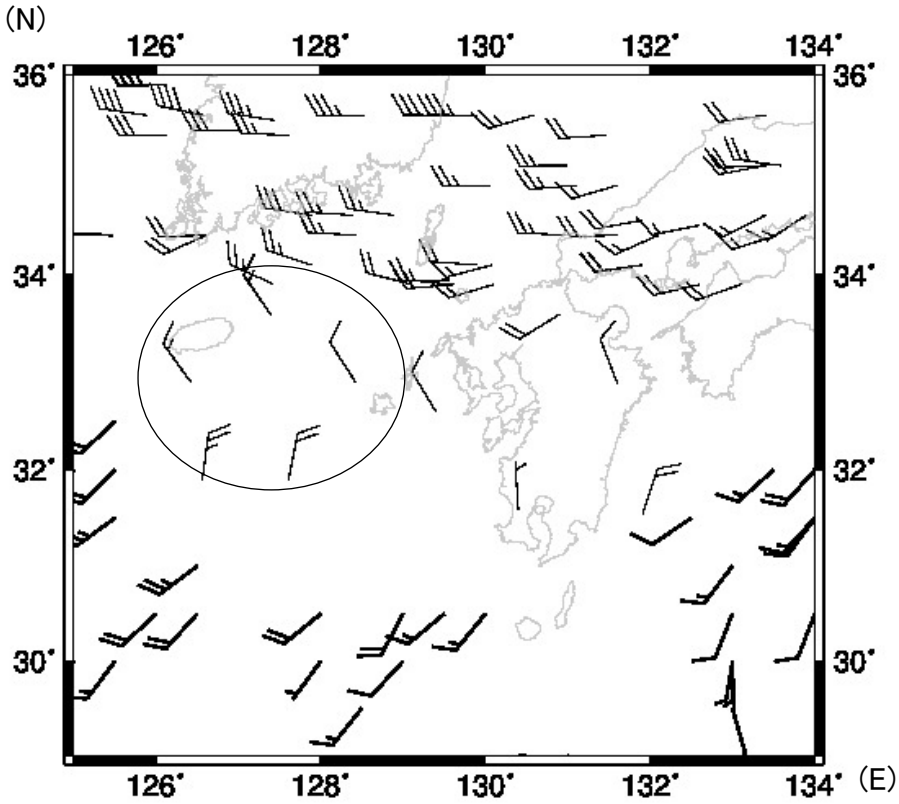

Figure 2.9. The spatial distribution of assimilated RS-AMVs during the period of 0000–0900 UTC on 13 August 2012 in the forecast domain. Thin barbs represent upper-level winds, and thick barbs represent lower-level winds. The area of divergent upper-level flows is circled.

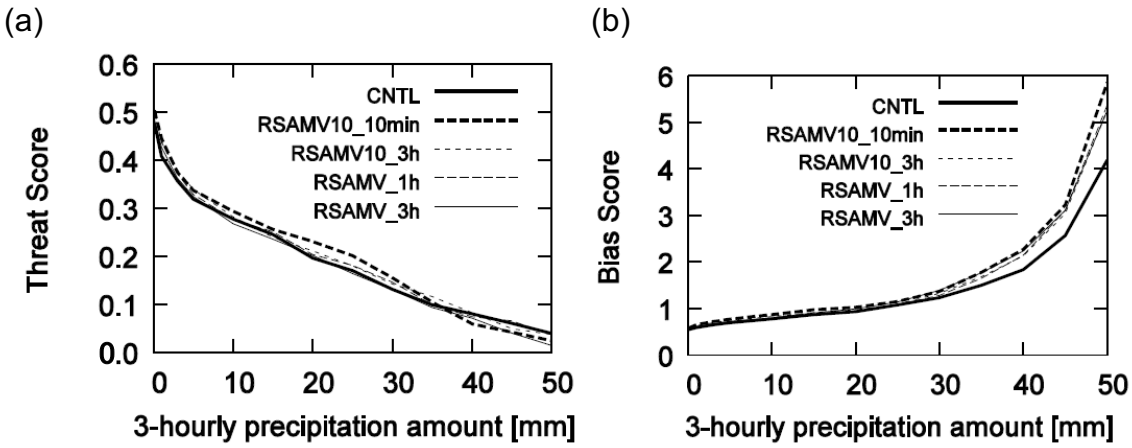

Figure 2.10. Forecast scores for 3-hourly precipitation amounts averaged over the whole forecast period of the assimilation experiments (see Table 2.2). (a) Threat scores; (b) bias scores.

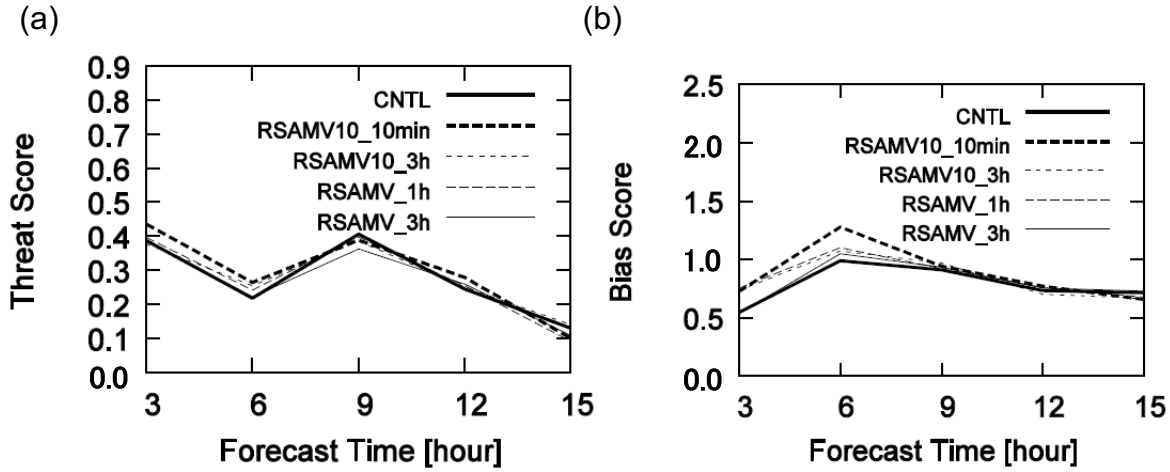

Figure 2.11. Precipitation forecast scores for the precipitation threshold of 10 mm in three hours in the assimilation experiments. (a) Threat scores; (b) bias scores.

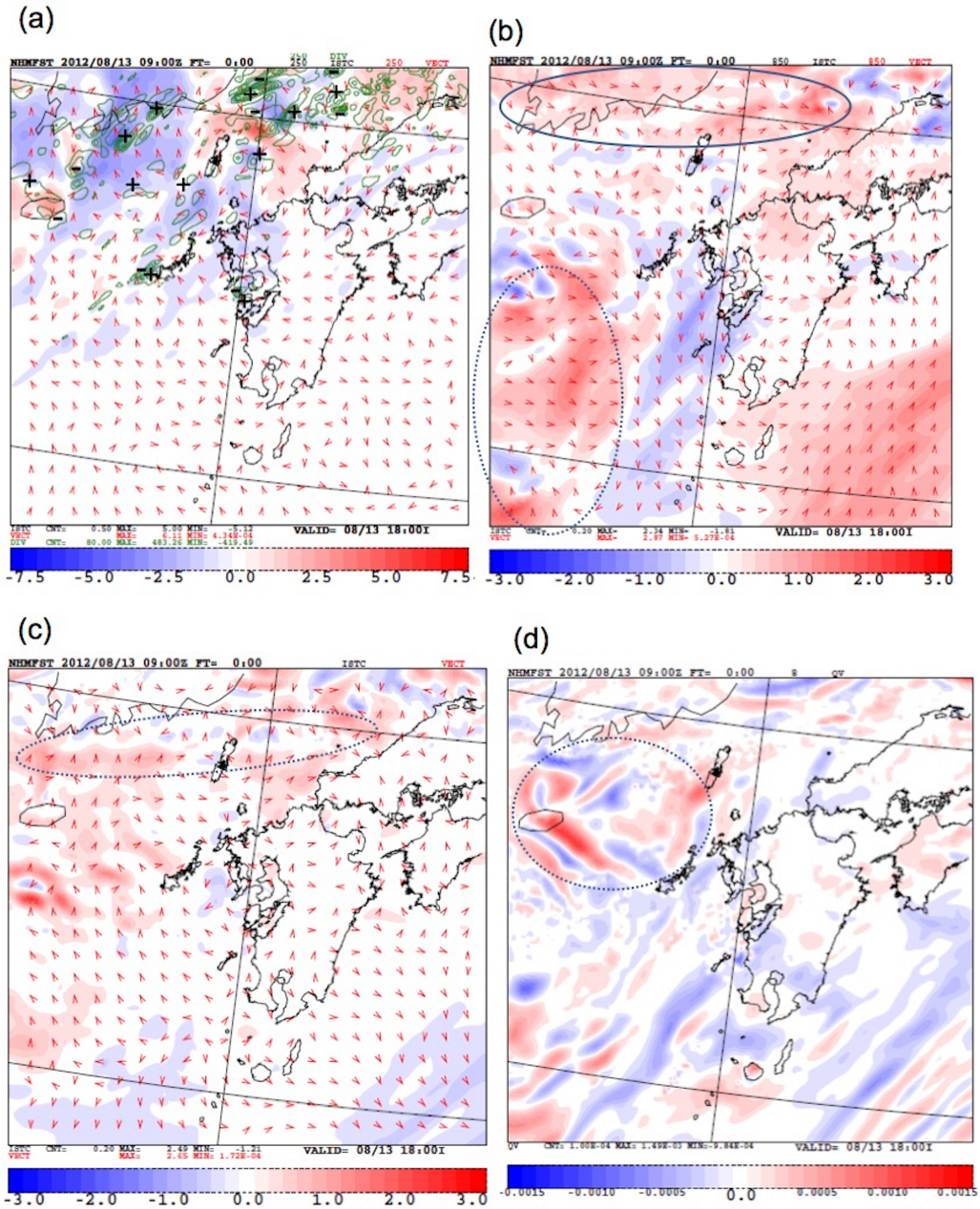

Figure 2.12. Differences in the analysis results between TEST and CNTL (TEST minus CNTL). Wind difference fields at (a) 250 hPa (green contours show areas of divergence using a 8.0×10^{-5} s^{-1} interval; plus and minus signs indicate increased and decreased divergence, respectively); (b) 850 hPa; and (c) the surface. In (a), (b), and (c), the color scale shows wind speed difference (m s^{-1}), and the arrows show wind direction difference. (d) The water vapor mixing ratio difference at 500 m above the surface (kg kg^{-1}).

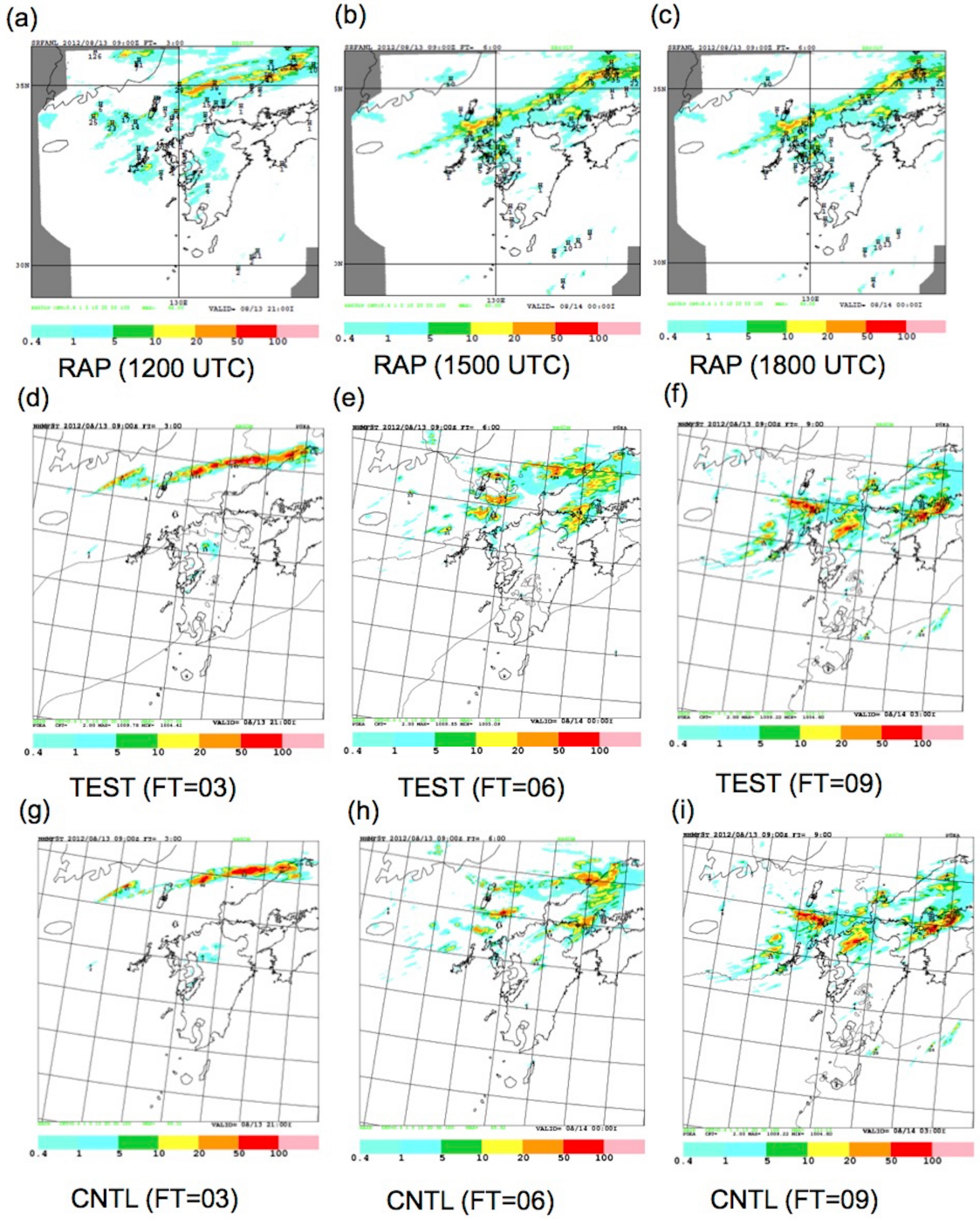

Figure 2.13. Hourly precipitation (mm) in observations and NHM forecasts. (a), (b), and (c) Radar/rain gauge-analyzed precipitation (RAP); (d), (e), and (f) forecasts by TEST; (g), (h), and (i) forecasts by CNTL. (a), (d), and (g) Forecast time (FT) = 03 (1200 UTC); (b), (e), and (h) FT = 06 (1500 UTC); (c), (f), and (i) FT = 09 (1800 UTC).

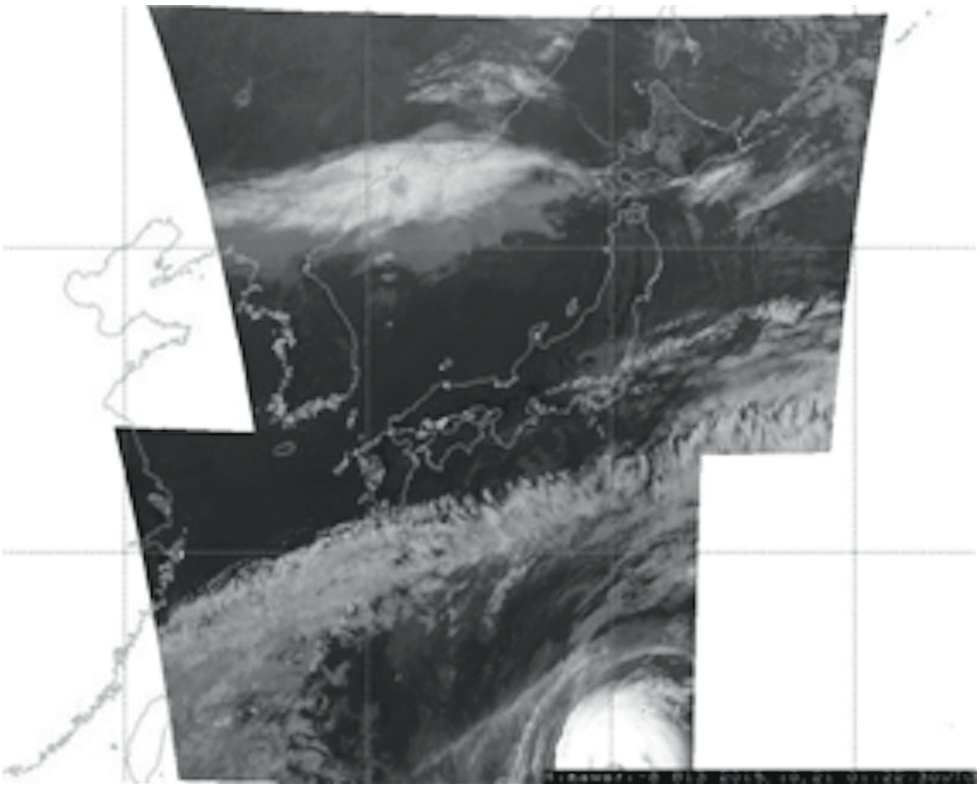

Figure 3.1. 2.5-min rapid scan area around Japan by Himawari-8.

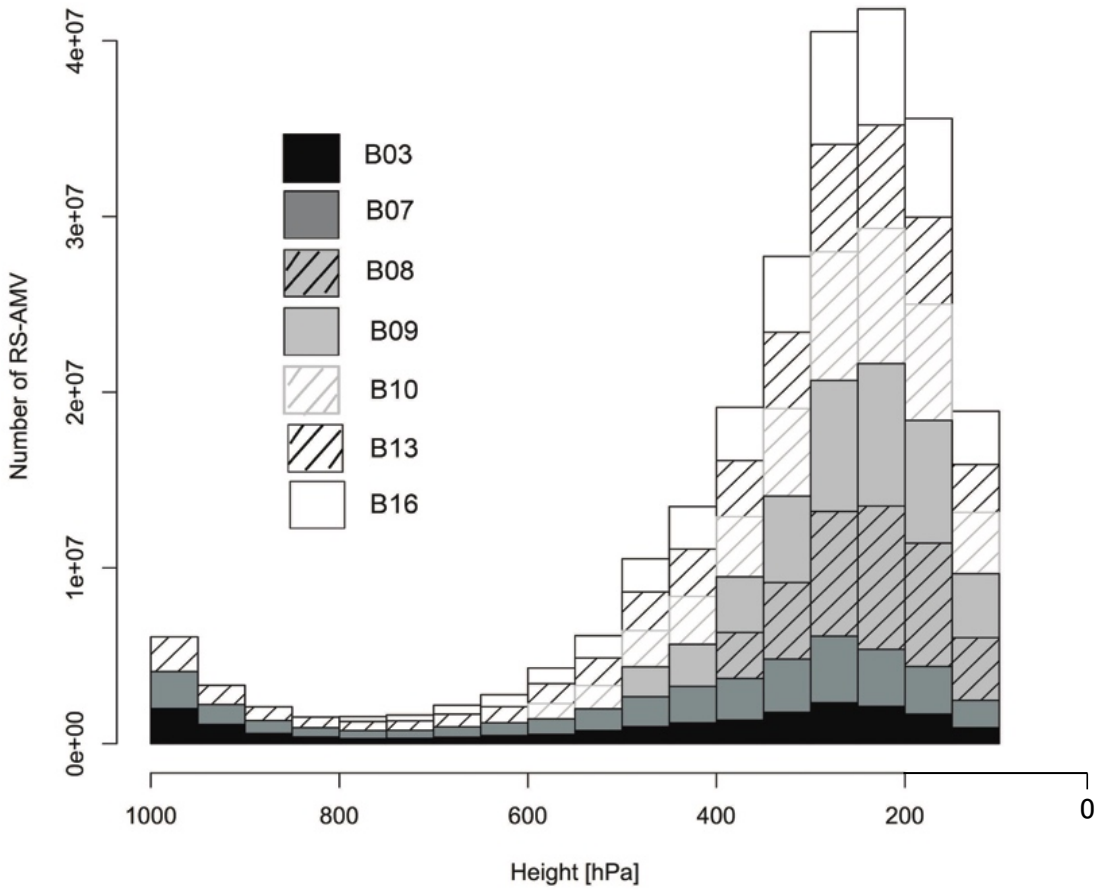

Figure 3.2. Distributions of RS-AMVs according to pressure level in June 2016. Black, dark gray, gray hatched with black lines, gray, white hatched with light gray lines, white hatched with black lines, and white bars show the number of B03, B07, B08, B09, B10, B13, and B16 observations, respectively.

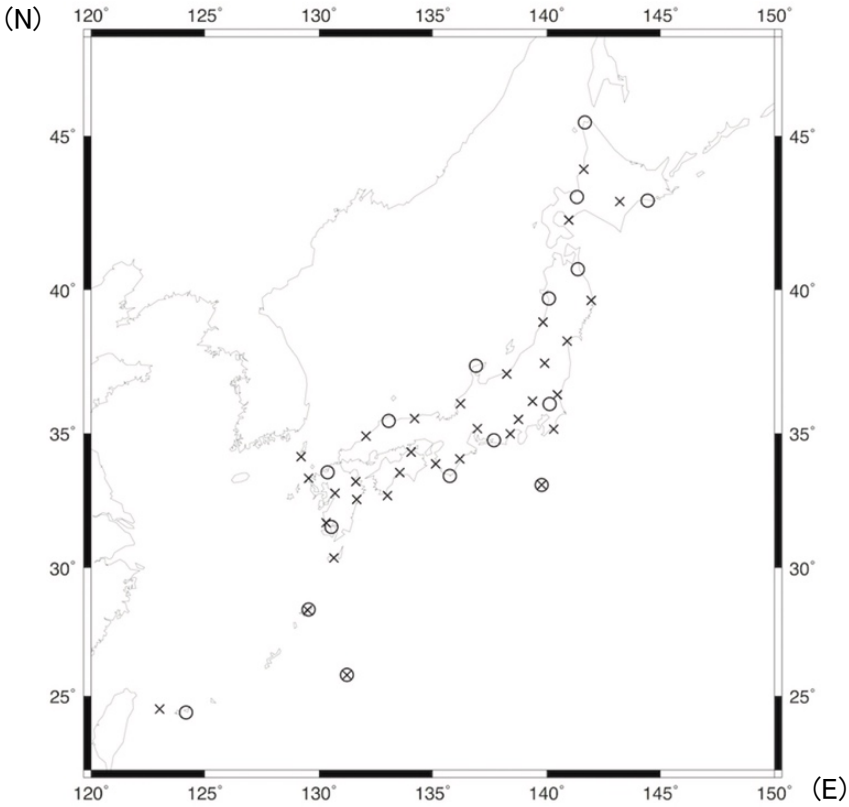

Figure 3.3. Upper-air observation stations of the JMA used for the comparison with RS-AMVs. Circles and crosses represent sonde and WPR stations, respectively.

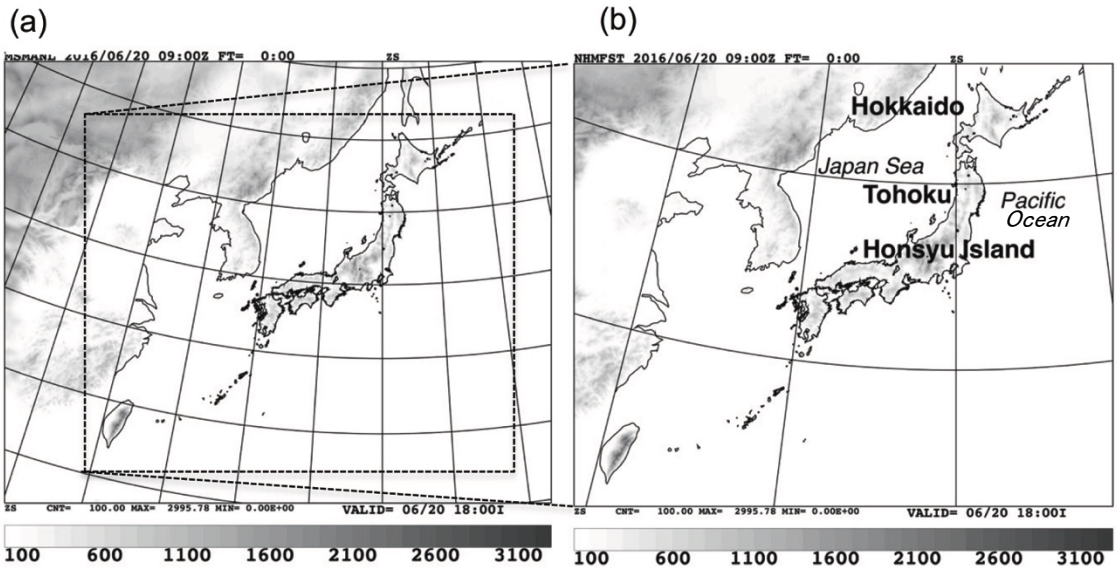

Figure 3.4. (a) The JNoVA and (b) NHM forecast domains. Topography (meters above sea level) is indicated by shading.

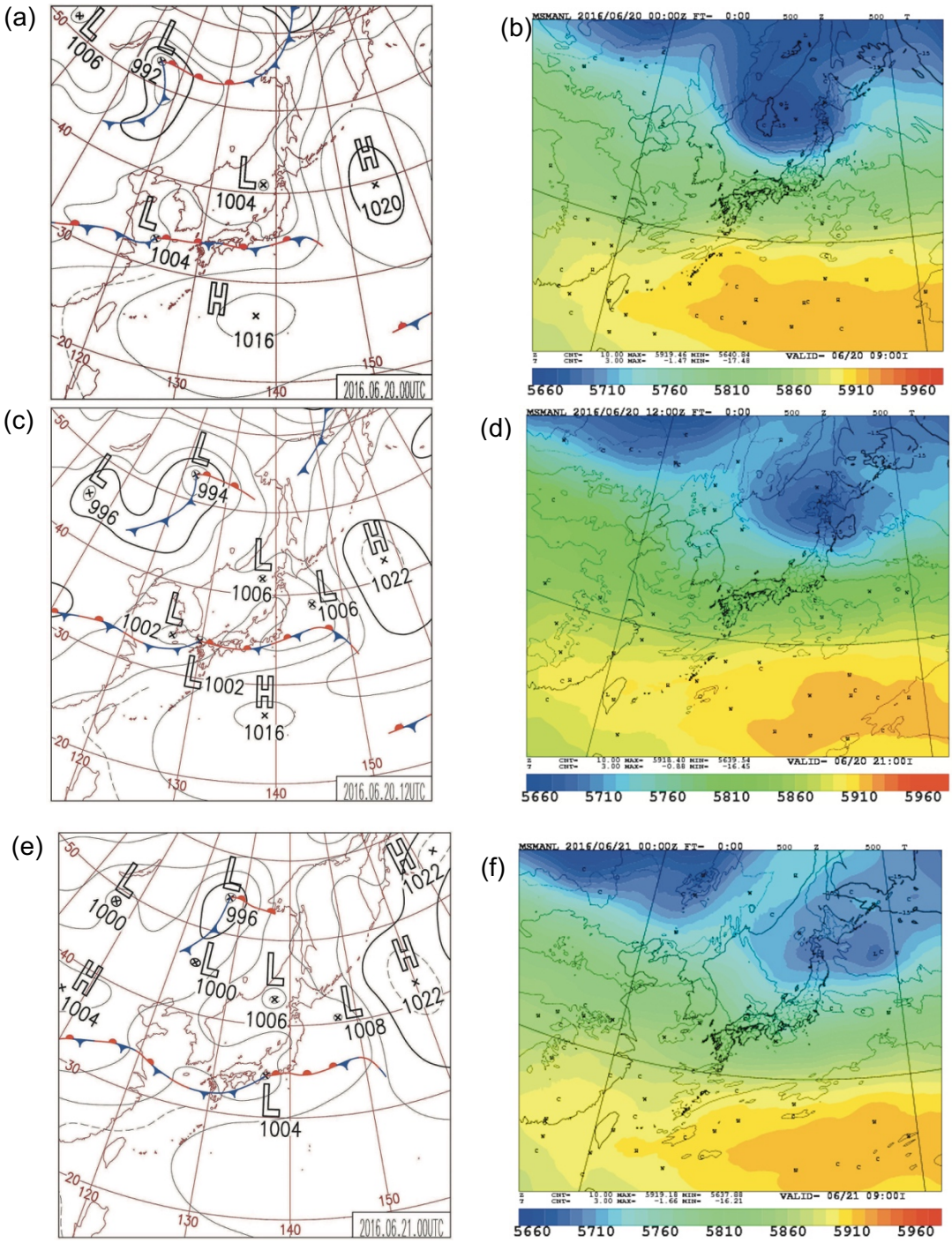

Figure 3.5. JMA produced weather analysis at (a) 0000 UTC, (c) 1200 UTC on 20, and (e) 0000 UTC on 21 June 2016 for the surface. Geopotential heights in meters (color shades) and contours of temperatures in degrees Celsius using a contour interval of 3.0 degrees at 500 hPa height obtained from JMA's meso analyses at (b) 0000 UTC, (d) 1200 UTC on 20, and (f) 0000 UTC on 21 June 2016.

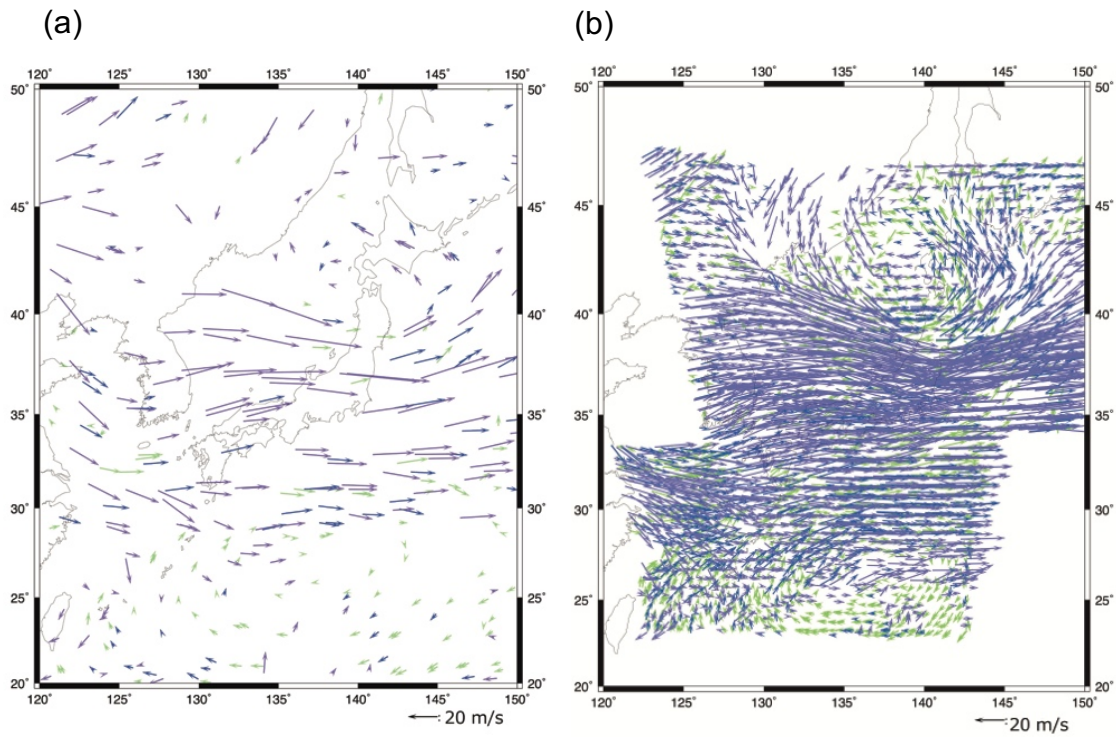

Figure 3.6. The spatial distribution of assimilated RS-AMVs during the period 0600–0900 UTC on 20 June 2016 around Japan. Purple, blue, and green arrows represent high-, mid-, and low-level winds, respectively. (a) CNTL with RTN-AMVs, (b) ALL with RS-AMVs, (c) CNTL0.5 with RTN-AMVs thinned to 0.5 deg., (d) ALL1.0 with RS-AMVs thinned to 1.0 deg., and ALL minus first guess for (e) low-level winds and (f) mid- and high-level winds.

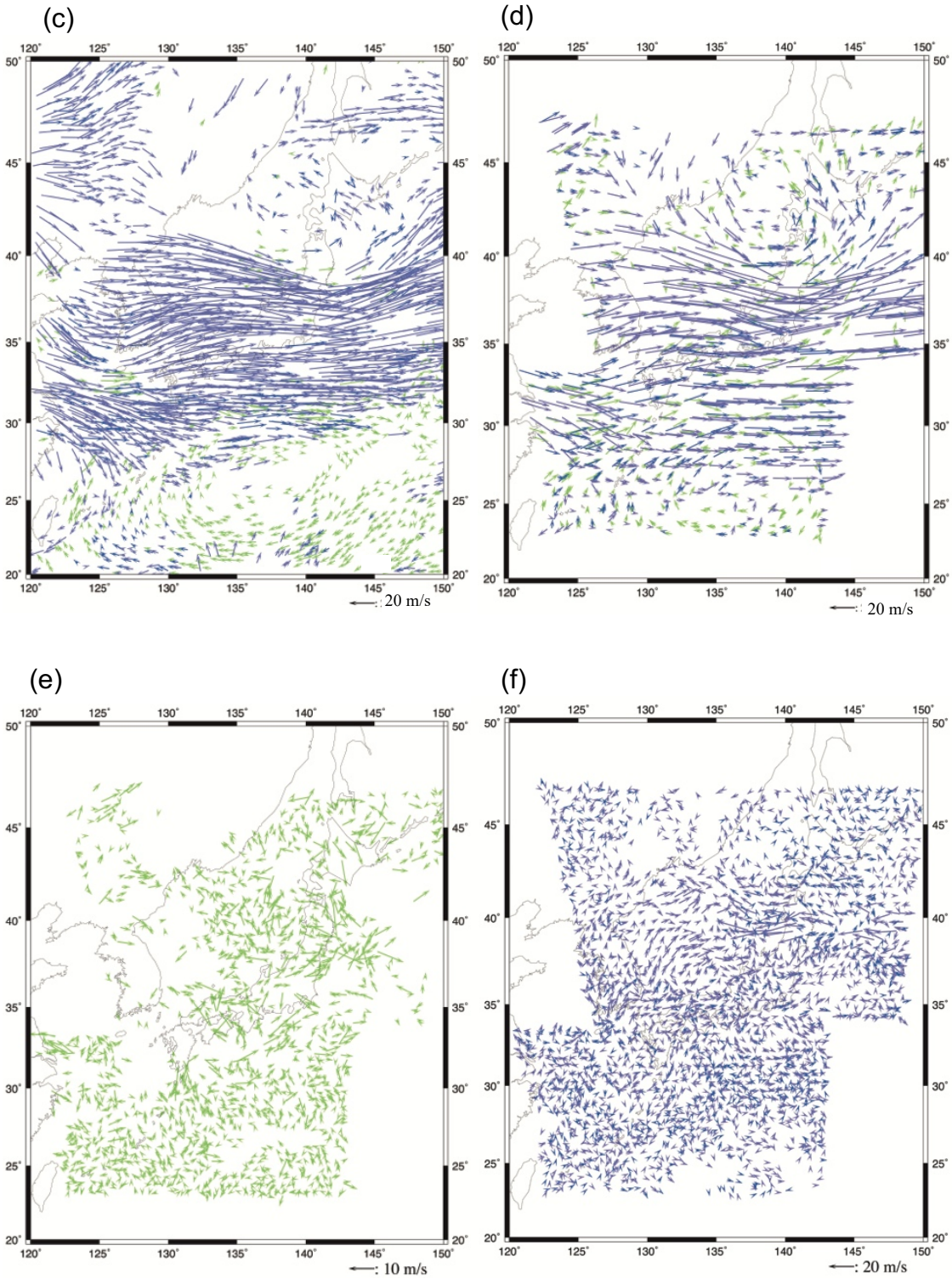

Figure 3.6. Continued.

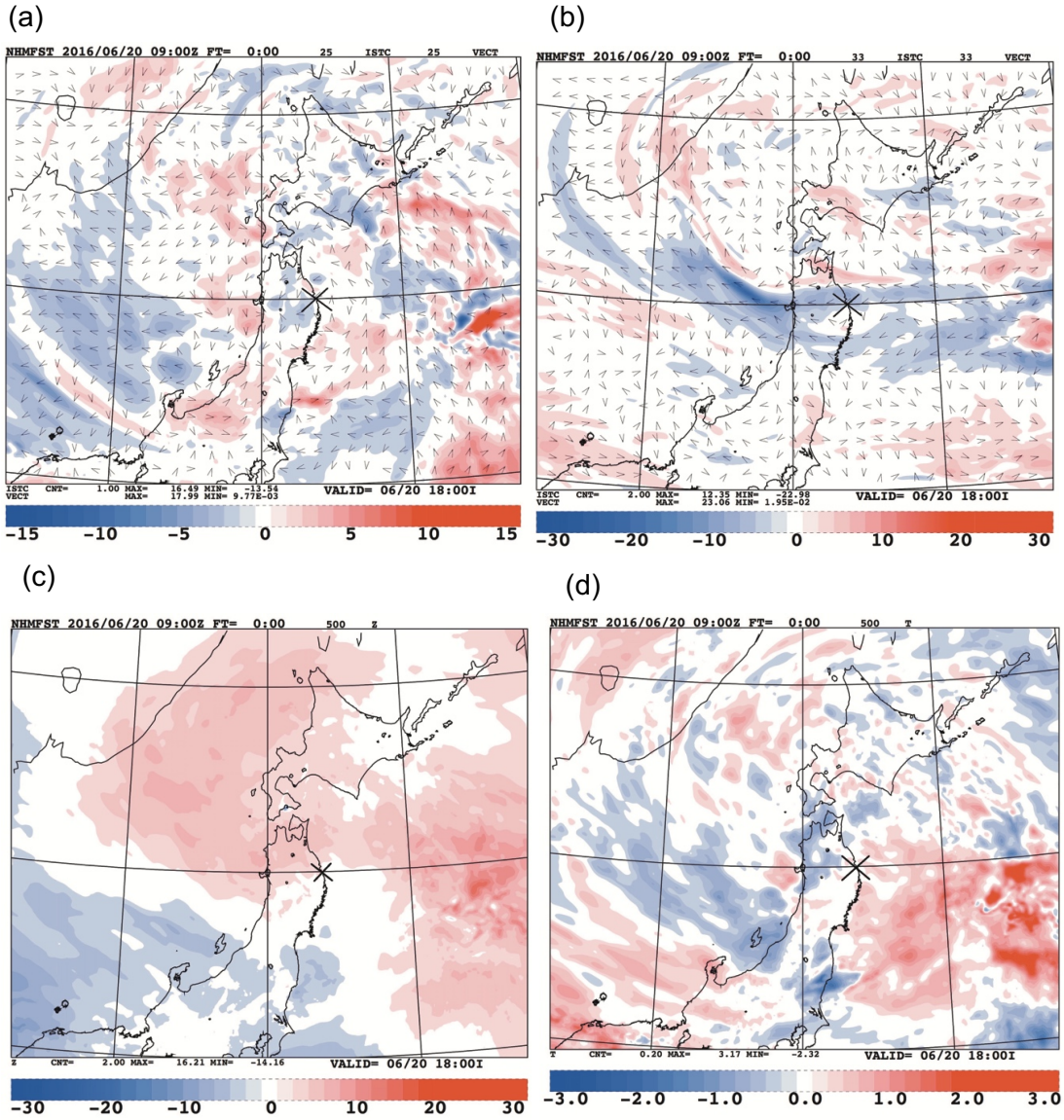

Figure 3.7. Differences in the analysis results between ALL and CNTL (ALL minus CNTL) at 0900 UTC on 20 June 2016 after the four assimilation cycles. (a) Wind vectors and wind speeds at 500 hPa, (b) wind vectors and wind speeds at 300 hPa, (c) geopotential heights at 500 hPa, and (d) temperatures at 500 hPa. Arrows represent wind direction in (a) and (b). Color shades represent wind speed (m s^{-1}) in (a) and (b), geopotential heights in (c), and temperatures in (d). A cross in each figure indicates the position of the center of the cold vortex.

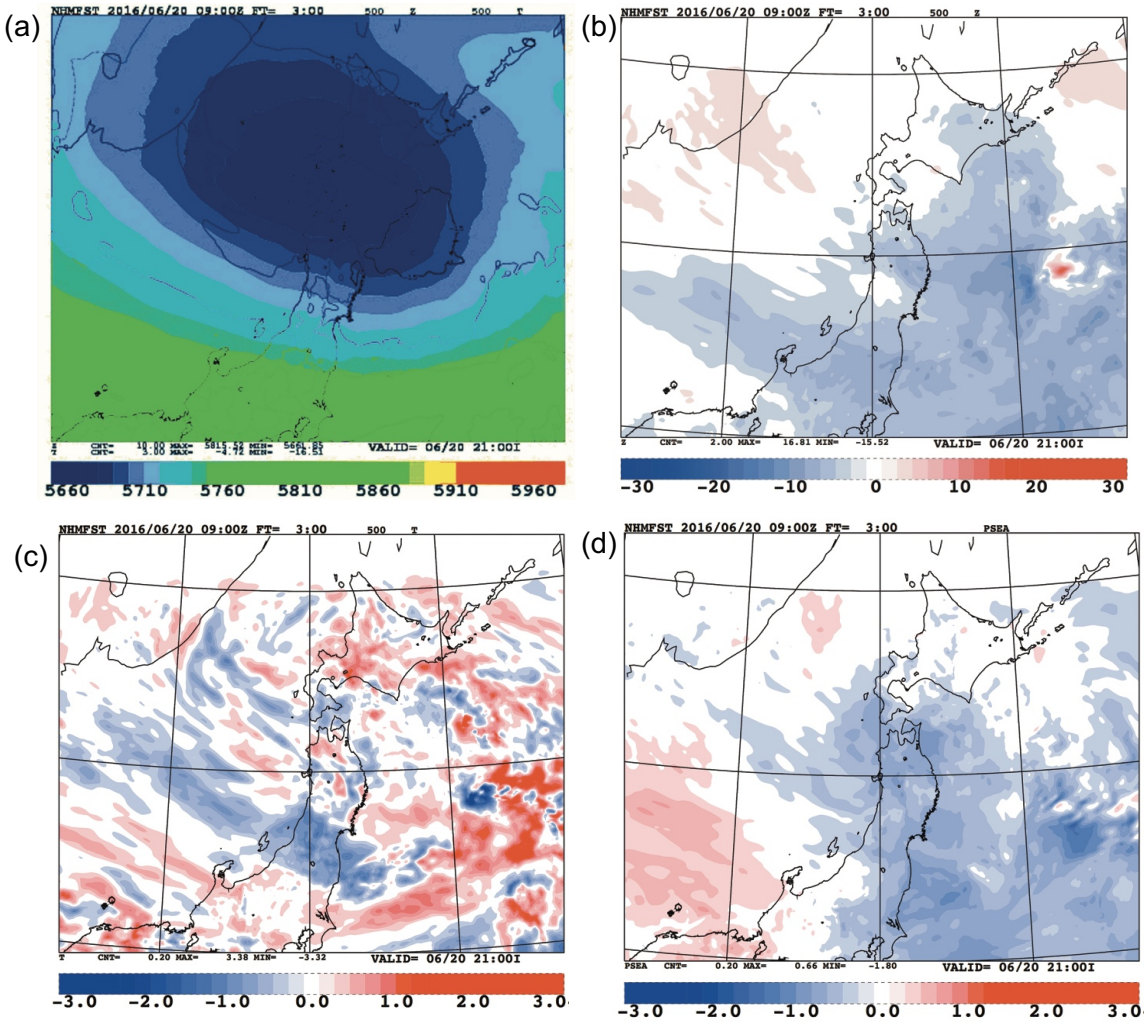

Figure 3.8. Forecast results in ALL and CNTL. (a) Geopotential heights (color shades) and temperatures (contour lines) at 500 hPa in ALL, differences between ALL and CNTL (ALL minus CNTL) in (b) geopotential heights and (c) temperatures at 500 hPa, and (d) surface pressure (hPa) at 1200 UTC on 20 June 2016 (FT03). (e) Geopotential heights (color shades) and temperatures (contour lines) at 500 hPa in ALL and (f) differences between ALL and CNTL in geopotential heights at 500 hPa at 0000 UTC on 21 June 2016 (FT15). Color shades represent differences of geopotential heights in (b) and (f), temperatures in (c), and surface pressures in (d).

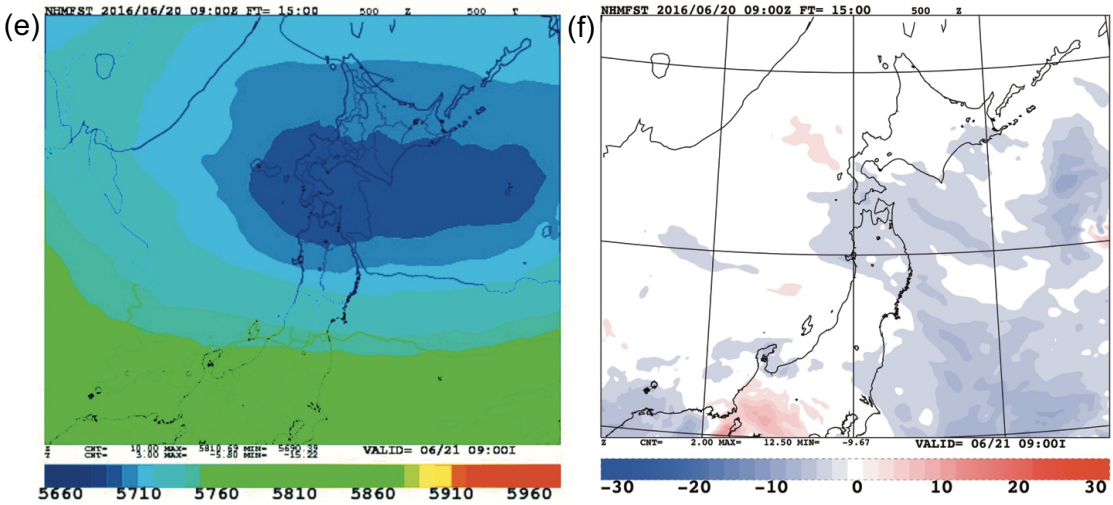

Figure 3.8. Continued.

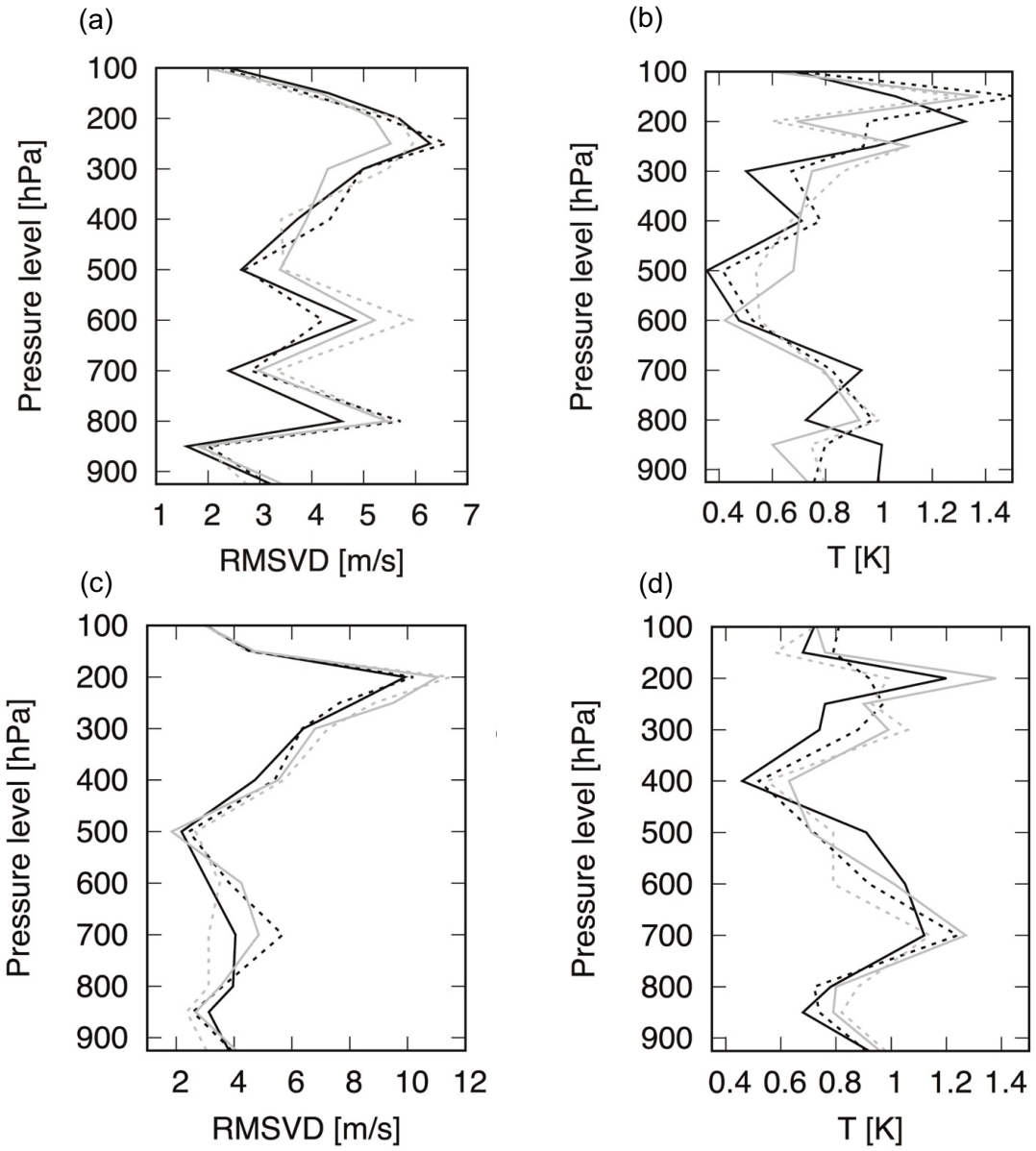

Figure 3.9. Forecast winds and temperatures in northern Japan validated against sonde observations. The two upper panels (a, b) at FT03, the bottom panels (c, d) at FT15. RMSVD profiles (a, c) and RMSE profiles for temperature (b, d). The black solid line represents ALL, and the dashed line represents CNTL. The gray line indicates ALL1.0 with 1.0° data thinning, while the gray dashed line indicates CNTL0.5 with 0.5° thinning scale.

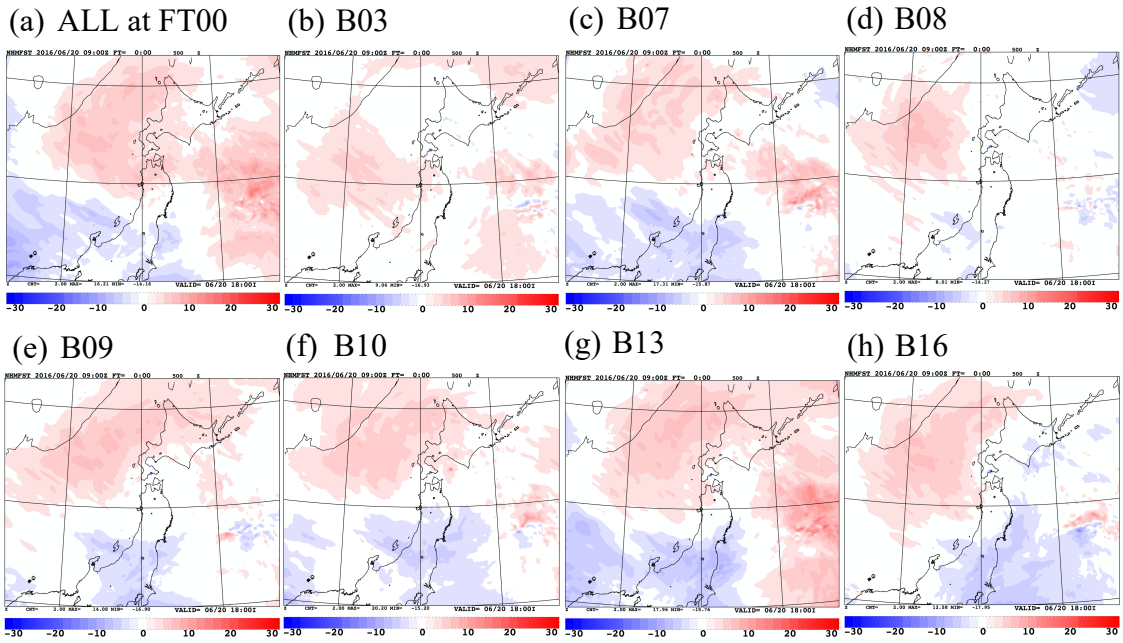

Figure 3.10. Differences in the analysis and forecast results of geopotential heights at 500 hPa from CNTL. Analysis differences in (a) ALL and (b) B03, (c)B07, (d) B08, (e) B09, (f) B10, (g) B13, and (h) B16. Forecast differences at 1200 UTC 20 June 2016 (FT03) in (i) ALL and (j) B03, (k) B07, (l) B08, (m) B09, (n) B10, (o) B13, and (p) B16. Forecast differences at 0000 UTC 21 June 2016 (FT15) in (q) ALL and (r) B03, (s) B07, (t) B08, (u) B09, (v) B10, (w) B13, and (x) B16.

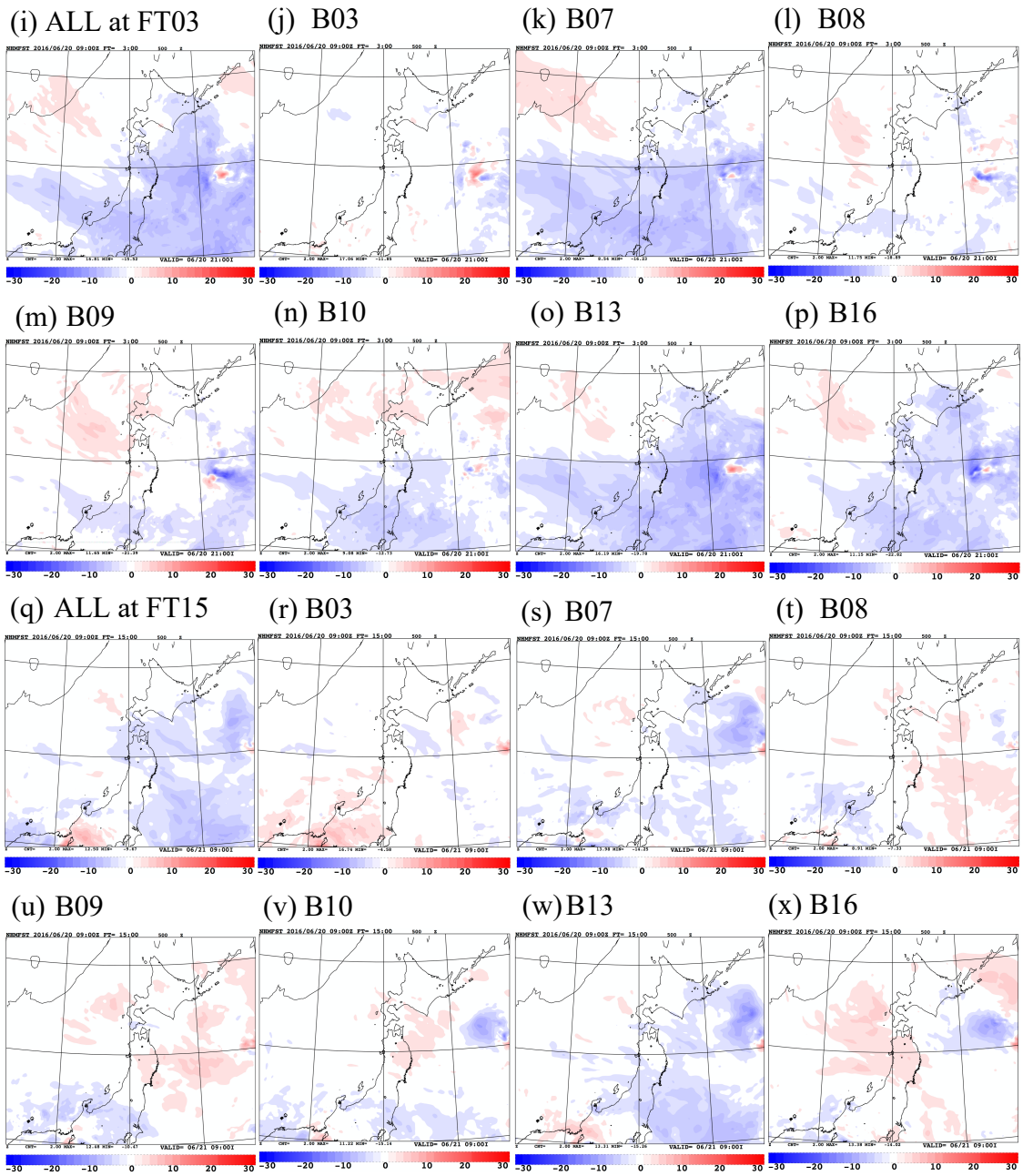

Figure 3.10. Continued.

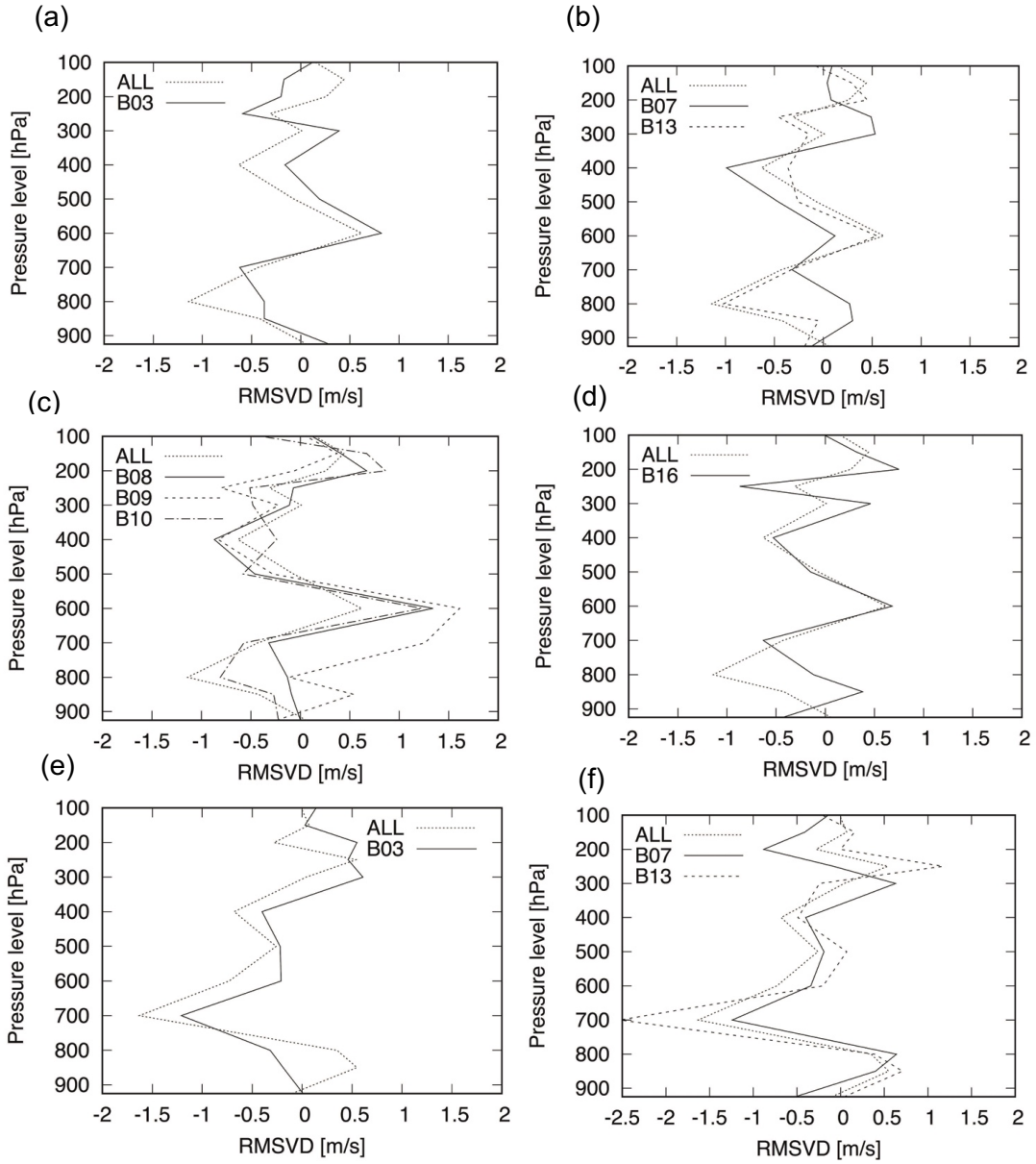

Figure 3.11. Forecast winds in northern Japan validated against sonde observations. Profiles of RMSVD differences from CNTL for the (a) VIS, (b) IR, (c) WV, and (d) CO_2 channels at FT03 and (e) VIS, (f) IR, (g) WV, and (h) CO_2 channels at FT15. The dotted lines indicate ALL. The solid line represents B03 in (a) and (e), B07 in (b) and (f), B08 in (c) and (g), and B16 in (d) and (h). The dashed line represents B13 in (b) and (f), and B09 in (c) and (g). The dash-dot line represents B10 in (c) and (g).

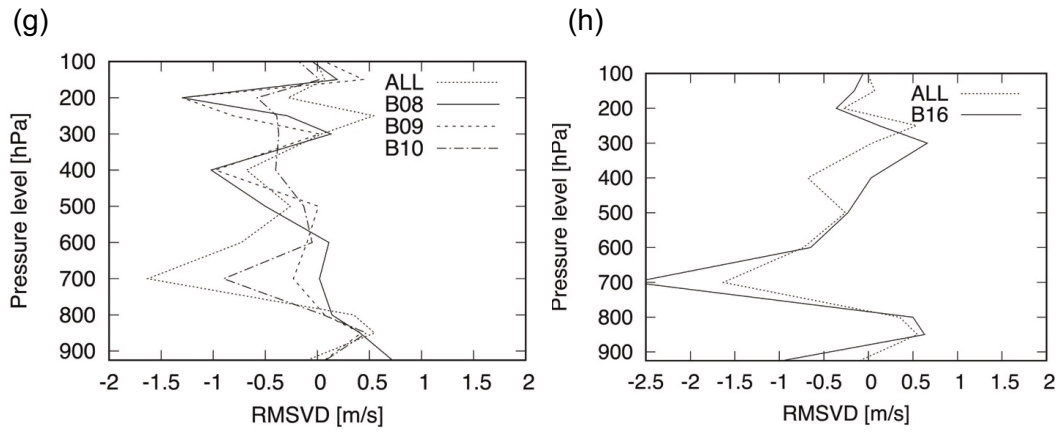

Figure 3.11. Continued.

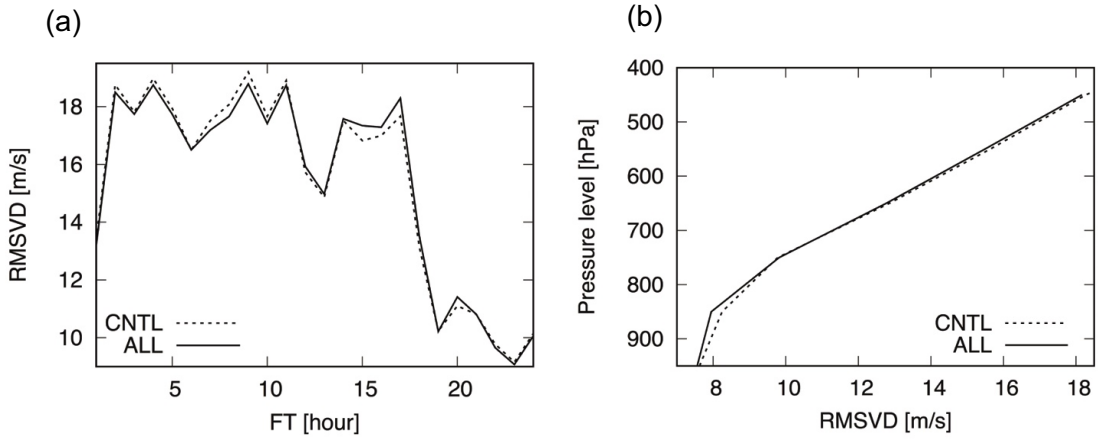

Figure 3.12. Forecast winds in northern Japan validated against WPR observations. (a) at each forecast hour and (b) profiles of RMSVD averaged over the whole forecast period. The solid lines and dashed lines represent ALL and CNTL, respectively.

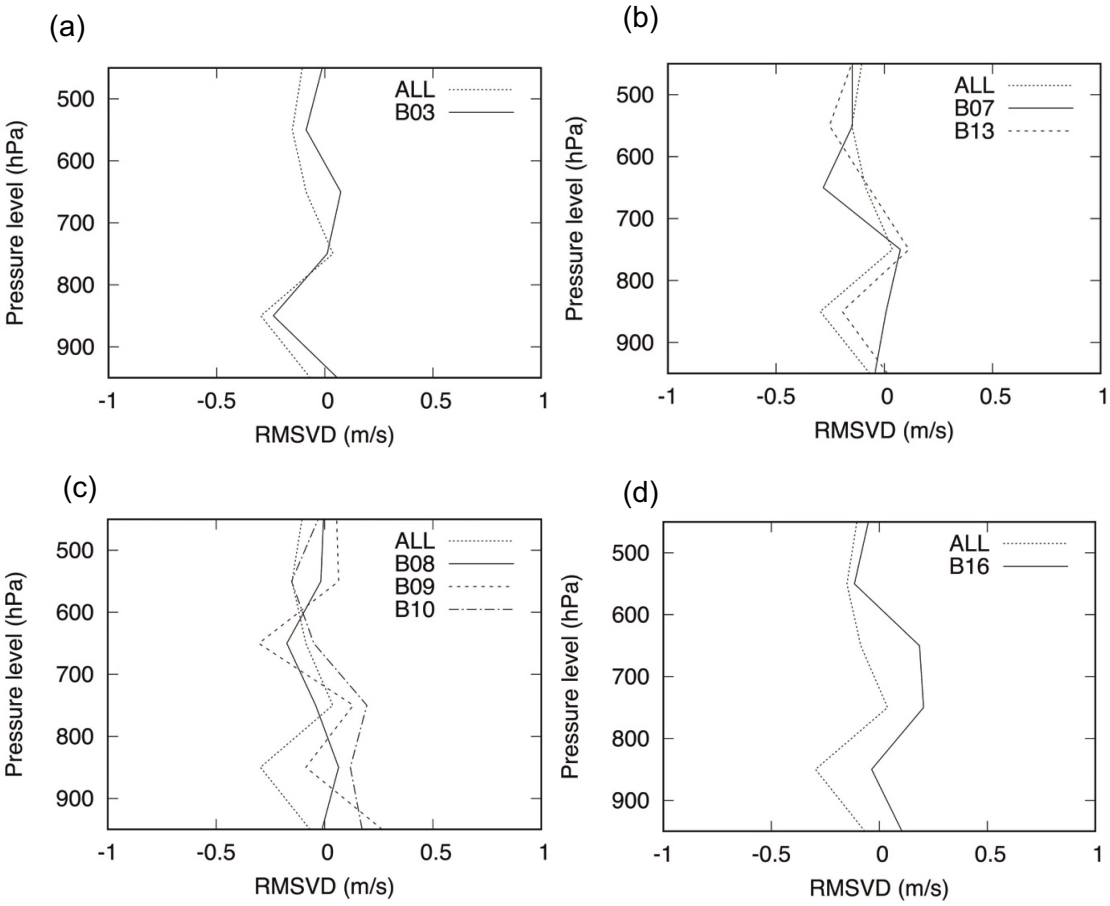

Figure 3.13. Forecast winds in northern Japan validated against WPR observations. Profiles of RMSVD differences from CNTL averaged over the entire forecast period for the (a) VIS, (b) IR, (c) WV, and (d) CO_2 channels. The dotted lines indicate ALL. The solid line represents B03 in (a), B07 in (b), B08 in (c), and B16 in (d). The dashed line represents B13 in (b) and B09 in (c). The dash-dot line represents B10 in (c).

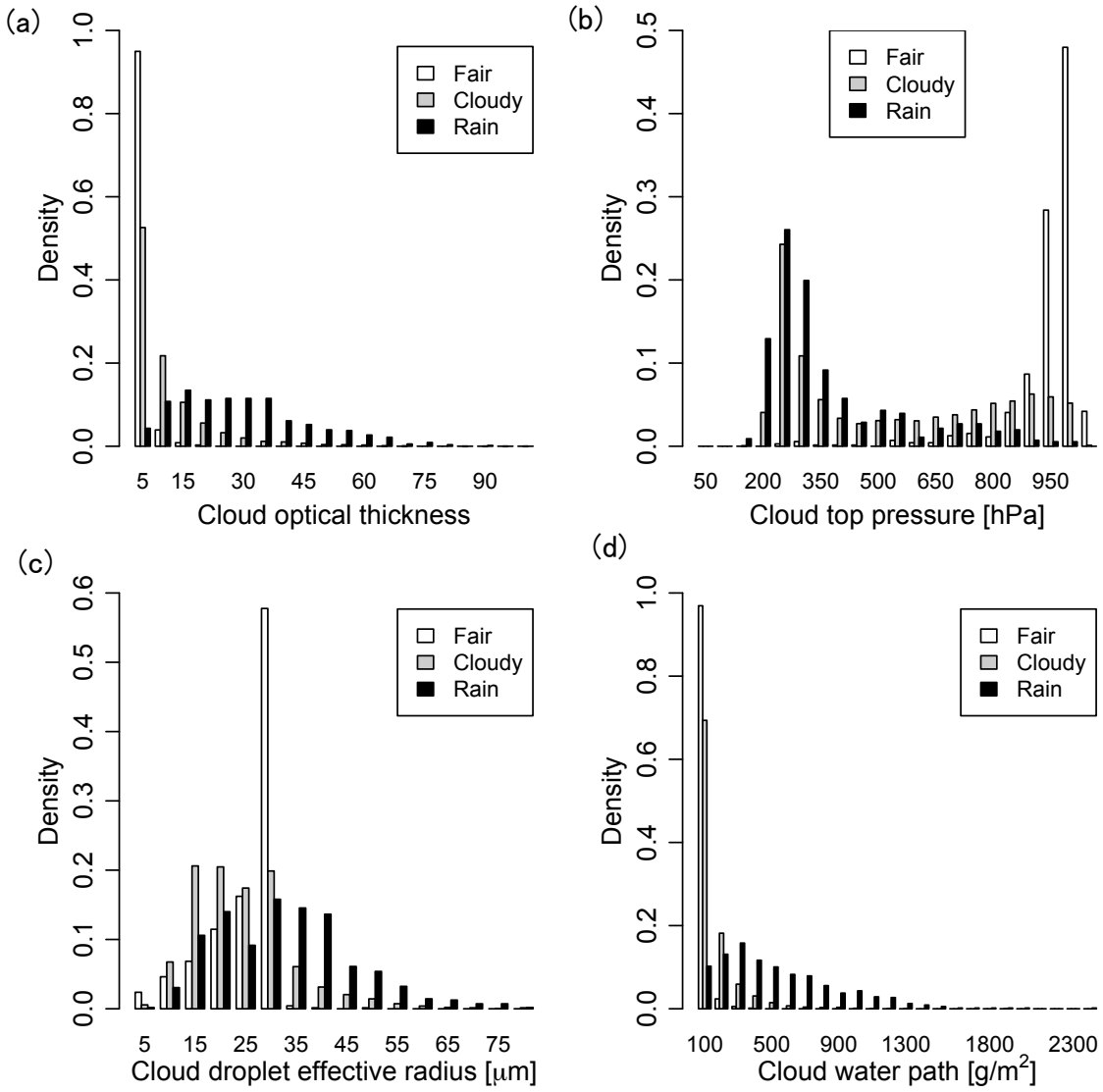

Figure 4.1. Appearance frequencies of cloud properties: (a) COT, (b) CTP (hPa), (c) CRE (μm), (d) CWP (g m^{-2}) according to present weather categories in July 2017. White, light gray, and black bars represent fair, cloudy, and rainy weather conditions.

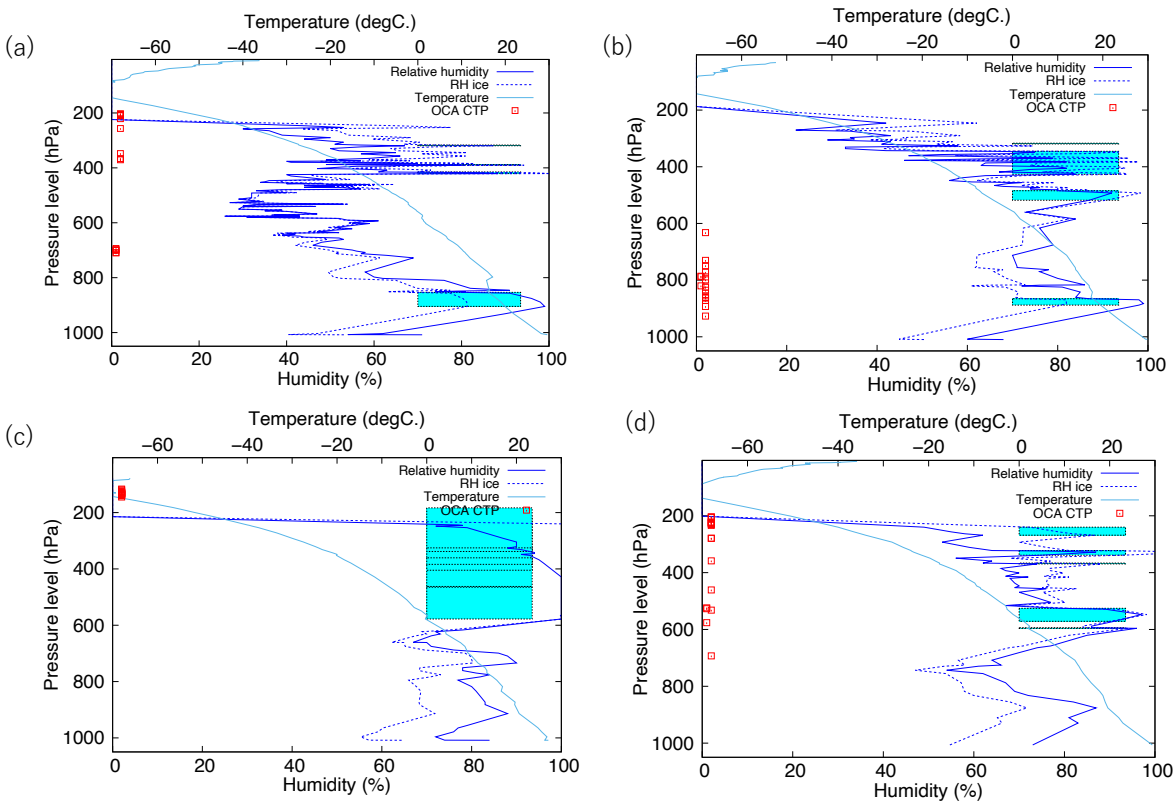

Figure 4.2. Examples of relative humidity over water (solid blue lines) and ice (dashed blue lines) and temperature (solid turquoise blue lines) profiles, and cloud layers (light blue rectangles) obtained by sonde observations together with OCA CTPs (red squares) within a radius of 5 km from a sonde station (Fukuoka). (a) 1 July, (b) 2 July, (c) 9 July, and (d) 10 July 2017. CF values in tenth were (a) 10^{-1} (overcast with openings), (b) 7, (c) 10^{-1}, and (d) 10^{-1}. There was rain in (c).

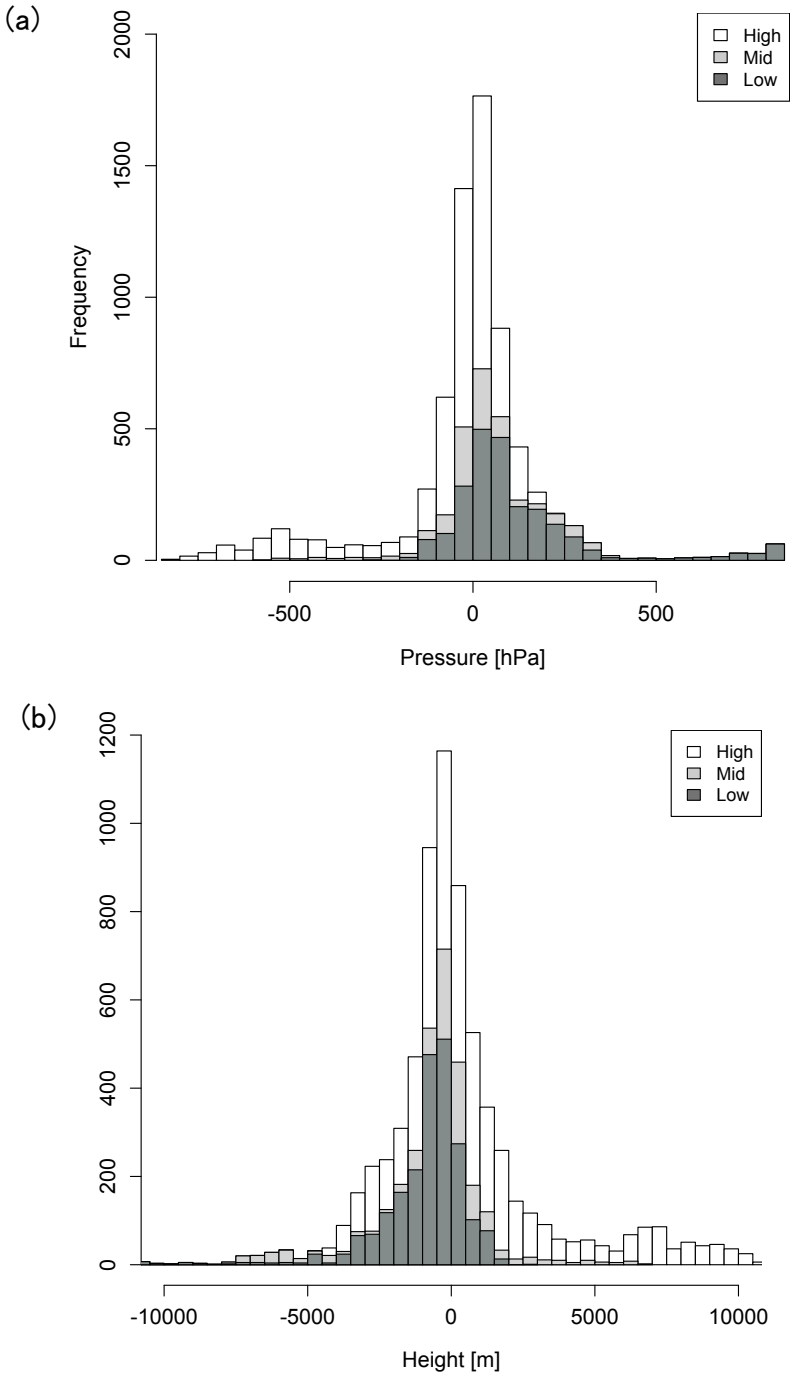

Figure 4.3. Frequencies of differences of (a) CTP (hPa) and (b) CTH (m) between OCA and sonde observation (OCA minus sonde) in July 2017. The white, light gray, and dark gray bars are histogram when OCA CTP levels were higher than 440 hPa, equal to 440−680 hPa, and lower than 680 hPa.

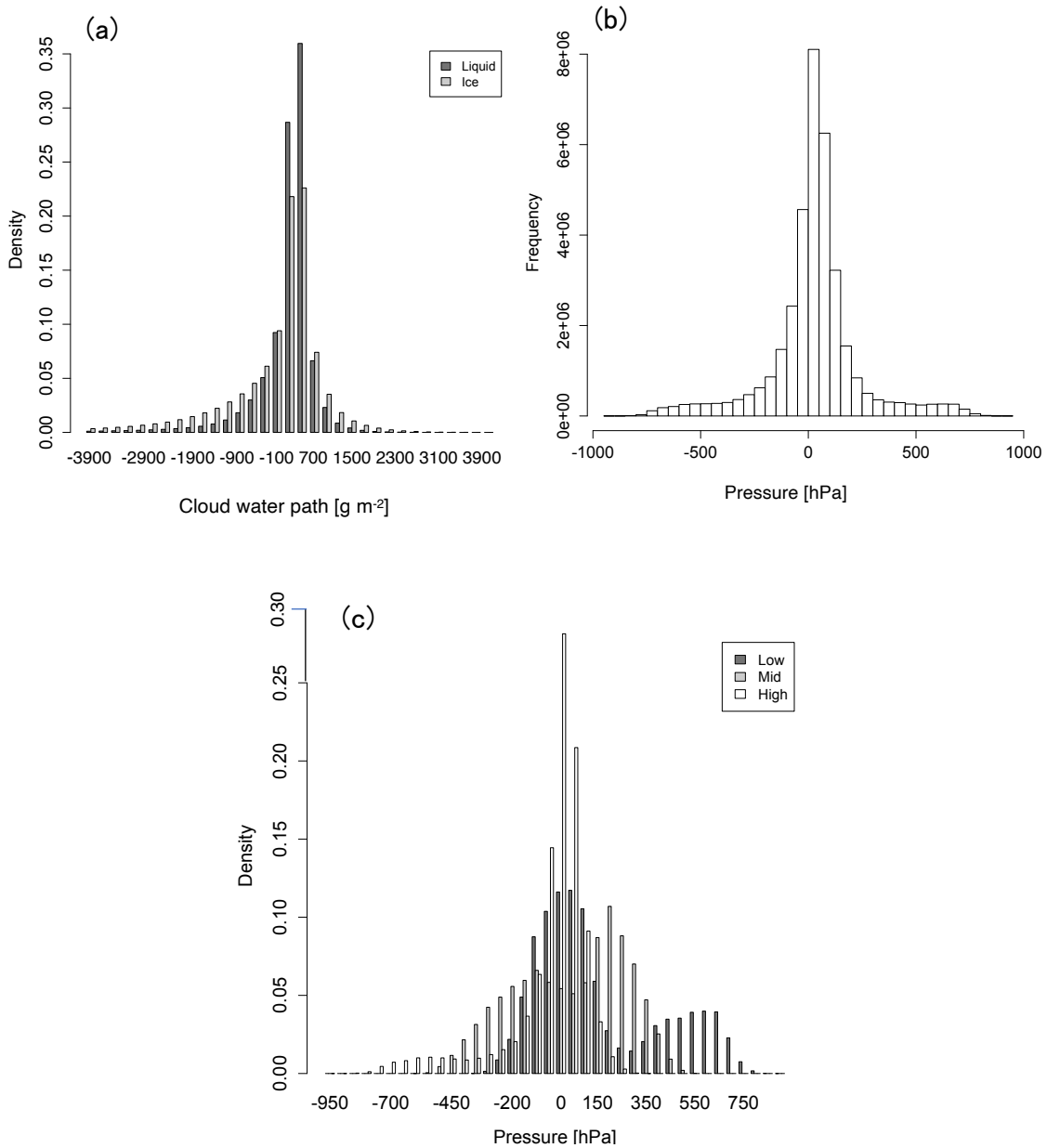

Figure 4.4 Frequencies of differences between OCA and NHM (OCA minus NHM) during the period 0000−0900 UTC 7−10 September 2015: (a) CWP (LWP and IWP are shown by dark and light gray bars, respectively) (g m^{-2}), (b) all OCA CTP levels (hPa), and (c) OCA CTP values at three heights. The white, light gray, and dark gray bars show frequencies when OCA CTP levels were above 440 hPa, equal to 440−680 hPa, and below 680 hPa. In (a), the left and the right sides of the histograms are cutoff. The minimum and maximum differences (g m^{-2}) for LWP and IWP are -68,719 and 1,997, -72,983 and 4,815, respectively.

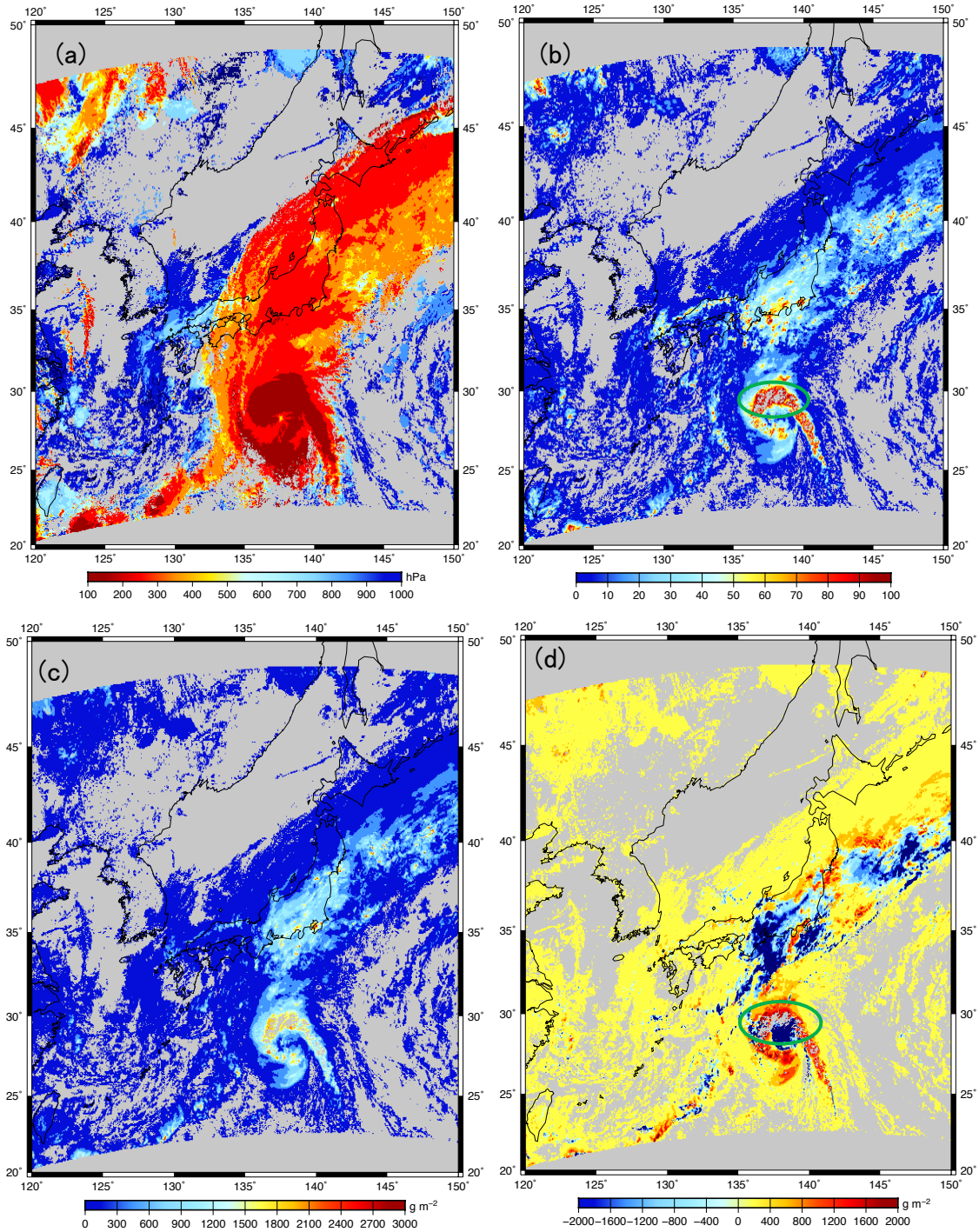

Figure 4.5. Himawari-8 OCA data: (a) CTP (hPa), (b) COT, and (c) CWP (g m^{-2}), and (d) CWP differences between OCA and NHM (OCA minus NHM) at 0200 UTC 8 September 2015. In (b), the gray pattern in the vicinity of the typhoon (green circle) represents COT values above 100 and corresponds to the gray pattern in the same area in (d).

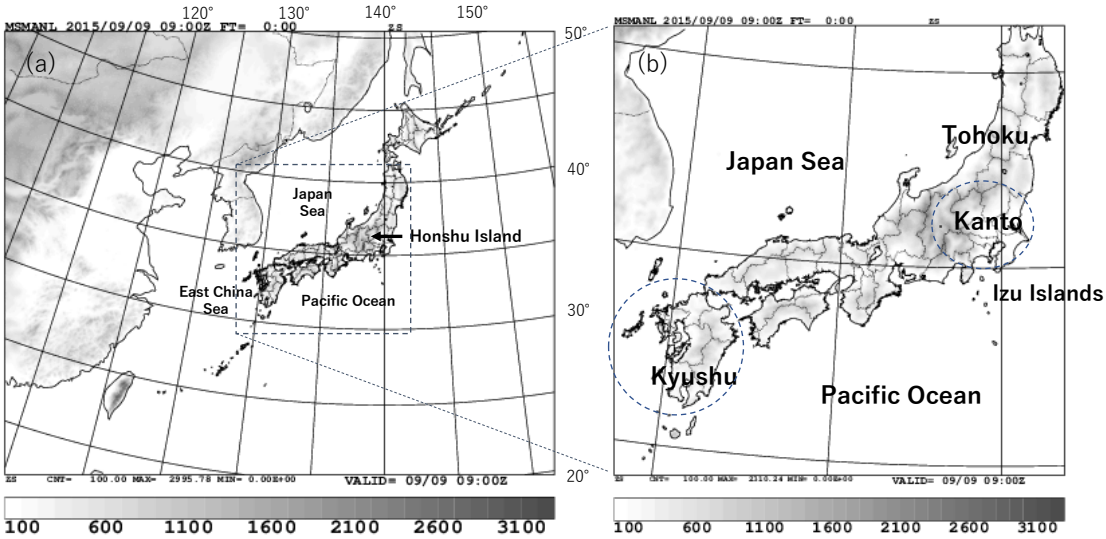

Figure 4.6. (a) The JNoVA domain and (b) locations of the Kanto and Kyushu areas (circles with dashed lines), where the heavy rainfalls examined in the experiments of this study occurred, and surrounding areas. Topography (meters above sea level) is indicated by shading.

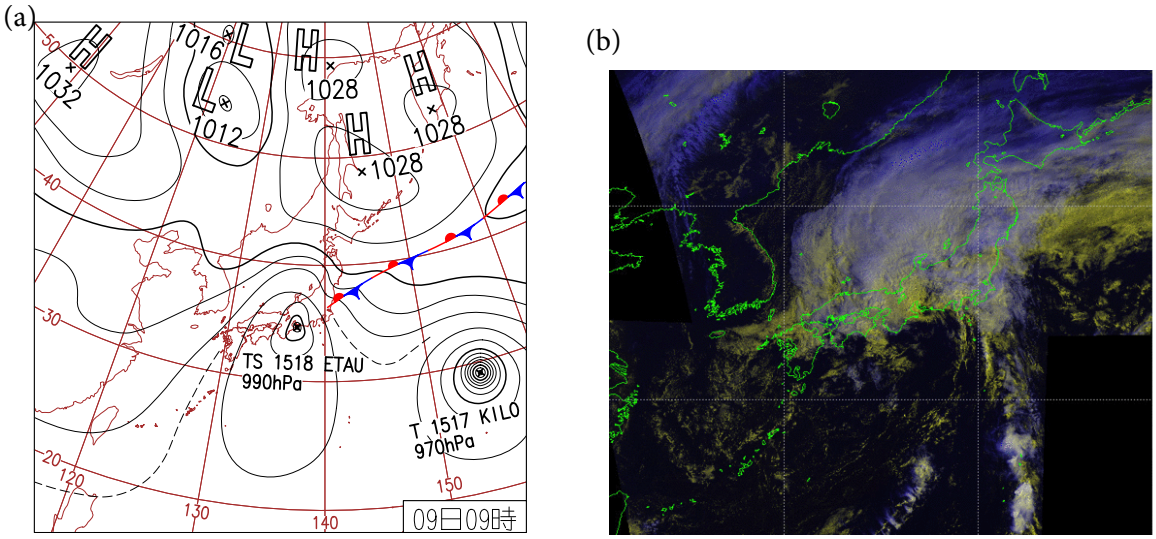

Figure 4.7. Synoptic situation for the assimilation experiment on 9 September 2015. (a)Surface weather map and (b) Himawari-8 IR and VIS composite image at 0000 UTC produced by JMA. In (b), yellow color represents low clouds, white represents thick and high clouds such as Cb and Ns, and blue represents cirrus clouds.

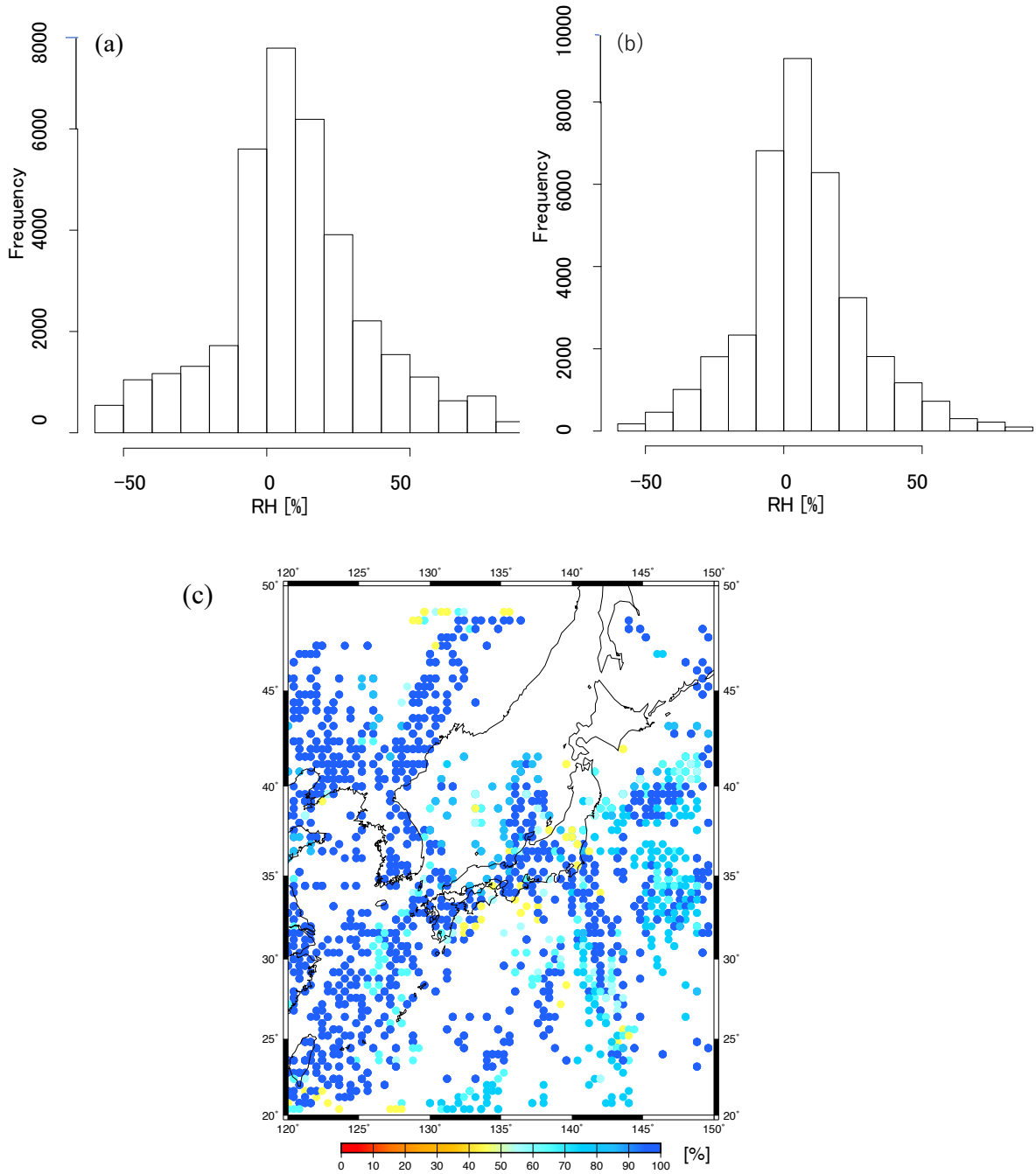

Figure 4.8. Frequency histograms of departures of assimilated OCA pseudo-RH from (a) first-guess and (b) analysis results during the 0000−0900 UTC 9 September 2015 assimilation period. (c) Distribution map of pseudo-RH data points at 0900 UTC. In (c), the circles indicate points where pseudo-RH profiles for assimilation were obtained. The color of each circle indicates the pseudo-RH value at the top of the profile.

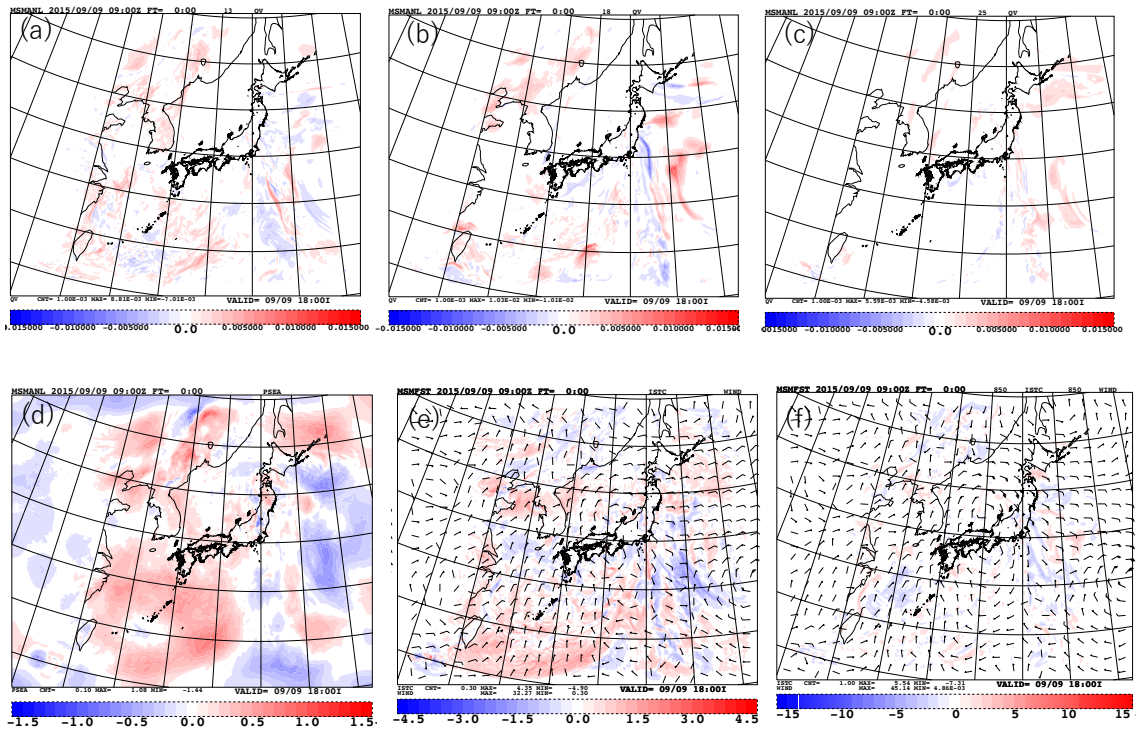

Figure 4.9. Differences in analysis results between TEST and CNTL at 0900 UTC 9 September 2015. Water vapor mixing ratio (kg kg^{-1}) at (a) 850 hPa, (b) 700 hPa, and (c) 500 hPa, (d) sea surface pressure and wind speed at (e) the surface and (f) 850 hPa. Color shading in (e) and (f) indicates differences of wind speed (m s^{-1}) between TEST and CNTL, and arrows indicate wind vectors in TEST.

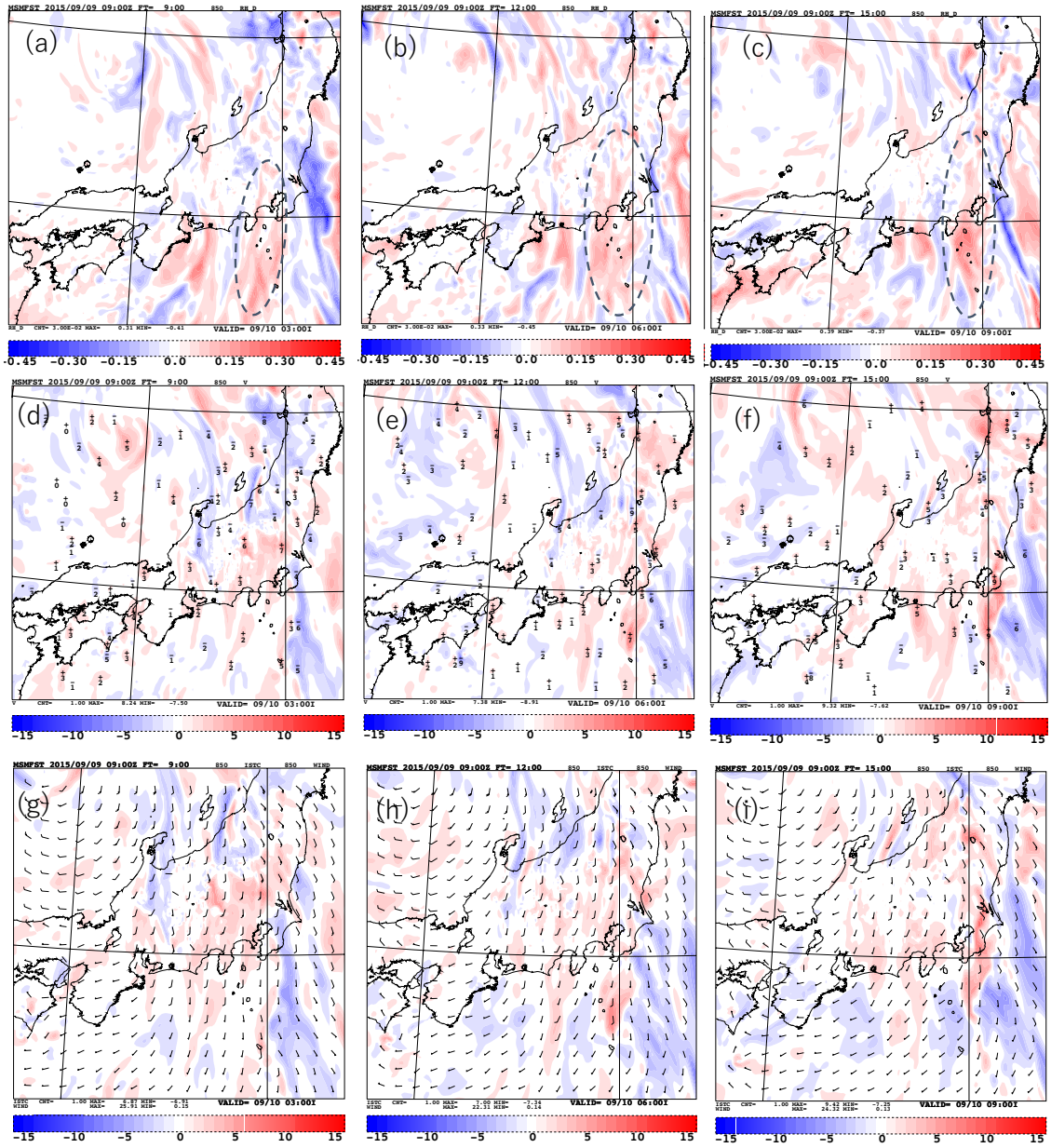

Figure 4.10. Differences of forecast RH and wind speed at 850 hPa between TEST and CNTL. (a), (b) and (c) for RH (%), (d), (e) and (f) for v-component wind (m s^{-1}), and (g), (h) and (i) for wind speed (m s^{-1}). (a), (d) and (g) at the 9 h, (b), (e), and (h) at 12 h, and (c), (f), and (i) at 15 h forecast time. Color shading indicates differences of RH in (a)−(c) and wind speed in (d)−(i) between TEST and CNTL, and arrows in (g)−(i) indicate wind vectors in TEST.

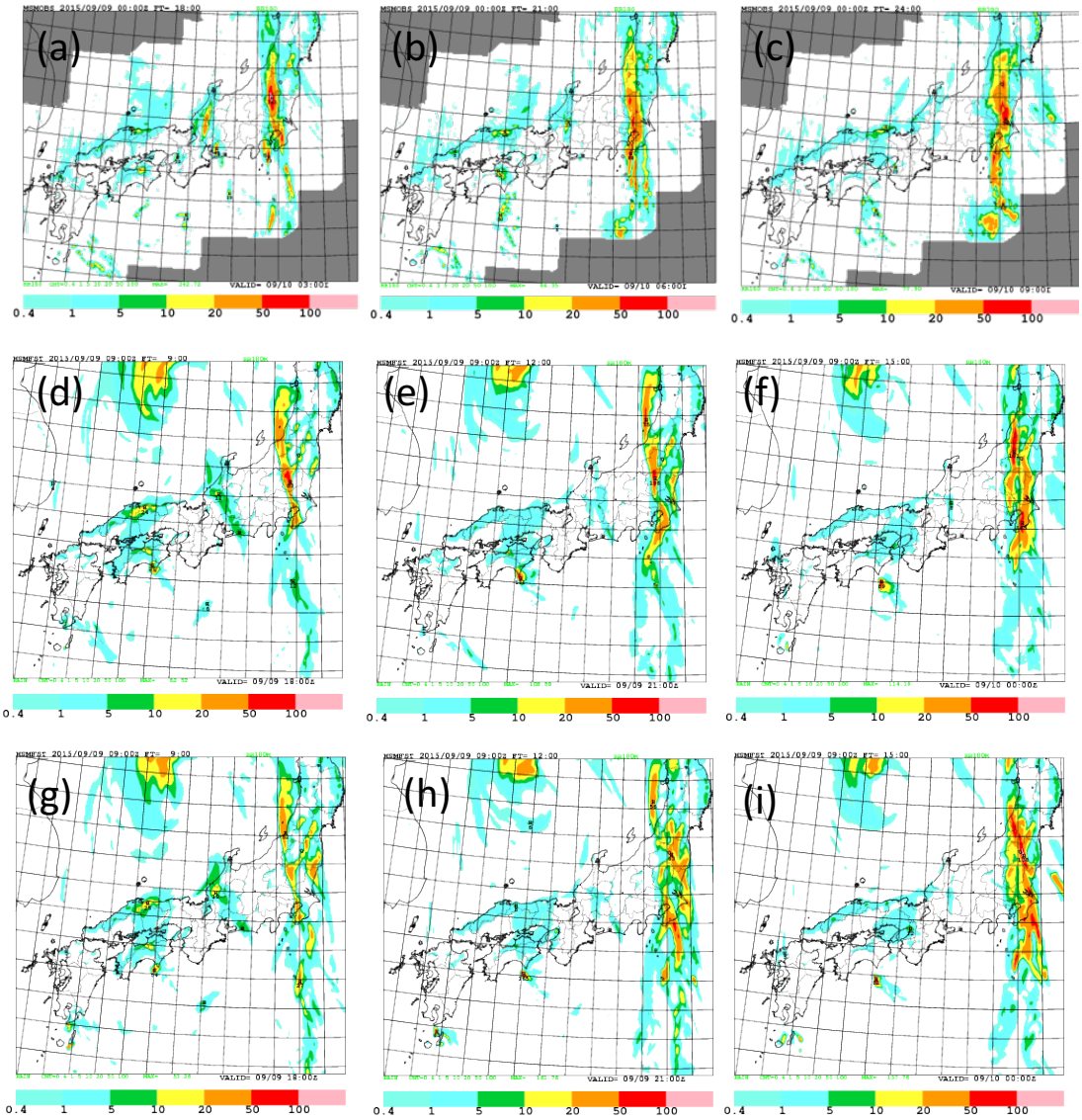

Figure 4.11. 3-h precipitation (mm) in observations and forecasts on 9 September 2015. (a), (b), and (c) Radar/rain gauge-analyzed precipitation (RAP); (d), (e), and (f) forecasts by TEST; (g), (h), and (i) forecasts by CNTL. (a), (d), and (g) FT = 09 (1800 UTC 9 September 2015); (b), (e), and (f) FT = 12 (2100 UTC 9 September 2015); (c), (f), and (i) FT = 15 (0000 UTC 10 September 2015).

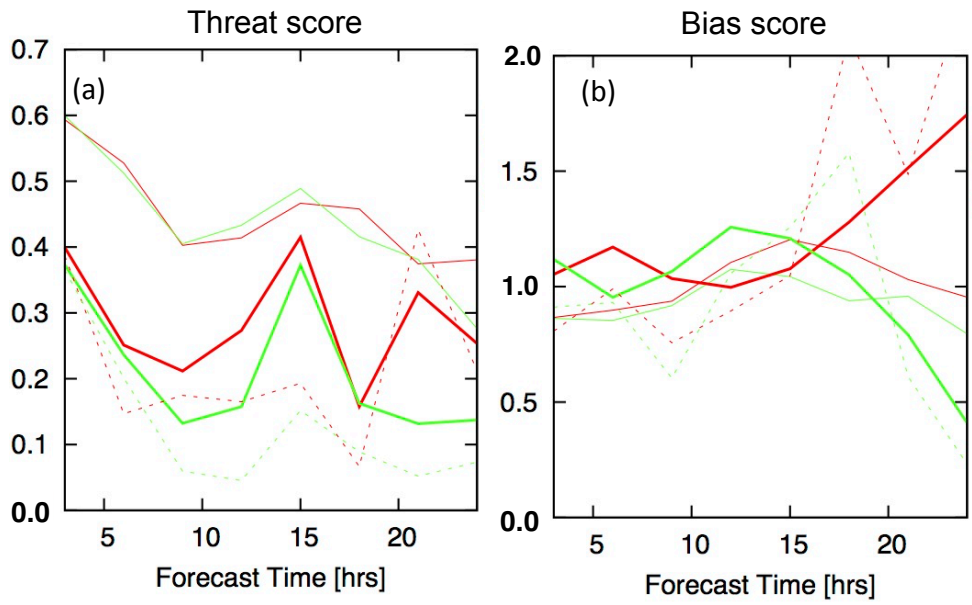

Figure 4.12. Precipitation forecast (a) threat and (b) bias scores for the 3-h precipitation thresholds at every 3 h of forecast time in CNTL (green lines) and TEST (red lines). Thin, thick, and dashed lines indicate threshold values of 1 mm, 10 mm, and 20 mm, respectively. Threat score = hits / (hits + misses + false alarms). Bias score = (hits + false alarms) / (hits +misses).

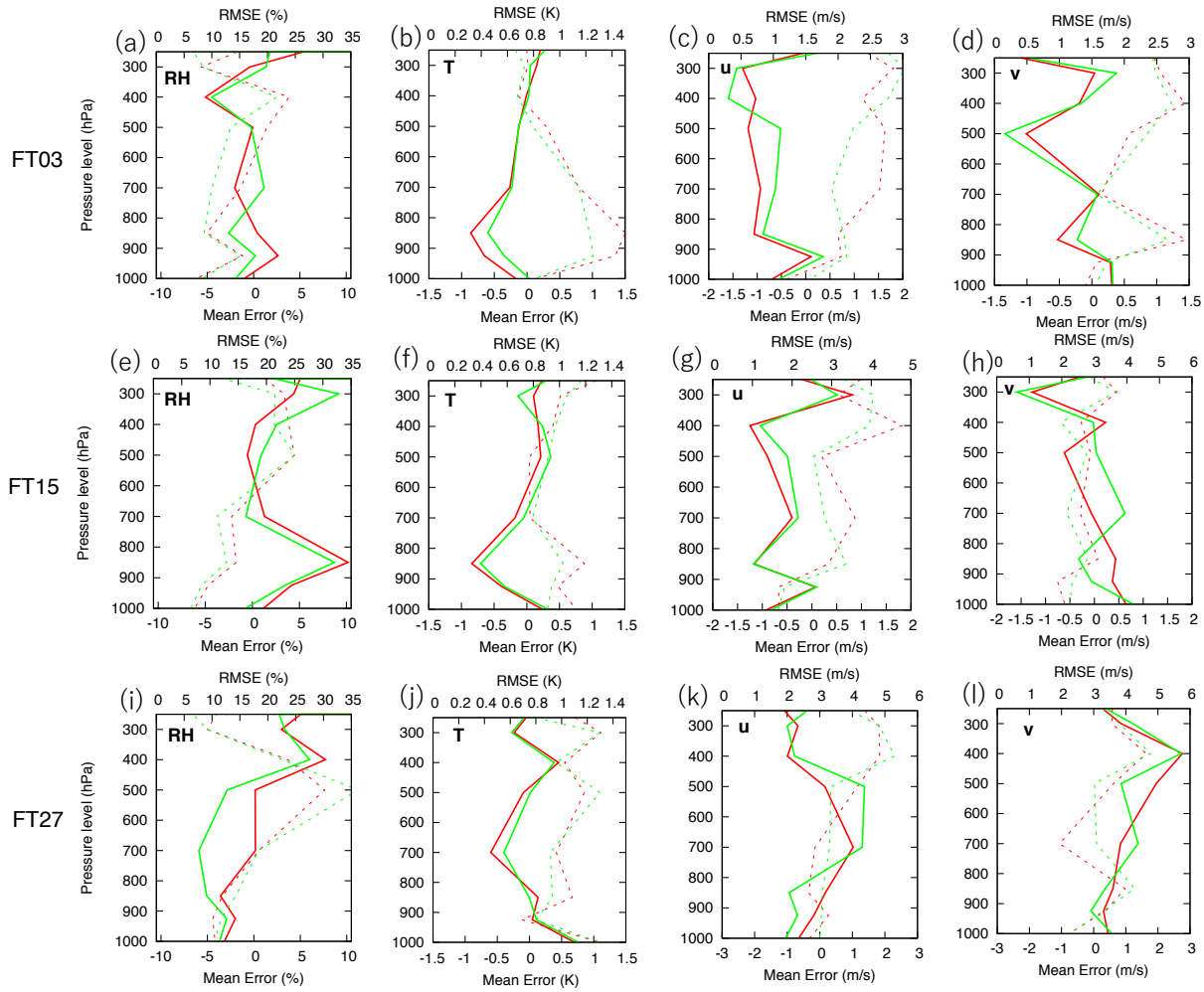

Figure 4.13. Forecast RH, temperature, and wind validated against sonde observations. (a, b, c, d) FT = 03 (1200 UTC 9 September 2015); (e, f, g, h) FT = 15 (0000 UTC 10 September 2015); (i, j, k, l) FT = 27 (1200 UTC 10 September 2015). (a, e, i) RH (%); (b, f, j) temperature (K); (c, g, k); u-component wind (m s^{-1}); and (d, h, i) v-component wind (m s^{-1}) in CNTL (solid green lines) and TEST (solid red lines). The green dashed lines represent RMSEs in CNTL, and the red dashed lines represent RMSEs in TEST.

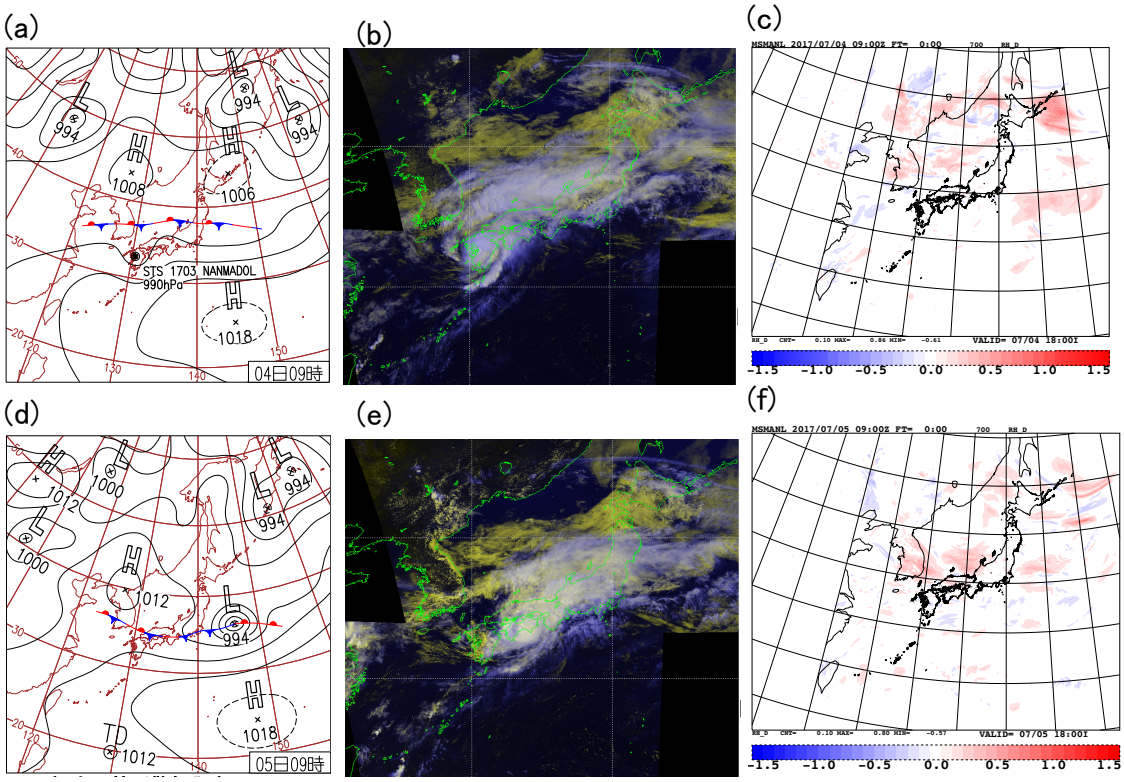

Figure 4.14. Synoptic situation and differences in water vapor analyses for the assimilation experiments on 4 and 5 July 2017. (a, d) Surface weather maps, (b, e) Himawari-8 IR and VIS composite images with the same color patterns as in Fig.4.7b, and (c, f) differences in analysis results for RH (%) between TEST and CNTL at 700 hPa at (a, b, c) 0000 UTC 4 July and (d, e, f) 0000 UTC 5 July.

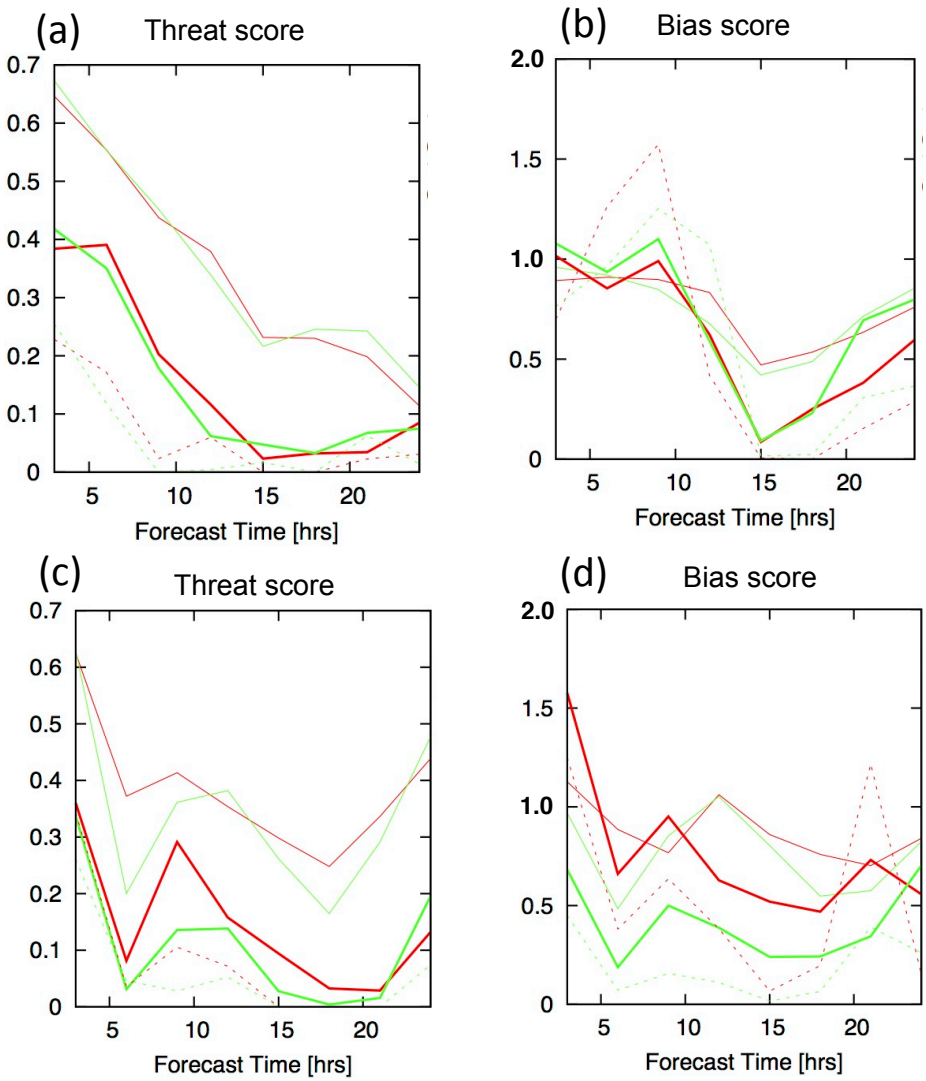

Figure 4.15. Precipitation forecast (a, c) threat and (b, d) bias scores for the 3-h precipitation thresholds at every 3 h of forecast time in the assimilation experiments on (a, b) 4 July and (c, d) 5 July 2017. Green lines represent CNTL, and red lines represent TEST. The thin, thick, and dashed lines indicate threshold values of 1 mm, 10 mm, and 20 mm, respectively.

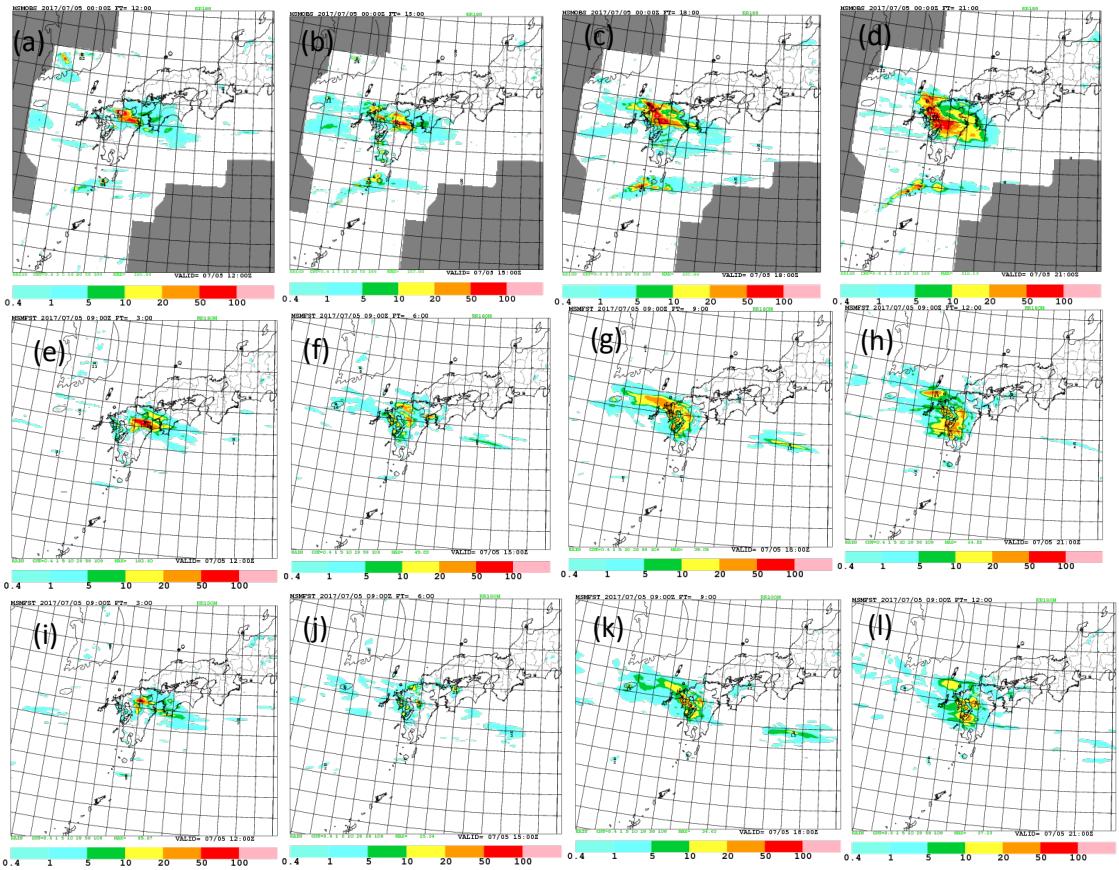

Figure 4.16. 3-h precipitation (mm) in observations and forecasts on 5 July 2017. (a, b, c, d) Radar/rain gauge-analyzed precipitation (RAP); (e, f, g, h) forecasts by TEST; (i, j, k, l) forecasts by CNTL. (a, e, f) at FT03 (1200 UTC); (b, f, j) at FT06 (1500 UTC); (c, g, k) at FT09 (1800 UTC); (d, h, l) at FT12 (2100 UTC).

Tables

Table 2.1. Root mean square difference (RMSD), mean error (ME), and root mean square vector difference (RMSVD) values of (a) RS-AMVs and (b) RTN-AMVs relative to NHM outputs.

(a)

Channel and level	RMSD (m s^{-1})	ME (m s^{-1})	RMSVD (m s^{-1})	Number of data
IR1 upper and middle	3.56	–0.91	4.77	17,134
WV upper and middle	3.47	0.24	4.99	30,427
IR1 lower	1.81	–0.34	3.03	403
VIS lower	2.06	0.83	3.21	677

(b)

Channel and level	RMSD (m s^{-1})	ME (m s^{-1})	RMSVD (m s^{-1})	Number of data
IR1 middle and upper	3.15	–1.26	4.18	4,997
WV middle and upper	2.91	–0.27	2.91	7,692
IR1 lower	1.77	–0.64	2.72	102
VIS lower	1.61	0.12	2.84	50

Table 2.2. Summary of the four test experiments, showing the length of assimilation time slot and data thinning interval used in each.

Experiment	Length of time slot	Time interval of thinning	Number of RS-AMVs assimilated
RSAMV10_10min	10 min	10 min	1,640
RSAMV10_3h	10 min	3 h	838
RSAMV_1h	1 h	1 h	1,624
RSAMV_3h	1 h	3 h	838

Table 3.1. Seven channels of the AHI used for computing RS-AMVs.

Channel	Wavelength (μm)	Category	Spatial resolution (km)	Time resolution (min)	AMV height level
B03	0.64	VIS	0.5	2.5	Low, Mid, High
B07	3.9	IR	2	5	Low, Mid, High
B08	6.2	WV	2	5	High
B09	6.9	WV	2	5	Mid, High
B10	7.3	WV	2	5	Mid, High
B13	10.4	IR	2	5	Low, Mid, High
B16	13.3	CO_2	2	5	Low Mid, High

Table 3.2. RMSVD, RMSD, and MD values of RS-AMVs relative to JMA mesoscale analyses.

Channel	Level	RMSVD (m s^{-1})	RMSD (m s^{-1})			MD (m s^{-1})			Number of data
			u	v	Wind speed	u	v	Wind speed	
B03	Low	3.36	2.36	2.39	2.29	-0.23	0.44	0.18	4,640,774
	Mid	4.47	3.17	3.15	3.17	-0.44	0.36	-0.24	4,254,577
	High	5.62	4.00	3.95	4.07	0.21	0.43	0.45	10,156,668
B07	Low	4.24	2.81	3.18	2.90	0.00	0.18	0.30	5,350,690
	Mid	4.73	3.28	3.41	3.37	-0.49	-0.02	-0.33	7,138,677
	High	5.46	3.84	3.87	3.93	-0.49	0.39	-0.33	16,538,184
B08	High	6.17	4.38	4.34	4.55	0.32	0.42	0.78	32,546,702
B09	Mid	6.05	4.46	4.09	4.45	0.41	-0.21	0.62	4,058,080
	High	5.79	4.09	4.10	4.22	0.14	0.39	0.52	34,008,689
B10	Mid	5.52	3.97	3.84	4.00	0.17	-0.11	0.33	6,937,140
	High	5.60	3.93	3.99	4.05	-0.03	0.38	0.29	33,239,433
B13	Low	4.58	3.05	3.41	3.05	0.15	0.07	0.40	5,478,365
	Mid	4.76	3.26	3.46	3.35	-0.38	-0.06	-0.21	9,179,591
	High	5.38	3.74	3.87	3.84	-0.32	0.37	-0.08	26,989,902
B16	Low	5.39	3.85	3.77	3.88	-0.17	0.10	0.25	606,951
	Mid	4.96	3.46	3.55	3.52	-0.18	-0.10	-0.00	7,604,681
	High	5.47	3.80	3.93	3.91	-0.09	0.38	0.23	28,758,289

Table 3.3. RMSVD, RMSD, and MD values of RS-AMVs relative to sonde observations.

Channel	Level	RMSVD ($m\ s^{-1}$)	RMSD ($m\ s^{-1}$)			MD ($m\ s^{-1}$)			Number of data
			u	v	Wind speed	u	v	Wind speed	
B03	Low	6.38	4.92	4.06	4.68	0.03	0.70	0.58	2,803
	Mid	6.84	5.28	4.35	5.14	-1.14	0.39	-0.88	3,673
	High	9.13	7.17	5.66	7.17	-0.88	0.81	-0.98	6,464
B07	Low	7.14	5.18	4.91	4.74	0.77	0.05	0.62	5,407
	Mid	7.24	5.54	4.66	5.51	-0.89	0.20	-0.80	7,853
	High	9.21	7.06	5.92	7.23	-1.36	1.00	-1.57	13,789
B08	High	10.42	8.03	6.65	8.29	0.12	0.99	0.47	17,479
B09	Mid	8.42	6.40	5.46	6.34	0.86	0.35	1.05	3,577
	High	9.89	7.62	6.29	7.83	-0.28	0.82	-0.12	17,375
B10	Mid	8.08	6.08	5.32	6.05	0.43	0.11	0.48	5,993
	High	9.77	7.56	6.18	7.72	-0.39	0.86	-0.30	17,190
B13	Low	7.24	5.23	5.01	4.72	0.77	-0.07	0.67	4,861
	Mid	7.35	5.51	4.87	5.52	-0.45	0.04	-0.44	7,747
	High	9.19	7.01	5.94	7.20	-0.96	0.86	-1.12	15,230
B16	Low	7.18	5.15	5.01	5.10	-0.02	0.39	-0.06	1,488
	Mid	7.60	5.78	4.94	5.66	-0.04	0.01	-0.01	7,054
	High	9.39	7.15	6.09	7.40	-0.50	0.85	-0.51	15,695

Table 3.4. RMSVD, RMSD, and MD values of low-level RS-AMVs in VIS, IR, and CO_2 channels relative to wind profiler observations.

Channel	RMSVD ($m\ s^{-1}$)	RMSD ($m\ s^{-1}$)			MD ($m\ s^{-1}$)			Number of data
		u	v	Wind speed	u	v	Wind speed	
B03	5.30	3.96	3.52	3.75	-0.07	0.31	0.16	72,952
B07	6.73	4.89	4.63	4.62	0.26	-0.11	0.18	70,892
B13	7.01	5.10	4.81	4.66	0.22	-0.33	0.19	68,948
B16	6.60	4.88	4.45	4.64	-0.46	-0.02	-0.52	23,269

Table 3.5. Estimated inter-channel observation error correlations. (a) Zonal wind components and (b) meridional components.

(a)

	B07	B08	B09	B10	B13	B16
B03	0.26	0.24	0.23	0.25	0.30	0.27
B07	-	0.21	0.22	0.26	0.35	0.29
B08	-	-	0.31	0.28	0.26	0.28
B09	-	-	-	0.32	0.28	0.30
B10	-	-	-	-	0.29	0.31
B13	-	-	-	-	-	0.32

(b)

	B07	B08	B09	B10	B13	B16
B03	0.28	0.24	0.25	0.27	0.31	0.28
B07	-	0.22	0.23	0.27	0.35	0.30
B08	-	-	0.33	0.31	0.26	0.30
B09	-	-	-	0.34	0.29	0.31
B10	-	-	-	-	0.31	0.33
B13	-	-	-	-	-	0.34

Table 3.6. Quality Index threshold values for each channel.

Channel	Threshold of QI number		
	Low	Mid	High
B03	0.60	-	-
B07	0.60	0.60	0.75
B08	-	-	0.90
B09	-	0.90	0.90
B10	-	0.90	0.90
B13	0.60	0.60	0.75
B16	-	0.90	0.90

Table 3.7. Observation error values for RS-AMVs used in JNoVA.

Pressure level (hPa)	Observation error (m s^{-1})	
	u	v
10	6.2	7.2
30	5.1	6.2
50	3.5	5.1
100	4.4	6.0
200	3.8	4.9
300	4.6	3.7
500	3.7	3.0
700	3.2	2.6
850	2.9	2.3
1000	4.1	3.3
1100	4.1	3.3

Table 3.8. Summary of the assimilation experiments.

Experiment	Level of RS-AMVs assimilated
B03	Low
B07	Low, Mid, High
B08	High
B09	Mid, High
B10	Mid, High
B13	Low, Mid, High
B16	Mid, High
ALL	Low, Mid, High

Table 4.1. OCA CTP and COT, SYNOP weather and cloud types, and their corresponding ISCCP classification for collocated SYNOP and OCA data in July 2017. Abbreviations of cloud types are from WMO International Cloud Atlas (WMO 2017). ISCCP cloud types were determined by applying the OCA CTP and COT values as parameters to the ISCCP cloud classification chart (Rossow and Schiffer 1991).

SYNOP weather	OCA CTP	Number of cases	OCA COT	SYNOP cloud type	ISCCP classification
Fair	High	7	2.14	Ci [w/ Ac, Cu, Cb, St]	Ci
	Mid	17	2.08	Ac [w/ Cu, St, Cb, Sc, Ci]	Ac
	Low	690	1.64	Cu, St, Sc, Cb [w/ Ac, As, Ci]	Cu
Cloudy	High	1,799	8.08	Ci, N/A, Cs [w/ Ac, As, Cu, Cb, Sc]	Cs
	Mid	554	12.0	Ac, N/A, As [w/ Cu, Sc, St, Cb, Ci]	As
	Low	1,218	6.43	Cu, St, Sc, Cb [w/ Ac, As, Ci]	Sc
Rain	High	429	26.1	N/A, Ci, Cs [w/ Ac, As, Cu, St, Cb, Sc]	Deep convection
	Mid	74	32.7	N/A, Ac [w/ Cu, St, Sc, Cb, Ci]	Ns
	Low	54	24.3	Cu, St, Cb, Sc [w/ Ac, Ci]	St

Table 4.2. OCA cloud occurrences validated against SYNOP at JMA surface stations in July 2017. "N/A" means "not available" in SYNOP due to obstruction of view.

Cloud height	Hit (w/ clouds)	Correct reject (w/o clouds)	False	Miss	N/A	Total
High	1,640	546	39	1,418	1,610	5,253
Mid	878	1,308	297	2,000	770	5,253
Low	2,547	75	64	2,553	14	5,253

Table 4.3. OCA cloud occurrences validated against sonde observations at JMA upper-air stations in July 2017.

Cloud height	Hit (w/ clouds)	Correct reject (w/o clouds)	False	Miss	N/A
High	203	204	33	113	553
Mid	54	359	80	60	553
Low	104	162	198	89	553

Table 4.4. Clear-sky climatological RH for July and September derived from 10 years (2007–2016) of sonde observations in each of the height classes.

	RH (%)	
Height (m)	July (2007–2016)	September (2005–2014)
0–500	77.4	73.6
500–1500	66.4	63.1
1500–2500	57.5	51.3
2500–3500	51.2	45.3
3500–4500	46.6	41.9